

Doctoral Dissertation (Censored)

博士論文（要約）

Improvements of the vertical structure of precipitation systems
in the numerical weather prediction models
by advancement of physical processes schemes
using remote sensing observations as reference

（リモートセンシング観測データを参照値として用いた
物理過程スキームの高度化による数値予報モデルでの
降水システムの鉛直構造の改良）

Yasutaka Ikuta

幾田 泰醇

Abstract

Large amounts of precipitation associated with torrential rains and tropical cyclones (TCs) can cause disasters that destroy social infrastructure. Therefore, accurate forecasting of precipitation is an important issue for disaster prevention, and it is necessary to understand and model the internal structure of the precipitation system. In modeling, the enhancement of the cloud microphysics scheme will not only clarify the mechanisms of torrential rains and TCs, but also play a significant role in improving the accuracy of numerical weather prediction (NWP). In recent years, with the improvement of observation technology, many studies have been conducted to utilize wide-area and continuous remote sensing observations by ground-based radar and satellites for the improvement of cloud physics schemes in NWP models. However, there are many unsolved aspects of the physical processes, such as the diversity of solid precipitation in the cloud microphysics scheme and the model resolution dependence of the boundary layer scheme, and there is no unified solution for modeling.

Therefore, in this study, the NWP model was validated using satellite microwave radiometers, satellite-borne radars, ground-based polarimetric radars, and optical disdrometers as reference values, and the physical scheme was refined based on them. The NWP model used was the Japan Meteorological Agency's non-hydrostatic model ASUCA, which is a recursive acronym of "ASUCA is a System based on a Unified Concept for Atmosphere". Since a comparison between the model and remote sensing observations requires a precise simulation of the observations, an observation simulator was developed and used for the validation. First, the NWP model was validated using a satellite microwave radiometer and satellite-borne radar in the case of heavy rainfall, and it was found that there were problems with the conversion rate from cloud ice to snow and raindrop evaporation efficiency in the cloud microphysics scheme. Therefore, the forecast was improved by modifying the conversion efficiency to snow, the cloud ice fall rate, and the particle size distribution (PSD) of raindrops. Next, the internal structure of TCs was verified using ground-based polarimetric radar and an optical disdrometer. Based on the polarimetric parameters and observed PSD of hydrometeors, we developed a 1-moment scheme that can predict the bimodal raindrop PSD. Furthermore, based on the vertical distribution of the observed polarization parameters, temperature-dependent shape characteristics were introduced to the snow particles in the NWP model. These changes to the cloud microphysics scheme improved the accuracy of polarization parameter predictions, suppressing the difference in reflectivity (Z_{DR}) between horizontal and vertical polarization, which was excessive at altitudes below 1 km, and increasing the Z_{DR} and the rate of change in phase difference between polarizations, which was excessive at altitudes above 5 km. The improved cloud microphysical scheme increased the snow mixing ratio and the latent heat release in the upper troposphere.

The relationship between the detailed boundary layer (BL) structure prediction inside the precipitation system and the boundary layer scheme in the TC secondary circulation was also investigated. The boundary layer (BL) schemes used were Mellor-Yamada-Nakanishi-Niino level 3 (MYNN3) as a scheme based

on the Reynolds-averaged Navier-Stokes equation, the anisotropic Deardorff model (ADM) as a gray zone scheme, and Deardorff (DDF) as a Large eddy simulation (LES) scheme. The results of Doppler velocity validation revealed the relationship between the BL scheme and the predictability of the organized structure inside BL. The simulations with the DDF scheme reproduced a horizontal roll structure on a larger scale than observed, with BL thickness and secondary circulation values closest to the observed values; none of the experiments with the MYNN3 scheme and the ADM scheme produced any rolls. Their BL heights were higher than observed, suggesting that the MYNN3 and ADM schemes are not suitable for simulating the 250m grid in this case study. These results were also confirmed for the LES with 50 m grid spacing using the DDF scheme.

In this study, the NWP model was validated using remote sensing observations to improve the scheme. The improved scheme, which is supported by observations, improves the reliability of forecasting the momentum inside the precipitation system and the vertical structure of the mass of hydrometeors. The knowledge gained from the improved reproducibility of the detailed structure of the boundary layer in addition to the spatial distribution and particle shape of the water mass is expected to contribute significantly to the advancement of the physics scheme and the reduction of uncertainty in the cloud precipitation process and its progress and understanding.

Index

| | |
|---|-----|
| 1. General introduction..... | 4 |
| 1.1. Numerical weather prediction | 5 |
| 1.2. Cloud microphysics | 7 |
| 1.3. Planetary boundary layer | 9 |
| 1.4. Evaluation of NWP against remote sensing | 1 1 |
| 1.5. The objective of this study | 1 5 |
| 2. Method | 1 6 |
| 2.1. NWP model | 1 6 |
| 2.2. Integrated satellite simulators..... | 1 6 |
| 3. Improvement of the cloud microphysics scheme using space-borne radar and microwave imager | 2 1 |
| 3.1. Introduction | 2 1 |
| 3.2. Method..... | 2 2 |
| 3.2.1. JMA meso-scale model (MSM)..... | 2 2 |
| 3.3. A case study..... | 2 7 |
| 3.4. A kinematic model analysis..... | 3 4 |
| 3.4.1. Positive bias of brightness temperature | 3 5 |
| 3.4.2. Overestimated reflectivity above melting layer..... | 3 6 |
| 3.4.3. Underestimated reflectivity at lower layer..... | 3 7 |
| 3.5. Impacts on the numerical weather forecasts..... | 3 8 |
| 3.6. Conclusions | 4 1 |

| | |
|---|-----|
| 4. Improvement of cloud microphysics scheme using polarimetric radar and disdrometer | 4 4 |
| 5. Evaluation of turbulence scheme using the ground-based radar observation | 6 3 |
| 5.1. Introduction | 6 3 |
| 5.2. Model and simulation | 6 4 |
| 5.2.1. Non-hydrostatic model ASUCA | 6 4 |
| 5.2.2. Integrated satellite simulators (I-Simulator) | 6 7 |
| 5.3. Observations of Faxai | 6 7 |
| 5.4. Numerical results | 7 1 |
| 5.4.1. Track and central pressure | 7 1 |
| 5.4.2. Simulations of radar | 7 2 |
| 5.4.3. Azimuthally averaged values | 7 3 |
| 5.4.4. Budget analysis | 7 6 |
| 5.4.5. Circulation structures in the planetary boundary layer | 8 0 |
| 5.4.6. Spatial frequency | 8 5 |
| 5.5. Conclusion | 8 7 |
| 6. General discussion | 9 0 |
| 6.1. Effective observation for evaluation | 9 0 |
| 6.2. Universality of improvement | 9 1 |
| 6.3. Effects of snow shape on the atmosphere | 9 1 |
| 6.4. Dependency on resolution | 9 2 |
| 7. General conclusion | 9 4 |

| | |
|---|-------|
| 7.1. Improvement of cloud microphysics scheme | 9 4 |
| 7.2. Evaluation of turbulence schemes | 9 5 |
| 7.3. Conclusion..... | 9 7 |
| Appendix | 9 9 |
| List of acronyms..... | 9 9 |
| Acknowledgment..... | 1 0 2 |
| References | 1 0 3 |

1. General introduction

Weather disasters caused by torrential rains and typhoons (we arbitrarily use the terms typhoons and hurricanes to refer to tropical cyclones, TCs) are responsible for the destruction of social infrastructure and the loss of human lives. To mitigate weather-related disasters, it is important to predict the phenomena that cause disasters and prepare for their occurrence. To improve the accuracy of forecasting weather phenomena, it is necessary to improve the accuracy of numerical weather prediction (NWP) models. In particular, phenomena with precipitation and strong winds that cause disasters depend on the accuracy of the physical schemes in the NWP model. In other words, to improve the forecast accuracy of severe weather events, the physical schemes need to be refined. However, there are many uncertainties in the physical schemes. For example, cloud precipitation processes are modeled under various assumptions, as there are many unresolved aspects due to the diversity of precipitation particles. In order to perform modeling, a scientific understanding of the phenomena is essential. To understand a phenomenon, it is necessary to observe the phenomenon accurately. In recent years, with the improvement of observation technology, research has been conducted to improve the physical scheme of numerical models by using wide-area and continuous remote sensing observations from ground-based weather radars and earth observation satellites. Improvements in the physical scheme lead to improved predictions of the vertical structure of the precipitation system. The vertical structure inside a precipitation system is related to the vertical transport of atmospheric water, heat, and momentum. This vertical transport is important both meteorologically and climatologically. For example, vertical transport determines the intensity of prominent phenomena such as heavy rainfall and strong winds on short timescales and the magnitude of climate variability on long timescales. However, vertical transport is difficult to be observed directly, and the amount transported vertically is highly uncertain. In this study, the mechanism of vertical transport is analyzed using NWP models with improved reproducibility based on remote sensing observations. From the results, we identified the major physical processes that contribute to the improved reproducibility of the vertical structure prediction of precipitation systems and clarified the impact of these physical processes on the atmosphere.

The history and overview of NWP model is first presented in Section 1.1. Section 1.2 describes the overview of cloud microphysical processes that are closely related to the prediction of precipitation systems. Section 1.3 describes the planetary boundary layer processes related to the near surface substructure of the precipitation system. Section 1.4 describes the verification by vary remote sensing observations to show the robustness of the arguments concerning these physical processes.

1.1. Numerical weather prediction

Current weather forecasts are based on the NWP, which is a numerical model described by equations based on physical laws and predicted numerically by supercomputers. The birth of NWP dates back to the 1900s. The idea of predicting atmospheric conditions by applying the equations of hydrodynamics to the atmosphere was proposed by Bjerknes in 1904. Richardson used hand calculations to predict the atmosphere as proposed by Bjerknes. This Richardson calculation failed, showing unrealistic pressure changes (Richardson 1922). Numerical forecasting in practice was initiated in Sweden in 1954 by Rossby and others. The United States began numerical forecasting operations in 1955. In Japan, numerical forecasting operations began in 1959. In the 1960s, NWP services were launched in many countries around the world. The European Centre for Medium-Range Weather Forecasts (ECMWF), which has the world's highest forecast accuracy as of 2023, began operations in 1979.

Forecast models used in NWP have evolved from models with large assumptions to models with fewer assumptions. The evolution of the field of numerical modeling can be roughly described as follows: Until the 1970s, models were used only for the prediction of large-scale atmospheric motion, as described above; in the 1980s, models reverted to primitive models and assumed hydrostatic balance; since the 1980s, non-hydrostatic models that do not use the hydrostatic balance approximation have been used. In the 2000s, as computer performance improved, the resolution of numerical forecasts became higher, and models with a horizontal grid spacing of 1 to 3 km were used at several NWP centers.

Early studies with non-hydrostatic models used an anelastic model (Ogura and Phillips 1962) that neglects the time derivative of density from the continuity equation based on scale analysis. This anelastic model does not include sound waves. Later, as computer performance improved, the elastic model was used (e.g., Durran and Klemp 1983; Ogura and Yoshizaki 1988). Elastic models include quasi-compressible and fully compressible models. The quasi-compressible model substitutes the density of the basic field for the density of the continuity equation. The basic field is a horizontally uniform field for which the hydrostatic equilibrium approximation holds. Although the quasi-compressible model includes sound waves, its accuracy is not significantly different from that of the anelastic model. The fully compressible system model predicts sound waves without including approximations like those of the quasi-compressible model. In the early 1990s, non-hydrostatic models described by quasi-compressible equations were studied (e.g. Ikawa and Saito 1991, Pielke et al. 1992, Tuboki and Sakakibara 2001). Subsequently, studies using non-hydrostatic models described in fully compressed form became mainstream in research and operation (e.g. Saito et al. 2006, Skamarock et al. 2008, Satoh et al. 2008, Brown et al. 2012). The first non-hydrostatic model to be developed for practical use by the operational NWP center was the MetOffice in the United Kingdom (Carpenter 1979). Since then, many non-hydrostatic models have been developed and put into operation by NWP centers in the world. The main non-hydrostatic models used by the world's operational centers are listed below. The UK Met Office has been operating the Unified Model (UM; Brown et al. 2012) which is a global model with a variable grid and a mid-latitude grid spacing of

10 km. In UK Met Office, a limited-area NWP model based on UM with a horizontal grid spacing of 1.5 km is also in operation for the area around the United Kingdom (Tang et al., 2013). Icosahedral Nonhydrostatic (ICON; Zängl et al. 2015) model is the Deutscher Wetterdienst's (DWD's) global model with a grid spacing of about 13 km. ICON-EU with a horizontal grid spacing of ~ 7 km and ICON-D2 with a horizontal grid spacing of ~ 2.2 km is also in operation as a regional model. The United States operates the Global Forecast System (GFS) with a horizontal grid spacing of 13 km, which uses the Finite-Volume Cubed-Sphere Dynamical Core (FV3). The FV3 is a scalable and flexible dynamical core capable of both hydrostatic and non-hydrostatic simulations and was implemented operational system as a limited-area model in 2019. In addition, several regional models based on Weather Research and Forecasting (WRF; Skamarock et al. 2008) are in operation for North America. The Meteo France operates the non-hydrostatic model “Application of Research to Operations at Mesoscale” (AROME; Seity et al., 2011) with a horizontal grid spacing of 1.3 km as a regional model.

In Japan Meteorological Agency (JMA), the non-hydrostatic model (NHM; Ikawa and Saito 1991) was developed at the Meteorological Research Institute in the 1980s, and the results of the Numerical Prediction Division of JMA were incorporated into NHM to develop JMA-NHM (Saito et al. 2006). JMA-NHM began operating as the Meso-Scale Model (MSM) in 2004. In 2006, The horizontal grid spacing of MSM was upgraded from 10 km to 5 km. In 2012, the Local Forecast Model (LFM) with a grid spacing of 2 km using the meso-model as a boundary condition was put into operation. The JMA non-hydrostatic model “ASUCA is a System based on a Unified Concept for Atmosphere” (ASUCA; Ishida et al. 2022) was started to develop in 2007, introduced into the LFM in 2015, and into the MSM in 2017. There are several non-hydrostatic models developed in Japan for research purposes. For example, the Cloud Resolving Storm Simulator (CReSS) at Nagoya University (Tsuboki and Sakakibara, 2001,2002), The Non-hydrostatic Icosahedral Atmospheric Model (NICAM) at the University of Tokyo (Tomita and Satoh, 2004; Satoh et al. 2008; Satoh 2013) NICAM, and RIKEN's SCALE (Nishizawa et al. 2015).

The NWP model we focus on in this study is non-hydrostatic, and is a regional model with the forecast domain limited to the area around Japan. The phenomena targeted in this study are on scales smaller than the synoptic scale and, following the classification of Orlanski (1975), are on the meso-beta to micro-alpha scale. The meso-beta scale ranges from 20 to 200 km, and corresponds to squall lines. The meso-gamma scale is 2 to 20 km and corresponds to thunderclouds. The micro-alpha scale is 200 m to 2 km and corresponds to deep convection. This study discusses meteorological phenomena larger than deep convection. Meteorological phenomena that can be predicted by numerical models are considered to be about five times larger than the grid spacing of the model; the grid spacing of the model used in this study is between 5 km and 50 m. There is a limit to the high resolution of hydrostatic models because the hydrostatic equilibrium approximation becomes less valid when the grid spacing is less than 10 km. On the other hand, non-hydrostatic models have no problem achieving high resolution below km-scale. However, when the non-hydrostatic model has a grid spacing of 1 to 5 km, meteorological phenomena can be

divided into two categories: those with scales that can be resolved on a discretized grid and those with scales that cannot. Phenomena reproduced on discretized grid points are called grid-scale phenomena. Phenomena on scales smaller than the grid points are called subgrid-scale. Therefore, the parameterization is used to compute sub-grid scale phenomena as grid averages. The parameterization involves many errors because it approximates physical phenomena that cannot be explicitly computed in the model, and it also depends on the grid spacing. Ideally, as the grid spacing is reduced, sub-grid scale phenomena should be able to be predicted as grid-scale phenomena. However, conventional parameterizations are often optimized for a particular resolution and behave unphysically as the grid spacing is reduced. The resolution at which the parameterization is no longer valid is called the “gray zone”. For the boundary layer scheme, the gray zone ranges roughly from 200 m to 2 km (Honnert et al. 2020). This means that NWP models with a grid spacing of several kilometers are included in the gray zone, making the physical scheme less reliable. In recent years, many studies have been conducted on the gray zone problem, and some solutions, though limited, have been proposed (e.g. Wyngaard 2004, Field et al. 2017, Honeert et al. 2020).

The spatial resolution of numerical forecast models continues to improve as computing power increases. If the grid spacing becomes small enough that the resolution breaks through the gray zone, the need for parameterization decreases. For example, if the grid spacing is reduced to a few hundred meters where cumulus clouds can be resolved, the need for convective parameterization is reduced and predictions can be made almost entirely with cloud microphysics schemes. It is also believed that a resolution of less than 100 m is necessary to explicitly reproduce the detailed structure inside the boundary layer. Numerous studies have been conducted using high-resolution models. In the operational NWP centers, the UK Met Office has been developing 500 m resolution model for future operations and parameterization studies (<https://www.metoffice.gov.uk/research/foundation/parametrizations/high-resolution>). The use of a high-resolution model allows parameterization to be eliminated and allows for refinement of the physics scheme to handle grid-scale phenomena. Based on the physical scheme of the refined high-resolution model, it is also possible to improve the parameterization of the gray zone. However, some physics schemes for grid-scale phenomena are modeled while the physical processes remain unresolved. The cloud microphysics scheme is one such example, and its high uncertainty is a source of discrepancy between predictions and observations. To bridge this gap, it is necessary to understand the physical processes that contribute to the uncertainty in the predictions.

1.2. Cloud microphysics

In NWP models, the effective resolution is determined by the grid spacing defined during spatial discretization. In the prediction of NWP models, the cloud microphysics scheme is responsible for the time evolution of clouds and precipitation at that grid-scale. Cloud microphysics process schemes used in numerical forecast models include the bulk method, the bin method, and the super-droplet method. The bulk method is a scheme that classifies hydrometeors into different categories, such as cloud water, rain, cloud

ice, snow, and graupel, and uses lower-order moments as prognostic variables. The bin method predicts physical quantities, such as particle mass assigned to a bin, without a priori assumption of particle size distribution. The super-droplet method uses the particle method to calculate the motion of a particle, and in principle can calculate the change of state of a particle without parameterization. The bulk method is more computationally efficient than the other two methods and is used in operational models. The bulk method was first introduced by Kessler (1969) as warm rain physics for cloud water and rain. Kessler assumed the rain particle size distribution to be an exponential function and used an autoconversion scheme to represent the growth of clouds by accretion and the conversion from clouds to rain. It is called a one-moment scheme because it predicts only the mixing ratio, which is a third-order moment of the size distribution function. This bulk method was extended to include ice particles (e.g., Cotton 1982; Lin et al. 1983; Rutledge and Hobbs 1984). A two-moment scheme was also proposed that predicts not only the ice mixing ratio but also the number concentration, a zeroth-order moment (e.g., Ziegler, 1985; Ferrier, 1994; Cohard and Pinty, 2000; Morrison et al. 2005). There is also a three-moment method in which the reflectivity, which is the sixth moment, is the predictor (Milbrandt and Yau, 2005a, 2005b).

Ice is difficult to deal with because of its diversity. Early cold rain schemes (e.g., Lin 1983) used ice categories of cloud ice, snow, and graupel as predictors; Ferrier (1994) predicted hail in addition to cloud ice, snow, and graupel; Straka and Mansell (2005) introduced 10 types of ice; Morrison and Milbrandt (2015) developed the predicted particle properties (P3) bulk scheme. P3 prognoses four ice mixing ratio variables, total mass, rime mass, rime volume, and number, using a single category.

The shape of ice particles is not as simple as raindrops, but very complex. For example, bin models, which are more advanced than bulk models, have been proposed to track ice habits (Chen and Lamb, 1994; Hashino and Toripoli, 2007, 2011). Bulk schemes often have been formulated assuming that ice particles are spherical for computational efficiency and simplicity. The following is an example of a bulk scheme where the ice shape is considered non-spherical: Straka and Mansell (2005) use the mixing ratio of 10 different ice particles as a prognostic variable. Different formulations of the terminal velocity are set for each particle. Ice particles are assumed to be plates and columns, each with a different capacitance. Snow particles are assumed to be aggregations of snow crystal only; Thompson's scheme (Thompson et al., 2008) gives the capacitance of snow as a function of temperature. The capacitance linearly decreases from spherical value to plate value as temperature increases from -30° to -15°C . However, the velocity of snowfall does not include shape dependence; Harrington et al. (2013) proposed a bulk method to predict the aspect ratio of particles and calculate diffusion growth for water vapor; Jesen and Harrington (2015) showed that riming between particles with different aspect ratios effect between particles with different aspect ratios. Jesen et al. (2017) extended Harrington et al. (2013) for predicting the aspect ratio of particle shapes based on Jesen and Harrington (2015).

In this study, the cloud microphysics scheme used is based on the bulk scheme. The predictor variables are the low-order moments of the particle population, such as the number concentration and mixing ratio of each category. In the bulk scheme, aqueous materials are classified into several categories. The interactions between the classified particles are modeled under a variety of assumptions. Because there are many unresolved aspects of the cloud water deposition process in reality, the assumptions made during this modeling process are subject to many errors.

1.3. Planetary boundary layer

The planetary boundary layer (BL) scheme controls vertical mixing inside the BL and is responsible for the transport of heat, water vapor, and momentum in the NWP models. Vertical mixing inside the BL of the atmosphere is highly influenced by turbulence. The turbulence of various scales exists inside the BL. The BL scheme is responsible for subgrid-scale turbulent phenomena. Therefore, the effectiveness of the BL scheme depends on the size of the model grid spacing.

Currently, there are two main types of boundary layer schemes widely used in numerical forecast models. One is called the Large Eddy Simulation (LES) model and the other is called Reynolds Averaged Navier-Stokes (RANS) model. LES treats eddies smaller than the grid size as parameterized eddy viscosity and explicitly computes eddies larger than the grid size; RANS treats the flow in the grid as an ensemble average and further parameterizes the scale eddies that contribute to the vertical transport of momentum and heat. RANS targets Reynolds averages, which are less variable than LES. RANS has the advantage of being less computationally demanding than LES. However, RANS requires more parameterizations and has greater model uncertainty than LES. Therefore, LES is often a simpler and more universal model than RANS, although more computational resource with high-resolution $O(100\text{m})$ or less is required. The first LES was developed by Smagorinsky (1963) and an improved version was presented by Deardorff (1980) in the meteorological application. At JMA, the Deardorff (1980) scheme has been introduced into JMA-NHM and used to study high-resolution models.

Mellor and Yamada (1974, 1982) constructed the Mellor-Yamada (MY) scheme which belongs to the RANS model using a system of fundamental equations that approximates the flow in a grid by an ensemble average. In the MY model, the second-order turbulent closure model with the least approximation is called level 4. In addition to that, other models have been proposed such as level 3, 2.5, 2, and 1 with simplifications depending on the degree of isotropy of the turbulence. Level 3 is numerically difficult to compute stably because there are more forecast equations to solve and the diffusion coefficient can be negative (which represents counter gradient diffusion). Nakanishi and Niino (2004, 2006) improved the computational stability of this Level 3 model. Nakanishi and Niino (2009) improved the scheme by determining the unknown constants of the MY scheme using the result of LES as a reference value. This improved scheme is called the MYNN scheme, and JMA has introduced MYNN level 3 into the operational model

(Hara et al. 2007). It has also been implemented in many models such as the Model for Interdisciplinary Research on Climate (MIROC; Watanabe et al. 2010), NICAM, and WRF.

The behavior of the BL of TCs (hereafter referred to as the tropical cyclone boundary layer, TCBL) is very different from that of the BL under calm conditions in terms of the existence of roll vortices (rolls), which are nearly aligned in the tangential direction, and of associated vertical transport of momentum (e.g., Kepert 2001; Kepert and Wang 2001; Foster 2005; Nolan et al. 2009a,b; Gao and Ginis 2014).

Many studies of the TCBL have shown the presence of various types of small-scale organized structures inside the BL (Gall et al. 1998; Wurman and Winslow 1998; Morrison et al. 2005; Zhang et al. 2008; Koshiba et al. 2013; Ito et al. 2017). Morrison et al. (2005) reported the presence of rolls with horizontal wavelengths of about 1500 m below altitudes of 800 m. Rolls in the TCBL are a series of large turbulent eddies that are aligned along the mean azimuthal wind direction in the lower layer of TCs. Such rolls are developed in the vertical wind shear (e.g., Brown 1980; Etling and Brown 1993). Ito et al. (2017) found three types of rolls, and their basic mechanism has not been fully understood. Rolls in the TCBL have been studied in detail (e.g., Wurman and Winslow 1998; Morrison et al. 2005; Ellis and Businger 2010; Li et al. 2021), and are known to be responsible for the vertical transport of energy in the TCBL (e.g., Foster 2005; Nolan 2005; Gao and Ginis 2014).

A few observational studies have focused on the detailed structure of the rolls in TCs. For example, Wurman and Winslow (1998) showed the results of remote sensing observations of the rolls. Lorsolo et al. (2008) show the rolls observed by Doppler radar in Hurricanes Isabel (2003) and Frances (2004). The height scale of TCBL and the vertical eddy diffusivity in TCBL have been investigated using dropsonde and aircraft observation, respectively (Zhang et al. 2011; Zhang et al. 2012). More recently, Kosiba and Wurman (2014) reported observations at high temporal resolution for TCs. To advance knowledge of TC structure and the process of TC intensification, meteorological elements in the BL of TC eyewalls have been measured by small unmanned aircraft systems (e.g., Cione et al. 2020). In addition, Tang et al. (2021) evaluated the momentum flux due to the rolls using aircraft observation and estimated the momentum flux with the rolls, which was about two or three times higher than that without the rolls. This result suggests that the representation of the rolls in the TCBL affects the accuracy of predictions of the detailed structure of TCs.

The effects of BL schemes on the structure of tropical cyclones in simulations have been examined by conducting both ideal and realistic numerical experiments. Nolan et al. (2009a, b) compared local and higher-order schemes to analyze the detailed structure of the BL, whereas Kepert (2010a, b) compared higher-order closure and a simple non-local closure in linear/nonlinear models. These studies produced similar results for the BL flow in the inner core of the cyclone, but significantly different results at the radius where subsidence occurred. This is because the higher-order closure was more sensitive to the resulting increase in static stability at the radius where subsidence occurred. In addition, using a large eddy

simulation (LES), Nakanishi and Niino (2012) investigated the formation mechanism and importance of the horizontal rolls in a near-neutrally stratified TCBL. They showed that rolls with a horizontal wavelength of 1.5–2.4 km are generated due to the inflection-point instability of the radial velocity profile. They argued that in the upper part of the TCBL, internal gravity waves, Kelvin-Helmholtz waves, and entrainment are generated and partially coupled with rolls that enhance vertical transport. Ito et al. (2017) conducted LESs over a whole domain of a tropical cyclone for an ideal experiment with a grid spacing of 100 m over an area of 2,000×2,000 km². They showed that three types of rolls are generated inside the TCBL. Gao and Ginis (2016) evaluated the horizontal momentum flux parallel to the rolls and orthogonal to the rolls, which cannot be controlled by the PBL scheme, by analyzing an TCBL simulated by LESs. They found that the momentum flux parallel to the rolls was not correlated with the vertical shear and could not be represented by a PBL scheme based on the classical K-theory (e.g., Stull 1988).

Most studies of real tropical cyclones have focused on the turbulence characteristics of rolls by performing high-resolution simulations in a localized region within a tropical cyclone. For example, Li et al. (2021) compared an LES and a simulation with a PBL scheme using a high-resolution model for a TC. In their validation of the simulations, LES was better at simulating the vertical structure of TC winds and precipitation over the ocean. The simulation with the PBL scheme overestimated the precipitation associated with TCs over the ocean. At landfall, the strong negative momentum fluxes from the PBL scheme resulted in unrealistically strong TCs that decayed faster than they did before landfall. By contrast, weak negative momentum fluxes in the LES maintained strong winds; Li et al. (2021) argued that the effects of the rolls on TC winds and precipitation at landfall are not yet fully understood.

Recent improvements in computing power have facilitated the use of atmospheric models for numerical simulations at grid spacings of hundreds of meters, which is comparable with the length scales of the turbulence that dominates in the BL. However, in this “gray zone” region of the BL, neither LESs, which are ideally used for atmospheric models with very high resolutions (tens of meters), nor Reynolds Averaged Navier-Stokes (RANS) equation models, which are used for traditional meteorological models with resolutions of several kilometers that use a PBL scheme, are appropriate, because basic assumptions about parameterization for both the LES and RANS are violated. As reviewed by Honnert et al. (2020), various studies have been carried out on the predictive performance of PBL schemes in the gray zone. However, there is a paucity of studies comparing the properties of PBL schemes for TC simulations in the gray zone. In particular, there is a lack of studies comparing models and observations at this resolution to evaluate numerical results in the gray zone.

1.4. Evaluation of NWP against remote sensing

Forecast errors in the NWP models are largely due to the uncertainty of these physical schemes. To quantitatively measure the uncertainty of a scheme, the model is compared to observations. Predicted physical quantities in the model are difficult to compare directly with observations because many physical

quantities are difficult to observe directly. Therefore, pseudo-observations are created from clouds and precipitation in the numerical model predictions and compared with actual observations for validation of the NWP model.

Numerical weather forecasting is made worldwide by weather forecast centers such as JMA, ECMWF, and UK Met Office. In those weather forecast centers, the initial condition of NWP models is created by the data assimilation method. The data assimilation method compares model predictions with observations to reduce errors between observations and models and produces plausible atmospheric conditions. Therefore, model-observation comparisons are routinely performed in the operational center. In the data assimilation, it is expected that there will be no bias between models and observations. In reality, however, there is a bias between observation and model. When a bias is found to exist between the observations and the model, data assimilation is performed to correct for that bias. Even if the observation doesn't have a bias and the model has a bias, the observation is corrected to avoid the effects of bias. In the field of data assimilation, the variational bias correction method (e.g., Dee 2004), which corrects for bias sequentially, has been established and put into practical use. However, if the model has a bias, it is necessary to reduce the bias by improving the model itself, rather than correcting the bias. In other words, improving the model not only improves the forecast accuracy, but also improves the accuracy of the model's initial condition.

To validate the hydrometeors predicted by the cloud microphysics scheme, it is necessary to obtain information on hydrometeors in the actual atmosphere. Weather radar provides a wide range of steady-state observations of atmospheric hydrometer conditions. Precipitation distribution data from radar observations are indispensable for disaster prevention as well as for model validation. Microwave radar began to be used for precipitation observation in the 1940s. Before that, Rayleigh (1871) showed that backscattering by precipitation particles was proportional to the sixth power of particle size. Mie (1908) showed that rigorous calculations are required for scattering calculations by particles that are about 1/10 smaller in diameter than the radar wavelength. Ryde (1946) estimated reflectivity and attenuation based on these scattering theories. Marshall and Palmer (1948) showed the relationship between reflectivity and precipitation intensity. These were the beginnings of radar meteorology. In the United States, Doppler radar began to be used in the 1950s (e.g., Brantley and Braczy 1957; Atlas 1964). This Doppler radar was fixed in the vertical direction and used to measure terminal velocity and estimate size distribution. In the 1970s, with the development of data processing technology, it became possible to process data while scanning. In the 1990s, a U.S. radar network, Next Generation Weather Radar (NEXRAD), began operations (Crum and Alberty, 1993), and NEXRAD was upgraded to dual polarimetric radar in 2011. JMA began operating weather radar in 1954. Later in 1995, Doppler radar began operating at Kansai International Airport, and since 2015, existing radars have been updated to polarimetric radar.

Radar observations have been made from space as well as from the ground. The Tropical Rainfall Measuring Mission (TRMM) satellite equipped with precipitation radar (PR) was launched in 1997 (Kozu et al. 2001). The PR was a Ku-band phased-array radar and was the world's first satellite-borne radar. TRMM continued to observe for 17 years, well beyond its 3-year design life, and operated until 2015. In 2006, CloudSAT with Cloud Profiling Radar (CPR) was launched; CPR has a frequency of 94 GHz and is a cloud radar sensitive to ice particles. The Global Precipitation Measurement (GPM) core satellite, launched in 2014 as the successor to TRMM, carries the Dual-frequency Precipitation Radar (DPR), which was jointly developed by Japan Aerospace Exploration Agency (JAXA) and National Institute of Information and Communications Technology (NICT). DPR is a Ku- and Ka-band phased-array radar that can simultaneously observe precipitation at two frequencies, allowing it to diagnose differences in the types of hydrometeors inside a precipitation system. TRMM Microwave Imager (TMI) and GPM Microwave Imager (GMI), which are loaded on the same platform as the spaceborne precipitation radar, provide horizontal distribution of the precipitation information, which also can be used for model validation. These microwave imagers can detect microwave signals that are scattered by cloud ice at a high-frequency band over 89 GHzV (where V is a vertically polarized wave element) and can be used for cloud ice validation. The advantage of these satellite-based instruments is that they are capable of global observation, not limited to land.

Many previous studies have compared NWP models with Earth observation satellites. Verification of cloud microphysics schemes requires information on the vertical structure of hydrometeors. Space-borne radar can observe information on the distribution of hydrometeors inside the precipitation system globally. Several previous studies have quantitatively validated models using space-borne radars (e.g., Eitzen and Xu 2005; Zhou et al. 2007; Masunaga et al. 2008; Eito and Aonashi 2009; Matsui et al. 2009; Roh and Satoh 2014). Eito and Aonashi (2009) validated the NWP model using TRMM/PR, TMI, and ground radar and quantified the errors in the cloud microphysics scheme. Matsui et al. (2009) proposed a validation method for a cloud-resolving model (CRM) using the multiple sensors of TRMM/PR and TMI, called TRMM Triple-Sensor Three-Step Evaluation Framework (T3EF). Masunaga et al. (2010) stated that many of the model predictions are physical quantities that are not stationary and cannot be observed extensively. This makes it difficult to know the true state of the predictor variable. Therefore, they state that a better strategy is to simulate observations from model predictions and compare the simulated observations with the actual observations. Masunaga et al. (2010) provided one direction in which the validation of weather phenomenon forecasts can proceed.

To further validate models using various earth observation satellites, the Joint-Simulator (Joint simulator for satellite sensors; Hashino et al. 2013) was developed with the Satellite Data Simulator Unit (SDSU: Masunaga et al. 2010) at its core. The advent of this Joint-Simulator has led to significant progress in model validation using satellite observations (e.g., Hashino et al. 2013,2017; Roh and Satoh 2014; Roh et al. 2017,2020; Seiki and Roh 2020). Hashino et al. (2013, 2016) compared CloudSat, CALIPSO, and

Clouds and the Earth's Radiant Energy System Aqua with models using the Joint-Simulator, which is a package of highly accurate satellite simulators developed for the EarthCARE satellite mission (Illingworth et al. 2015). Duruisseau et al. (2018) validated the model by simulating GPM/DPR and CloudSat/CPR using the enhanced rapid radiative transfer for TOVS for scattering (RTTOV-SCATT; Bauer et al. 2006; Saunders et al. 2018) developed by the European Organisation for the Exploitation of Meteorological Satellites (EUMETSAT). Roh and Satoh (2014) and Roh et al. (2017) improved the cloud microphysics scheme of a CRM based on T3EF. Roh et al. (2017) extended a multisensor satellite radiance-based evaluation for CRMs. Roh et al. (2020) proposed a model validation method of thermodynamics of hydrometeors using the depolarization ratio and total attenuated backscatters of CALIPSO. Seiki and Roh (2020) improved the cloud microphysics scheme based on the validation results to improve prediction accuracy.

In the field of operational data assimilation, the bias between observations and simulations is a critical factor affecting the analysis accuracy. Okamoto et al. (2016) showed the existence of model bias by comparing GPM/DPR and models, and Ikuta et al. (2021) corrected the bias using GPM/DPR in assimilation. Fielding and Janisková (2020) highlighted the necessity to correct the bias in CloudSat direct assimilation. To assimilate microwaves, such as GPM/GMI, it is assumed that a systematic bias exists over cloud regions between models and observations; these biases must be carefully corrected before assimilation (Geer and Bauer 2011). Results of previous studies indicate that the prediction accuracy of models and analysis accuracy of spaceborne radar and microwave assimilation depend on the predicted hydrometeors in the models (Chambon et al. 2014; Geer et al. 2018).

Recently, models have also been validated using ground-based dual-polarimetric radar. A dual-polarimetric radar provides information on the shape of precipitation particles. Jung et al. (2008) developed a radar simulator for polarimetric parameters including reflectivity, differential reflectivity, and specific differential phase in horizontal and vertical polarization. The simulator is a forward observation operator of S-band polarimetric radar for data assimilation. In the simulator, the T-matrix method is used to calculate the backscattering of raindrops, while the Rayleigh scattering approximation is applied to snow and hail particles. Squall lines and supercells are simulated and it is shown that the polarimetric signature is well captured by the simulator. Jung et al. (2010) also investigated the ability of the simulator to simulate the polarimetric signatures in the case of a supercell storm. The simulations were compared to the double-moment scheme and the single-moment scheme. The results point out the limitations of the single-moment method with a slope parameter that is independent of the mixing ratio. The usefulness of a well-designed radar simulator for validating numerical models was also demonstrated. Ryzhkov et al. (2011) developed a radar observation operator to simulate polarimetric radar. The model covered by this simulator includes seven classes of hydrometeors, each class represented by a 43-bin size distribution function. Evaluation in the hailstorm case showed that the polarimetric parameters are in general agreement with the observations. A relationship between the microphysical data and the polarimetric signatures is also

presented. Putnam et al. (2017) simulated polarimetric parameters using storm-scale ensemble forecasts and compared them to observations. Five different MP schemes were used for their ensemble predictions, including single-moment and double-moment schemes. The performance of each scheme was investigated and the presence of model bias was discussed. Matsui et al. (2020) validated several cloud physics schemes using dual-polarimetric radar. Simulations of dual-polarimetric radar observations were performed by POLARimetric Radar Retrieval and Instrument Simulator (POLARRIS: Matsui et al. 2019). In reality, solid precipitation is a mixture of particles of various shapes, but model snow is often assumed to be spherical. The observed polarimetric parameters of solid precipitation in such models differ significantly from the observed polarimetric parameters (e.g., Matsui et al. 2019; Matsui et al. 2020). Shrestha et al. (2022) performed an ensemble simulation for northwestern Germany. From these predictions, they performed polarimetric X-band radar simulations and compared them with observations. The predictions underestimated the convective area fraction, high reflectivities, and the width/magnitude of the differential reflectivity column, and underestimated the frequency distribution for high precipitation. As reviewed by Morrison et al. (2020), cloud microphysics schemes are composed of a combination of numerous modeled processes. The processes involved in solid particles are very complex and have many unexplored aspects. In particular, very few studies have quantitatively estimated the impact of ice and snow shape on forecasts. Verification using polarimetric radar reveals the certainty of prediction accuracy for particles with complex shapes. Some studies of cloud physics using dual-polarimetric radar have made progress in the U.S. and Germany. In Japan, the project of the ULTra-sIte for Measuring Atmosphere of Tokyo metropolitan Environment (ULTIMATE: Satoh et al. 2022) has also validated and compared several models using dual polarimetric radar and a disdrometer.

1.5. The objective of this study

In this study, the physical scheme will be validated by utilizing the NWP model and satellite, ground-based radar, and disdrometer observations. Using the validation results, we improve the cloud microphysics scheme and identify physical processes that contribute to improving the reproducibility of the vertical structure of the precipitation system. The influence of the physical processes on the atmosphere will also be clarified in terms of precipitation, BL, and model resolution. Chapter 2 of this thesis presents the validation and improvement of the cloud microphysics scheme using satellite observations; Chapter 3 presents the validation and improvement of the cloud microphysics scheme using polarimetric radar and optical disdrometer; Chapter 4 presents the validation of the turbulence scheme using polarimetric radar to clarify the model resolution dependence; and Chapter 5 presents the validation of the cloud microphysics scheme using polarimetric radar to clarify the model resolution dependence. Chapter 6 discusses the results obtained from this study, and Chapter 7 describes a comprehensive summary.

2. Method

2.1. NWP model

In this study, the non-hydrostatic model ASUCA (A System based on a Unified Concept for Atmosphere; Japan Meteorological Agency, 2019; Ishida et al. 2022) from the JMA is used to conduct numerical simulations. ASUCA forms the basis of the Meso-Scale Model (MSM) and Local Forecast Model (LFM). MSM and LFM are the JMA's regional NWP systems. The JMA operates the MSM and LFM to provide disaster prevention information. Figure 2.1 shows the domain of the MSM and LFM, which covers Japan and its surroundings. The horizontal grid spacing of MSM and LFM is 5 km and 2 km, respectively. The boundary condition of MSM is provided by Global Spectral Model (GSM) at JMA. The MSM is used as the boundary condition of the LFM. For the operational simulations, we used the Kain and Fritsch (Kain 2004) scheme for the convection scheme, the one-moment cloud microphysics scheme (Ikuta et al. 2021a), and the Mellor-Yamada-Nakanishi-Niino level 3 (MYNN3; Nakanishi and Niino 2009) scheme for the PBL scheme. The surface flux scheme was implemented according to Beljaars and Holtslag (1991). Land use information for the model's grid was taken from numerical map information with a resolution of 50 m provided by the Geospatial Information Authority of Japan. The initial conditions of the MSM were provided by the Meso-scale Analysis, which is the four-dimensional variational method version of the variational data assimilation system based on ASUCA (ASUCA-Var; Ikuta et al. 2021b). The model's configuration differs in each chapter of this paper. Therefore, details of the model's configuration are described in each chapter.

2.2. Integrated satellite simulators

From the output data of the NWP model, the sensor signals of GPM (DPR, GMI) are simulated using satellite simulators for each sensor. In addition, ground-based dual-polarimetric radar is also simulated by the satellite simulator. The package of the satellite simulators used at JMA is referred to as the I-simulator, which is described here.

For GMI, we use RTTOV-SCATT. The coefficient files used for radiation transfer calculations were recreated based on the cloud microphysics scheme in the ASUCA configurations. Cloud water, rain, cloud ice, snow, and graupel are effective hydrometeors. Particles of cloud water, rain, and graupel are spherical whereas that of cloud ice and snow are in the shape of thick hex plates and Liu's type-A snowflake (Liu 2008), respectively. The cloud fraction in the cloud microphysics scheme (see section 2.1) determines the cloud cover in the grid. The definitions of particle mass and size distribution are the same as those of ASUCA.

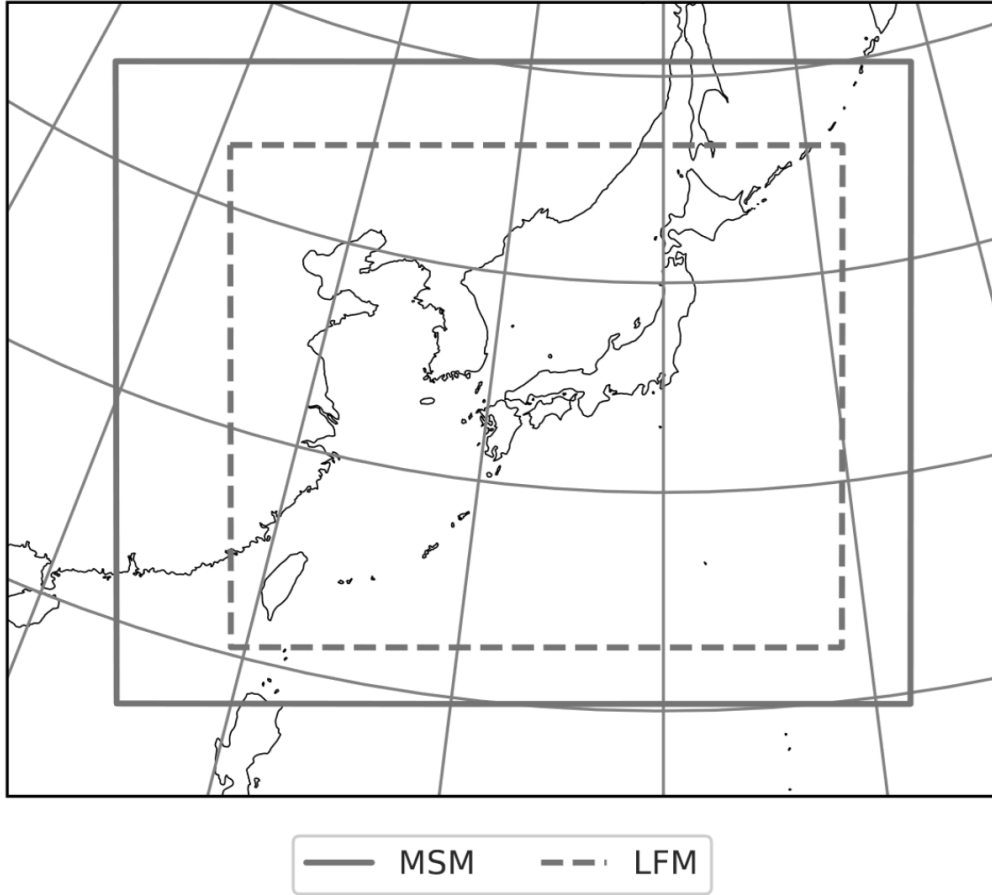


FIG. 2.1. Domain of MSM (solid) and LFM (dashed) at JMA.

For DPR simulations, we developed a DPR simulator. The DPR simulator is an extended version of the radar simulator developed as an observation operator in DPR assimilation (Ikuta et al. 2021). The observation operator for the assimilation is a very simplified simulator that ignores cloud particles and uses only Mie scattering. On the other hand, this study mainly enhances the scattering calculation process in the I-simulator. The DPR simulator should verify the microphysics of clouds in the NWP model so that it can perform more advanced simulations than those used in data assimilation. An overview is given here. The particles used in the DPR simulations are cloud water, rain, cloud ice, snow, and graupel. Particles of cloud water, rain, and graupel particles are assumed to be spherical. Particles of cloud ice and snow are in the shape of hex plate and sector-like defined by Liu's sector snowflakes (Liu 2008). Scattering coefficients are derived from the scattering database (<http://cirrus.met.fsu.edu/research/scatdb.html>; Liu 2008).

The DPR simulation is given by the following procedure regarding the GPM/DPR Level-2 algorithm (Iguchi et al. 2018; Seto et al. 2021). The effective radar reflectivity factor is given as

$$Z_e = \frac{\lambda^4}{\pi^4 |K|^2} \int \sigma_b n(D) dD \quad (2.1)$$

where λ (m) is the wavelength of the radar, $K = (m^2 - 1)/(m^2 + 2)$, m is the complex refractive index, σ_b (m^2) is a backscattering cross section of hydrometeor particles, $n(\cdot)$ (m^{-4}) is a PSD function, and D (m) is diameter. The precipitation-specific attenuation k ($dB\ km^{-1}$) is given as

$$k = c_k \int \sigma_e n(D) dD, \quad (2.2)$$

where $c_k = 0.01 \ln(10)$ and σ_e (m^2) is the total extinction cross section. The attenuation is integrated from space to the target altitude. The measured reflectivity factor Z_m is given as

$$10 \log_{10} Z_m = 10 \log_{10} Z_e - 2 \int_0^r k(s) ds, \quad (2.3)$$

where r is the length of the integrated path from the satellite to the target altitude. The measured dual-frequency rate (DFR_m; Le and Chandrasekar 2013) is defined as

$$DFR_m = Z_m(Ku) - Z_m(Ka) \quad (2.4)$$

where $Z_m(Ku)$ is the reflectivity of KuPR and $Z_m(Ka)$ is the reflectivity of KaPR. DFR_m is calculated only at the point where both $Z_m(Ku)$ and $Z_m(Ka)$ exist. The σ_b and σ_e are stored in advance in a database for each particle type. For the actual calculation, the scattering coefficients for each particle are obtained using the LUT method using the database, integrated by the particle size, and then summed for all the particles. The simulated DFR_m is a signal that cancels out almost of the bias caused by the error in the assumption of simulator. Therefore, verification using DFR_m allows us to evaluate the model with reduced errors by the simulator uncertainty. The bright band due to melted ice-phase particles is simply simulated using the average dielectric constant of ice and liquid based on Fabry and Szyrmer (1999) at temperatures above 0°C. The minimum detectable reflectivity is set as 16 and 18 dBZ for KuPR and KaPR, respectively. If the simulated reflectivity is below the minimum detectable reflectivity, the data are regarded as non-hydrometeors. Random noise is added to the simulation using a normal distribution PDF with a variance of 1 dB following the receiver power accuracy of the DPR (Iguchi et al. 2018).

Note that brightness temperature (T_B) at the high-frequency band (≥ 89 GHz) clearly depends on the assumption of the particle shape (e.g., Barreyat et al. 2021). However, the difference in T_B depending on such particle shape is smaller than the improvement in this study, as shown in section 3.3. In addition, the range of diameter for snow particle in the model and the simulator are also different. Specifically, the

range of snow diameters in the MSM is defined as 100–20 000 μm based on Field et al. (2007), while the range of Liu’s type-A snowflake diameter in the I-simulator is defined as 50–10 000 μm based on Liu (2008). Moreover, although the impact is expected to be limited, there are various uncertainties in the beam shape and cloud inhomogeneity. Therefore, for more sensitive and quantitative evaluation beyond this study, the simulation results need to be carefully checked and used, taking into account that the simulator is imperfect.

We enhanced the I-simulator for the simulation of a dual-polarimetric radar. The polarimetric parameters are computed by the LUT method. The LUT was made by the POLARRIS module in the Joint-Simulator. POLARRIS computes the single scattering of the non-spherical particle by the method of T-matrix (e.g., Mishchenko et al. 1996) and Mueller-matrix (Vivekanandan et al., 1991). The Muller scattering matrix \mathbf{S}_x (mm^2) for category x which indicates hydrometeor species is 4×4 matrix given by Eq. (2.2) in Vivekanandan et al. (1991). The Muller scattering matrix summed over total hydrometeor species is given as:

$$\mathbf{S}|_{\text{tot}} = \sum_x \int \mathbf{S}_x n_x(D) dD. \quad (2.5)$$

The LUT is a database of the Muller matrices for each temperature, mass of hydrometeors, and incident angle. The simulated polarimetric parameters are computed using the Muller matrices in the LUT. The horizontally polarized reflectivity $Z_{\text{hh}}(\text{mm}^6 \text{m}^3)$, vertically polarized reflectivity $Z_{\text{vv}}(\text{mm}^6 \text{m}^3)$ and differential reflectivity $Z_{\text{DR}}(\text{dB})$ are given as:

$$Z_{\text{hh}} = \frac{4\lambda^4}{\pi^4 |K|^2} \left(\frac{S_{11}|_{\text{tot}} - S_{12}|_{\text{tot}} - S_{21}|_{\text{tot}} + S_{22}|_{\text{tot}}}{2} \right), \quad (2.6)$$

$$Z_{\text{vv}} = \frac{4\lambda^4}{\pi^4 |K|^2} \left(\frac{S_{11}|_{\text{tot}} + S_{12}|_{\text{tot}} + S_{21}|_{\text{tot}} + S_{22}|_{\text{tot}}}{2} \right), \quad (2.7)$$

and

$$Z_{\text{DR}} = 10 \log_{10} \left(\frac{Z_{\text{hh}}}{Z_{\text{vv}}} \right). \quad (2.8)$$

Horizontally polarized reflectivity $Z_{\text{HH}}(\text{dBZ})$ and vertically polarized reflectivity $Z_{\text{VV}}(\text{dBZ})$, using uppercase letters for subscripts, are defined as follows:

$$Z_{\text{HH}} = 10 \log_{10}(Z_{\text{hh}}) \quad (2.9)$$

and

$$Z_{\text{VV}} = 10 \log_{10}(Z_{\text{vv}}). \quad (2.10)$$

The attenuation due to hydrometeors on the beam path is calculated, and the attenuated reflectivity is used as the equivalent of the measurement value.

Specific differential phase K_{DP} (deg km⁻¹) is given as

$$K_{DP} = 1000 \frac{180}{\pi} \text{Im}(M_{hh}|_{\text{tot}} - M_{vv}|_{\text{tot}}), \quad (2.11)$$

where

$$M_{hh}|_{\text{tot}} = \frac{\lambda}{1000} f_{hh}^{(0)}|_{\text{tot}}, \quad (2.12)$$

$$M_{vv}|_{\text{tot}} = \frac{\lambda}{1000} f_{vv}^{(0)}|_{\text{tot}}. \quad (2.13)$$

The values of $f_{hh}^{(0)}$ and $f_{vv}^{(0)}$ are components of 2×2 matrix of the forward scattering amplitude $\mathbf{f}^{(0)}$ (m m⁻³). Since K_{DP} is phase information, it has the property of being insensitive to precipitation attenuation. The correlation coefficient between horizontally and vertically polarized return signal ρ_{hv} is given as

$$\rho_{hv} = \frac{\sqrt{(S_{33}|_{\text{tot}} + S_{44}|_{\text{tot}})^2 - (S_{43}|_{\text{tot}} - S_{34}|_{\text{tot}})^2}}{\sqrt{Z_{hh}Z_{vv}}}. \quad (2.14)$$

This correlation coefficient ρ_{hv} is another commonly used polarimetry parameter along with Z_{DR} and K_{DP} shown above. For instance, ρ_{hv} decreases near the bright band and is useful to discriminate the melting layer. Although ρ_{hv} can also be simulated with I-simulator, the results for ρ_{hv} are not shown below because our cloud microphysics scheme used in this study cannot directly predict wet snow, which is responsible for the bright bands in the melting layer.

3. Improvement of the cloud microphysics scheme using space-borne radar and microwave imager

3.1. Introduction

Design and details of cloud microphysics schemes in the NWP model significantly affect the prediction accuracy of mesoscale systems, particularly the prediction of precipitation and hydrometeors. With the progress of global Earth observation satellite missions, satellite observations can now be used to verify simulated hydrometeors in numerical models (Masunaga et al. 2008; Eito and Aonashi 2009; Matsui et al. 2009; Hashino et al. 2013; Kotsuki et al. 2014; Swales et al. 2018). Based on a comparison of the cloud and precipitation properties between satellite observations and model results, studies are being conducted to improve the cloud microphysics scheme in numerical models (Li et al. 2010; Roh and Satoh 2014; Roh et al. 2017, 2020; Kuba et al. 2020).

Spaceborne precipitation radars that can observe three-dimensional (3D) reflectivity data using the Tropical Rainfall Measuring Mission/Precipitation Radar (TRMM/PR; Kummerow et al. 1998; Kozu et al. 2001) and Global Precipitation Measurement/Dual-frequency Precipitation Radar (GPM/DPR; Kojima et al. 2012; Hou et al. 2014; Skofronick-Jackson et al. 2017; Iguchi 2020) depict the 3D structure of precipitation systems. The TRMM/PR is a Ku-band precipitation radar, and the GPM/DPR consists of a Ku-band precipitation radar (KuPR) and a Ka-band precipitation radar (KaPR). The 3D reflectivity data are useful for comparing satellite observations with predicted hydrometeors. TRMM Microwave Imager (TMI) and GPM Microwave Imager (GMI), which are loaded on the same platform as the spaceborne precipitation radar, provide horizontal distribution of the precipitation information, which can be used for model validation. These microwave imagers can detect microwave signals that are scattered by cloud ice at a high-frequency band over 89 GHzV (where V is a vertically polarized wave element) and can be used for cloud ice validation. Simultaneous observations using radar and microwaves from space are beneficial in evaluating the 3D structure of precipitation systems in numerical models (Matsui et al. 2009, 2016; Chern et al. 2020).

NWP models of the JMA have been improved by focusing on the forecast accuracy of precipitation, atmospheric temperature, and water vapor (Japan Meteorological Agency 2020). However, relatively less attention has been devoted to the improvement of the prediction accuracy of hydrometeors in the atmosphere. In this study, we use GPM/DPR and GMI to evaluate hydrometeors of the NWP model of JMA and improve the cloud microphysics scheme implemented in the NWP model.

Furthermore, to save computational resources, cloud microphysics schemes in NWP models must not be complex; thus, it is difficult to implement multimoment schemes or spectral bin schemes for NWP models. The JMA's operational mesoscale model adapts a single-moment bulk microphysics scheme; a new scheme within the same framework is proposed herein. An elaborated scheme that captures realistic cloud

physics in a specific case does not necessarily reproduce better hydrometeor fields. Rather, forecasting ability eventually depends on the total balance of the details of NWP models.

In this study, the biases of hydrometeors of the original cloud microphysics scheme in the operational mesoscale model are identified using GPM observations and a new cloud microphysics scheme that reduces these biases is constructed. The structure of this chapter is as follows. Section 3.2 provides an overview of the I-simulator and cloud microphysics scheme in the mesoscale model (MSM) of JMA. Section 3.3 introduces a new scheme and shows the impacts of the new scheme by comparing it with the original scheme using the GPM/DPR and GMI observation via a case study. In section 3.4, the modification effects of the cloud microphysics scheme are clarified using a single-column kinematic mode. In section 3.5, we statistically verify the prediction accuracy of MSM by comparing the original and new cloud microphysics schemes. Section 3.6 concludes and discusses an approach for improving cloud microphysics schemes in NWP models.

3.2. Method

3.2.1. JMA meso-scale model (MSM)

The JMA operates the MSM to provide disaster prevention information. The forecast model for MSM uses the non-hydrostatic model ASUCA, as described in Chapter 2. The horizontal grid spacing is 5 km, with 817×661 grid points; the model height is approximately 21.8 km, with 76 vertical layers. The forecast area covers all of Japan and its surrounding areas. The Global Spectral Model at JMA provides the boundary condition. The MSM runs eight times a day, every 3 h. The integration time of the forecast is 39 h, with a time step of 100/3 s, but the integration time of the forecast from the initial condition at 0000 and 1200 UTC is 51 h. In the operational MSM, the cloud microphysics scheme called MP1702 was used before this study. Details about the MSM and MP1702 can be found in the JMA's NWP outline (Japan Meteorological Agency 2019).

We describe the parts of the cloud microphysics scheme relevant to this study. MP1702 is a 6-class 3-ice bulk cloud microphysics scheme (Japan Meteorological Agency 2019). The mixing ratios of water vapor (q_v), cloud water (q_c), rain (q_r), cloud ice (q_i), snow (q_s), and graupel (q_g) constitute prognostic variables. In the MP1702 scheme, a cloud distribution in the model's grid box is provided a cloud fraction of ice (C_i) and a cloud fraction of liquid (C_l). The total cloud fraction in the grid box (C) is given as

$$C = C_i + C_l - \min(C_i, C_l). \quad (3.1)$$

where the third term of the right hand side of Eq. (3.1) means a cloud fraction of mixed phase. The cloud fraction of liquid is provided by the method of Smith (1990). The shape of PDF for the cloud fraction is triangular, which is the same as in Smith (1990). The critical relative humidity for the commencement of

cloud formation is set at 95%. The cloud fraction of ice cloud is provided by the method of Wilson and Ballard (1999).

The particle size distribution (PSD) of cloud water is monodispersive. The concentration of cloud water is fixed at $1.0 \times 10^8 \text{ m}^{-3}$. The PSD of rain is provided by Abel and Boutle (2012) (hereafter referred to AB). The concentration of rain as a function of diameter D (m) is given as

$$n_r(D) = x_1 \lambda_r^{x_2} \exp(-\lambda_r D), \quad (3.2)$$

where λ_r (m^{-1}) is a slope parameter, $x_1 = 26.2 \text{ m}^{x_2-4}$, and $x_2 = 1.57$. The PSD of snow is provided by Field et al. (2007). The PSD of cloud ice and graupel is a negative exponential distribution, but the intercept parameter for cloud ice depends on temperature. The mass of ice and snow is defined by Brown and Francis (1995). The terminal velocity of hydrometeor particles is given as

$$V_{T_x} = \left(\frac{\rho_0}{\rho_a} \right)^{0.5} \sum_{k=1}^2 c_k D_x^{d_k} e^{-f_k D_x}, \quad (3.3)$$

where D_x is the diameter of category x , ρ_a is the density of air, and ρ_0 is the density of the reference air. The parameters c_{kx} , d_{kx} and f_{kx} are described in the MP1702 rows of Table 3.1. Note that particles of cloud water do not fall. The autoconversion scheme from cloud to rain is provided by the Kessler-type as

$$QCN_{cr} = K_1 H(q_c - q_{c0}), \quad (3.4)$$

where $K_1 = 0.001 \text{ s}^{-1}$ and $q_{c0} = 1.0 \times 10^{-5} \text{ kg kg}^{-1}$. At that threshold, the mean volume diameter of cloud water is about 13 micrometers. The autoconversion scheme from cloud ice to snow is given as

$$QCN_{is} = \max(K_2 H(q_i - q_{i0}), f_{AGG} q_i), \quad (3.5)$$

where Δt is the time step, $K_2 = 0.001 e^{0.025(T-273.15)} \text{ s}^{-1}$ and $q_{i0} = 1.0 \times 10^{-4} \text{ kg kg}^{-1}$. At that threshold, the mean volume diameter of cloud water is about 1.3 micrometers. The fraction f_{AGG} to split between ice and aggregates is given as

$$f_{AGG} = 1 - \exp\left(-T_0 \Delta T \frac{q_i}{q_{i0}}\right), \quad (3.6)$$

where $T_0 = 0.0384 \text{ K}^{-1}$ and ΔT is the temperature increase from the cloud top (Cotton et al. 2013). The collection rate when category x collects category y is calculated by

$$QCL_{yx} = \frac{1}{\rho_a} \frac{\pi}{4} \iint E_{xy} |V_{Tx}(D_x) - V_{Ty}(D_y)| (D_x + D_y)^2 m_y(D_y) n_x(D_x) n_y(D_y) dD_x dD_y, \quad (3.7)$$

TABLE 3.1. Parameters of terminal velocity in MP1702 and MP2003. c_2, d_2 and f_2 are ignored except for the rain particle of MP1702.

| | Rain | Cloud ice | Snow | Graupel |
|---------------|---|---|---|---|
| MP1702 | $c_1 = 4854.1$ $d_1 = 1.0$ $f_1 = 195.0$ $c_2 = -446.009$ $d_2 = 0.782127$ $f_2 = 4085.35$ (Abel and Boutle 2012) | $c_1 = 124.0$ $d_1 = 0.67862$ $f_1 = 0.0$ (Japan Meteorological Agency 2019) | $c_1 = 17.0$ $d_1 = 0.5$ $f_1 = 0.0$ (Murakami 1990) | $c_1 = 124.0$ $d_1 = 0.64$ $f_1 = 0.0$ (Murakami 1990) |
| MP2003 | $c_1 = 842.0$ $d_1 = 0.8$ $f_1 = 0.0$ (Lin et al. 1983) | $c_1 = 71.34$ $d_1 = 0.6635$ $f_1 = 0.0$ (Ferrier et al. 1995) | Same as MP1702 | Same as MP1702 |

where x and y are the category of hydrometeors, m_y is the mass of category y , and E_{xy} is the collection efficiencies. We set $E_{xy} = 1$, except for $E_{si} = 0.02 \exp(0.08T_c)$ and $E_{gi} = 0.01 \exp(T_c)$, where T_c is the air temperature of air in degrees Celsius. In the case of collecting cloud water and cloud ice, VTy is ignored for simplification.

In this study, we propose a new scheme, MP2003, which is a revised version of MP1702 and is obtained using the verification results described in sections 3.3–3.5. In the proposed scheme, we introduce the following changes. First, the PSD of rain is replaced by the Marshal–Palmer (MP) distribution (instead of the AB scheme). The PSD of rain is defined as a negative exponential form of MP, provided by Eq. (3.2) with $x_1 = 8 \times 10^6 \text{ m}^{-4}$ and $x_2 = 0$. Figure 3.1 shows the PSD of MP and AB. The concentration of AB is more than that of MP in the small-diameter regions. Figure 3.2 shows the terminal velocities of hydrometeor. The terminal velocity of rain and cloud ice is redefined as in the MP2003 rows of Table 3.1. As discussed below, the predictions using the classical simpler parameters were closer to the observed values than the predictions using the parameters from the newer references. The second change in MP2003 is in the autoconversion of cloud water to rain, where the threshold q_{c0} is changed to $1.0 \times 10^{-3} \text{ kg kg}^{-1}$ shown in Fig. 3.3. At that threshold, the mean volume diameter of cloud water is about 60–70 micrometers. Third, the fraction f_{AGG} is disabled to work in QCN_{is} (see Fig. 3.4). In the collection equation, the terminal velocity of cloud ice is not ignored and the collection efficiencies of snow and

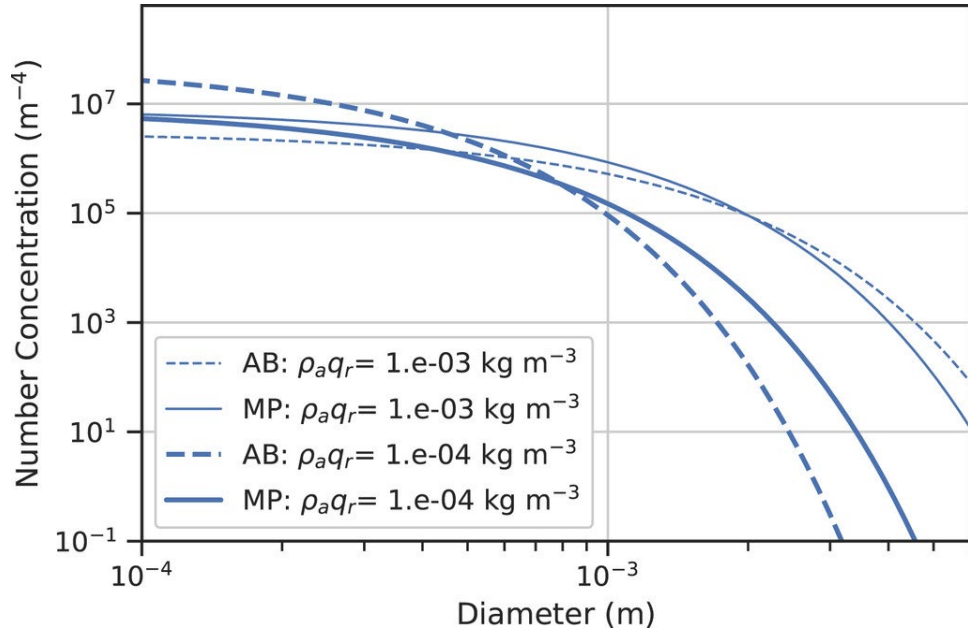


FIG. 3.1. PSD as a function of diameter. The thin lines show the concentration at $\rho_a q_r = 1.0 \times 10^{-3} \text{ kg m}^{-3}$; the thick lines show the concentration at $\rho_a q_r = 1.0 \times 10^{-4} \text{ kg m}^{-3}$. The solid (dashed) lines show the PSD of AB (MP).

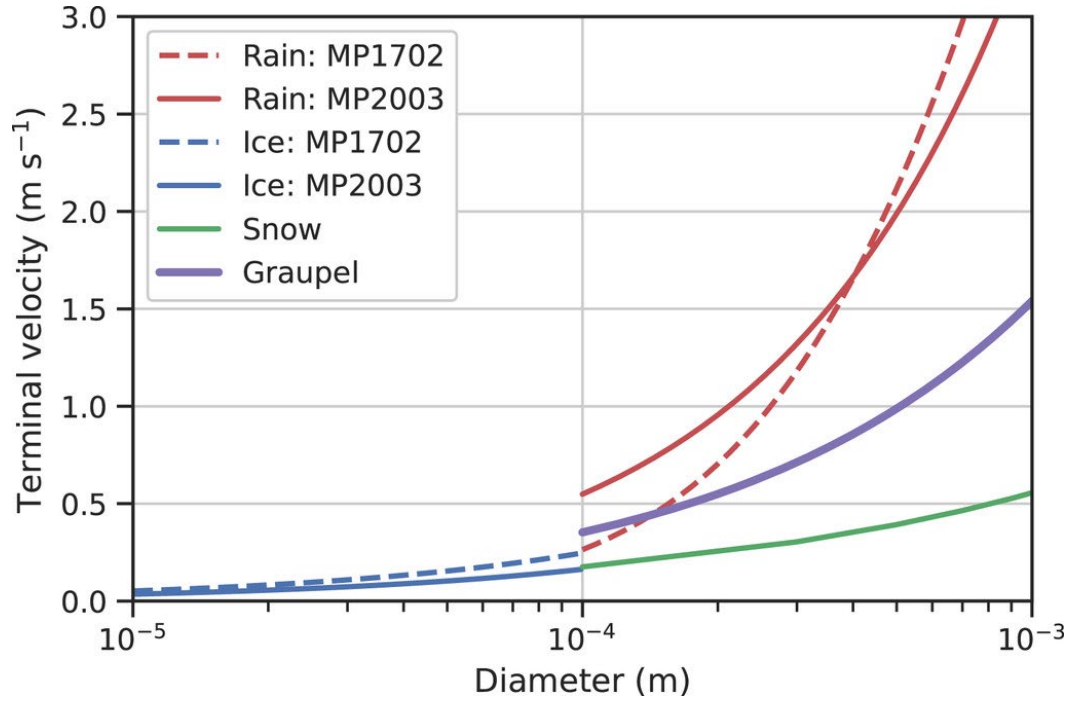


FIG. 3.2. Terminal velocities of rain, ice, snow, and graupel as a function of diameter. The solid (dashed) lines show the terminal velocities in MP2003 (MP1702) simulation.

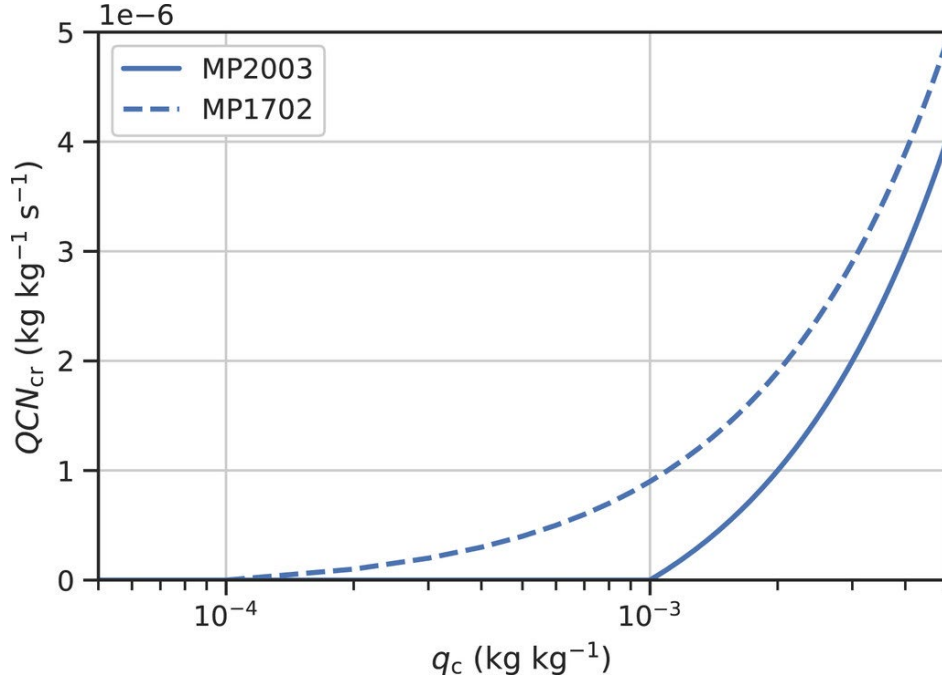


FIG. 3.3. Autoconversion tendencies from cloud water to rain as a function of q_c in MP1702 (dashed line) and MP2003 (solid line) simulation as given by Eq. (3.4).

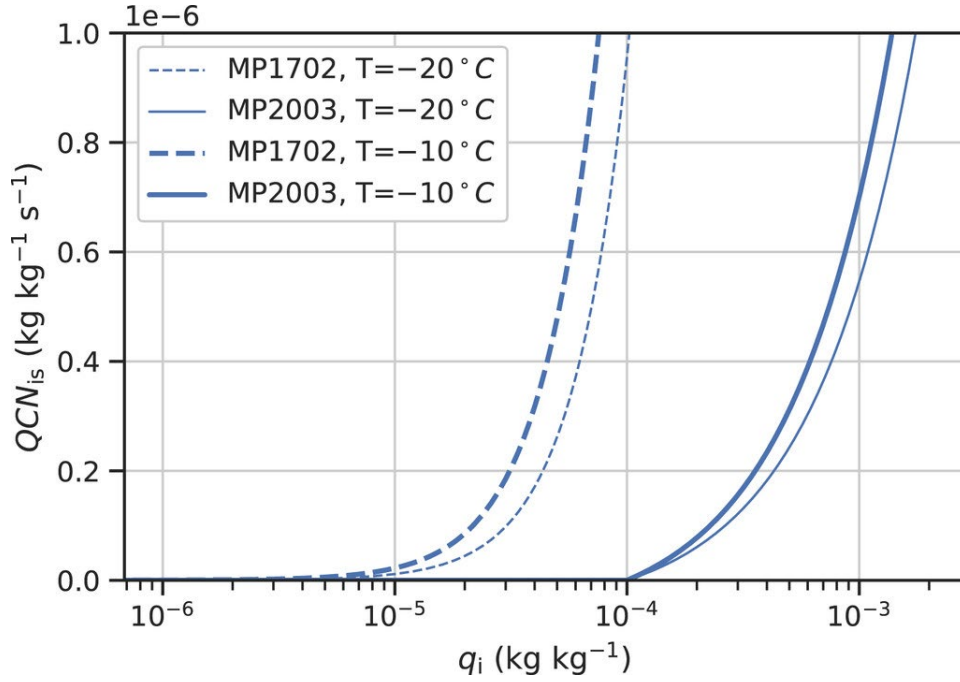


FIG. 3.4. Autoconversion tendencies from cloud ice to snow as a function of q_i in MP1702 (dashed line) and MP2003 (solid line) simulation according to Eq. (3.5), and correspond to the temperature at cloud top is -30°C and $\Delta t = 100/3$ s. The thin and thick lines show the tendencies in $T = -20^\circ\text{C}$ and $T = -10^\circ\text{C}$, respectively.

cloud ice are given as $E_{si} = 0.05 \exp(0.1T_c)$, following Ferrier et al. (1995). In section 3.3, we describe via a case study how these changes improve the biases, and in section 3.4, we show the impacts of each change separately using a single-column kinematic model.

3.3. A case study

In this section, we investigate the heavy-rainfall event that occurred on 7 July 2018. This is a remarkable case of a disaster caused by heavy rain in Japan and is named the Heavy Rain Event of July 2018 (Shimpo et al. 2019). In this heavy rainfall event, the stationary baiu front and Typhoon Prapiroon (T1807) caused heavy rainfall over a wide area of Japan from June 28 to July 8. Many areas, especially in western Japan, experienced heavy rainfall, with many rain gauges recording rainfall 2–4 times higher than the monthly climate in July. Moreover, we investigate also the event of the ocean-effect precipitation by cold surge at 0300 UTC 3 January 2018. The experimental values are compared with the values obtained using MP1702 and MP2003, as described in section 3.2.1. The experimental setting is similar to the operational model at JMA (Japan Meteorological Agency 2019).

We compare the numerical results with the observed values of GPM/GMI and GPM/DPR using the I-simulator described in section 2.2. In these cases, the GPM core satellite observed the precipitation event over Japan during 0035–0039 UTC 7 July 2018, and during 0006–0010 UTC 3 January 2018. The GMI product as reference value is T_b (K) in the L1 product, where T_b is the brightness temperature. The DPR product as reference value is *measuredZfactor* (dBZ) in the L2 product, where *measuredZfactor* means the reflectivity without attenuation correction.

Figure 3.5 shows the GMI’s T_B at 89 GHzV by comparing the observation with the MP1702 and MP2003 simulations. Figures 3.5a–c show the case of heavy-rainfall event in summer. In the observation, a low- T_B area under 220 K was widely spread over Japan (Fig. 3.5a). However, the MP1702 simulation shows that T_B is approximately 250 K all over Japan and failed to simulate the observed low- T_B area (Fig. 3.5b). In contrast, the MP2003 simulation successfully reproduced the low-temperature band of T_B , suggesting the presence of microwave-scattering ice aloft (Fig. 3.5c). In the case of winter, Fig. 3.5d shows that ocean-effect cloud systems by cold surge is observed in the south of Japan. The cloud system in MP2003 simulation is slightly closer to the observation, but not much different from the cloud system in MP1702 simulation (Figs. 3.5e,f). Figure 3.6 shows the histograms of T_B corresponding to Fig. 3.5. In the case of summer, Fig. 3.6a shows that the MP1702 simulation could not reproduce T_B lower than 240 K, whereas the MP2003 simulation was closer to the observation as it reproduced T_B as low as 200 K. In the case of winter, T_B in MP2003 simulation is slightly closer to observed T_B than T_B in MP1702 simulation over 260 K (Fig. 3.6b). However, since the difference between MP1702 and MP2003 in winter is much smaller than that in summer, we focus on the summer case in this study.

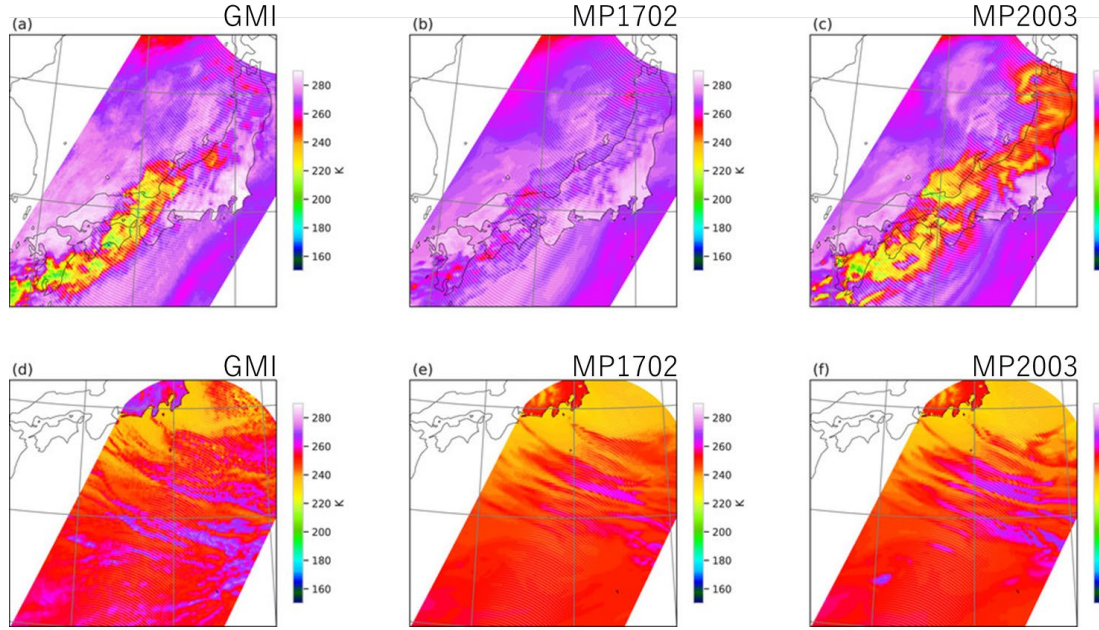


FIG. 3.5. T_B at 89 GHz V of (a),(d) GMI observation; (b),(e) MP1702 simulation; and (c),(f) MP2003 simulation. (top) T_B at 0000 UTC 7 Jul and (bottom) T_B at 0600 UTC 3 Jan 2018.

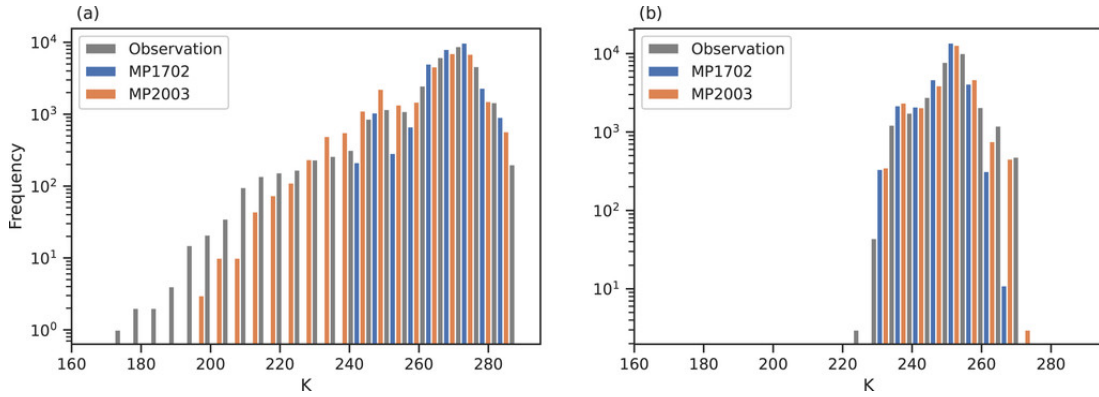


FIG. 3.6. Histograms of T_B at 89 GHz V. The gray bars show the observation; the blue bars show the MP1702 simulation; and the orange bars show the MP2003 simulation at (a) 0000 UTC 7 Jul (as in Figs. 3.5a–c), and at (b) 0600 UTC 3 Jan 2018 (as in Figs. 3.5d–f).

Figure 3.7 compares the observation and simulation values of Ku-band measured reflectivity Z_m (Ku) which is not corrected the attenuation at 2500-m altitude. The reflectivity over 40 dBZ is shown in Fig. 3.7a. The MP1702 simulation reproduced the precipitation accurately but overestimated the reflectivity in the northern area of the map around Tohoku region (Fig. 3.7b). In the MP2003 simulation, the predicted distribution of Z_m (Ku) was not significantly different from that obtained using the MP1702 simulation in the region over 30 dBZ, but the MP2003 simulation captured the observed region under 30

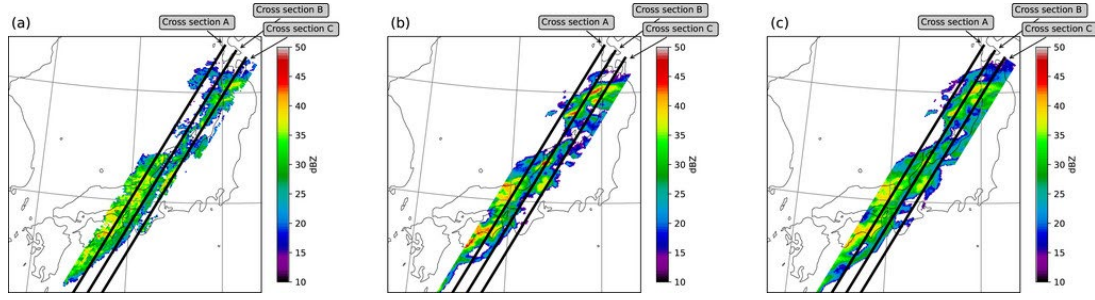


FIG. 3.7. As in Figs. 3.5a–c, but with the Ku-band reflectivity Z_m (Ku) at the altitude of 2500 m of the (a) KuPR observation, (b) MP1702 simulation, and (c) MP2003 simulation.

dBZ more accurately compared to the MP1702 simulation (Fig. 3.7c). It is noteworthy that the southern edge of the precipitation area in the MP2003 simulation is slightly larger and closer to observation than that in the MP1702 simulation.

Figure 3.8 is the vertical cross section of KuPR on the position shown by the solid black lines in Fig. 3.7. Figure 3.8a shows the Z_m (Ku) observation, which is masked below an altitude of approximately 2000 m because data at lower levels are contaminated by surface clutter (known as using the *binClutterFreeBottom*, which means the estimated clutter altitude in the DPR L2-product; Kubota et al. 2016). Figure 3.8b shows the simulated Z_m (Ku) values in the MP1702 simulation. The simulated reflectivity is smaller than the minimum detectable reflectivity of 16 dBZ in the upper atmosphere above 6000 m. In cross-section B, the reflectivity of the MP1702 simulation is stronger than the observation in the 136°–140°E region. In observations, the bright band exists around an altitude of 5000 m, which is predicted in the simulations. In the lower atmosphere, except in areas of high reflectivity (over 35 dBZ), the simulated reflectivity is weaker than the observed reflectivity. In some areas, such as around 134°E of cross-section B, the simulated reflectivity is smaller than the minimum detectable reflectivity. Figure 3.8c shows the vertical distribution of the KuPR simulation in the MP2003 simulation. The two abovementioned biases in the MP1702 simulation are improved in MP2003; the reflectivity at altitudes of both above 5000 m and under 4000 m increased and became closer to the observed reflectivity in the MP2003 simulation. Figure 3.9 shows the Contoured Frequency by Altitude Diagrams (CFADs; Yuter and Houze 1995) for KuPR on the path of DPR shown in Fig. 3.7. The CFADs median for KuPR shows that the MP1702 simulation has an excess of reflectivity over the observation around the altitude of 5000 m and the reflectivity decreases rapidly to below 25 dBZ at altitudes of around 3000–4000 m (Fig. 3.9b). The median of the CFADs in the MP2003 simulation indicates that the reflectivity remains approximately the same (27.5 dBZ) even below the altitude of 4000 m (Fig. 3.9c).

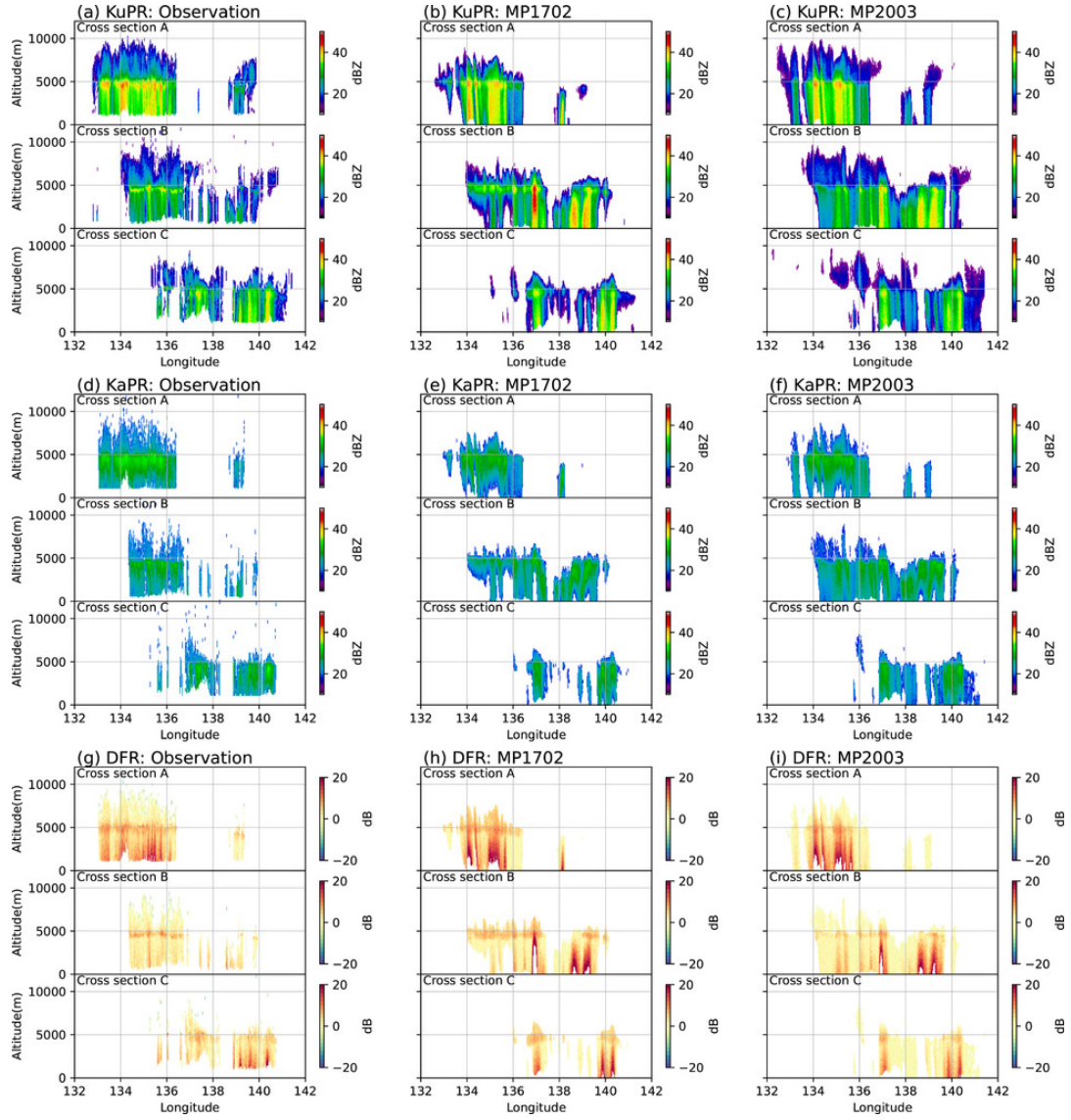


FIG. 3.8. Vertical cross section of (top) Z_m (Ku), (middle) Z_m (Ka), and (bottom) DFR_m in the position shown in Fig. 3.7. (a),(d),(g) Observed reflectivity; (b),(e),(h) simulated reflectivity in the MP1702 simulation; and (c),(f),(i) simulated reflectivity in the MP2003 simulation.

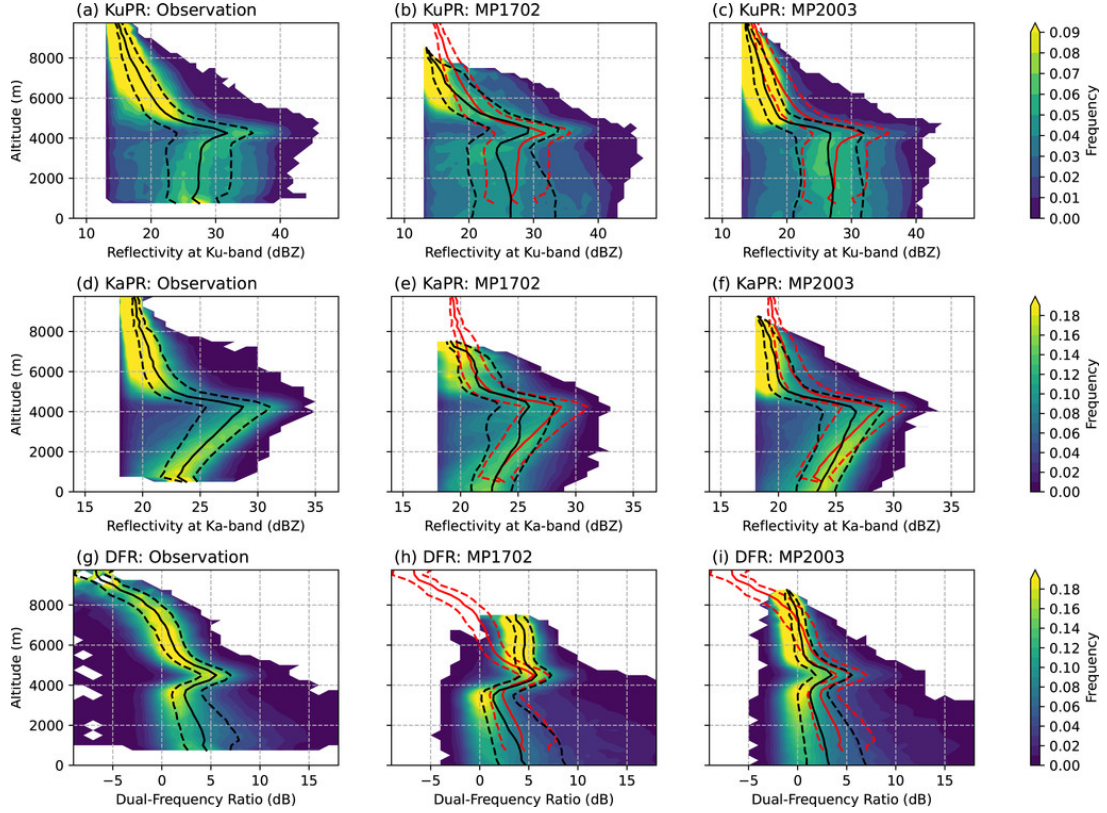


FIG. 3.9. Contoured frequency by altitude diagrams (CFADs; Yuter and Houze 1995) of (top) Z_m (Ku), (middle) Z_m (Ka), and (bottom) DFR_m in the region shown in Fig. 3.7. (a),(d),(g) Observed reflectivity; (b),(e),(h) simulated reflectivity in the MP1702 simulation; and (c),(f),(i) simulated reflectivity in MP2003 simulation. The solid line shows the median and dashed lines show the 25th and 75th percentiles. The red lines show the percentiles of observation corresponding to the element.

Figure 3.8d shows the vertical cross sections of the observed KaPR, where the clutter in low layers below the altitude of 2000 m is masked, as in KuPR. Figure 3.8e shows the simulated results of KaPR for the MP1702 simulation. In cross-section B, in particular, the reflectivity below an altitude of 5000 m at longitude 134°–137°E underestimates the simulated KaPR. This bias is reduced in the MP2003 simulation (Fig. 3.8f). In the lower atmosphere, where the reflectivity of KuPR is strong around the melting layer (134°–135°E in cross section A; Fig. 3.8a), the reflectivity of KaPR is weaker because of rainfall attenuation. Figures 3.9d–f, which is the same as Figs. 3.9a–c but for KaPR, shows the CFADs. Figure 3.9e indicates that the CFAD median in the MP1702 simulation decreased to approximately 25 dBZ at an altitude of approximately 3000–4000 m, which is not seen in the observation (Fig. 3.9d). In Fig. 3.9f, the median of the CFADs in the MP2003 simulation is closer to the observation compared to the MP1702 simulation, though still weaker than the observation. The reflectivity of the Ka-band at altitudes of 4000–6000 m is well represented compared to the Ku-band in MP2003, suggesting that there is a large error in the brightband simulation.

GPM/DPR observation is advantageous for investigating the characteristics of hydrometeors using simultaneous observations of the dual frequencies of radar signals (Ku and Ka bands). DFR_m in Eq. (2.4) is the difference ratio of Ku- and Ka-band reflectivities, and its magnitude depends on the type and size of hydrometeor particles. Figures 3.8g–i compares the observed DFR_m (Fig. 3.8g) with the simulated DFR_m for MP1702 (Fig. 3.8h) and MP2003 (Fig. 3.8i). Both the observed and simulated DFR_m are higher in the lower levels of precipitation, where Z_m (Ku) is greater than 35 dBZ because of the greater KaPR attenuation. In the layer above the bright band, the DFR_m of MP1702 simulation is higher than that of the observation and that of MP2003 is much closer to the observation. The MP1702 bright band is wider than the observed and that of MP2003 is comparable to the observed. In the CFADs of the DFR_m (Figs. 3.9g–i), MP1702 has a large bias above the altitude of 6000 m but the bias in MP2003 simulation is reduced to values comparable to the observation. Below the altitude of 4000 m, the DFR_m of both experiments is not significantly different from the observation.

Figure 3.10 compares two-dimensional joint histograms showing the frequency distribution of Z_m (Ku) and Z_m (Ka). Figure 3.10a shows the frequency distributions for the liquid phase at altitudes below 4000 m, Fig. 3.10b for the mixed phase at altitudes between 4000 and 5000 m, and Fig. 3.10c for the ice phase at altitudes above 5000 m. The solid line shows the distribution of observation, and the shades show the result of the MP1702 simulation. The dashed line in Fig. 3.10 represents the Z_m (Ka)– Z_m (Ku) relationship for graupel, obtained from the scattering calculation, and the dot–dash line represents the Z_m (Ka)– Z_m (Ku) relationship for snowflakes (Liu 2008). In the liquid phase, the observed and simulated frequency distributions are similar but the simulated frequency peak is located at a weaker portion in both Z_m (Ka) and Z_m (Ku) (around 23 dBZ for both reflectivity) than in the observation (around 26 dBZ). In the mixed and ice phases, the position of the simulation peak is significantly different between the observation and MP1702 simulation. Figures 3.10d–f show the result of the MP2003 simulation as in Figs. 3.10a–c. In the liquid phase, the frequency peak position is much closer to the observation peak (Fig. 3.10d). In the mixed phase, Z_m (Ku) is smaller than the observation and the error is still large (Fig. 3.10e). However, in the ice phase, the frequency peak is closer to the observation (Fig. 3.10f). The peaks for the observation and MP2003 simulation are close to the Z_m (Ka)– Z_m (Ku) relationship for snowflakes, indicating that snow was dominant here. In both the observation and MP2003 simulation, as the Z_m (Ka) and Z_m (Ku) become stronger, the frequency distribution shifts from the Z_m (Ka)– Z_m (Ku) relationship of snow to that of graupel. These results indicate that the difference between observation and simulation is smaller for MP2003 than for MP1702. In other words, not only the reflectivity because of rain but also because of snow and graupel for the MP2003 simulation are improved compared to the MP1702 simulation.

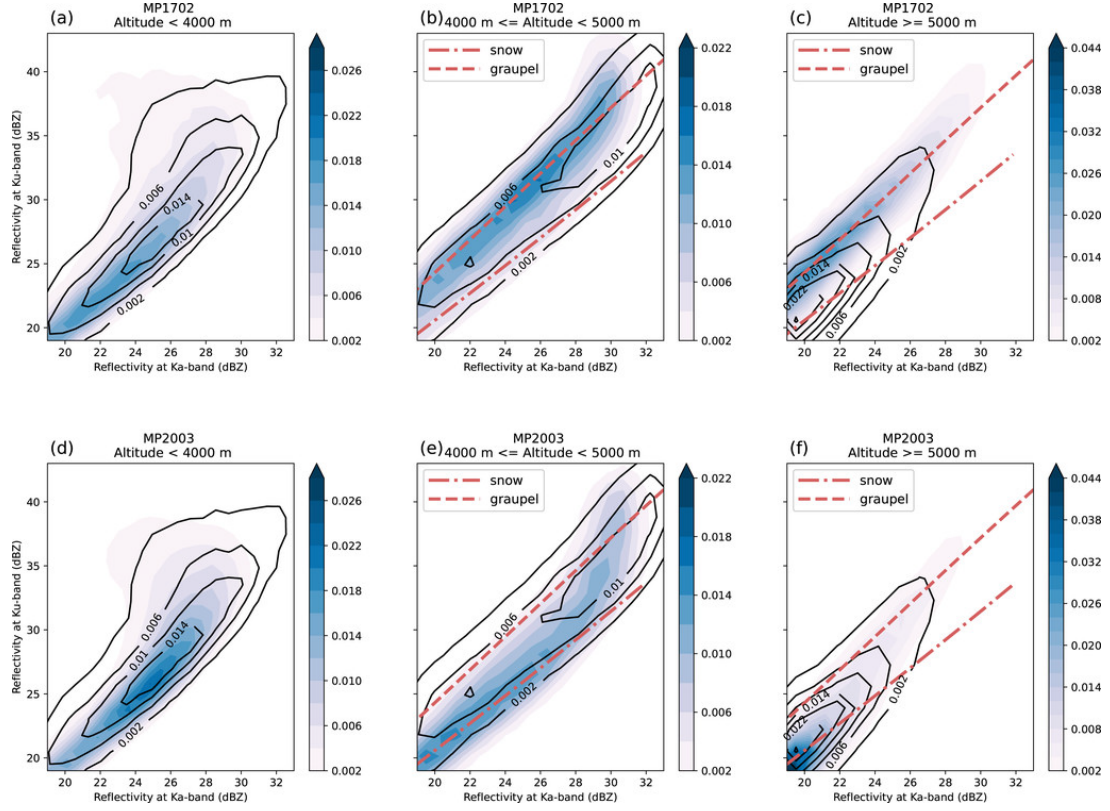


FIG. 3.10. 2D histogram of the reflectivity of the Ka- and Ku-bands. The solid lines show the DPR observation, and the shaded area is given by (top) MP1702 and (bottom) MP2003: (a),(d) altitude < 4000 m; (b),(e) $4000 \leq$ altitude < 5000 m; and (c),(f) altitude ≥ 5000 m. The dashed line is the Z_m (Ka)– Z_m (Ku) relationship of the model's graupel and the dash-dotted line is Z_m (Ka)– Z_m (Ku) relationship of the model's snowflake.

Figure 3.11 shows the vertical distributions of the mixing ratio of hydrometeors of the predicted categories, their tendencies, and the tendency of potential temperature. This vertical distribution is calculated by averaging the predicted values along the DPR path at each altitude at 0700 UTC 7 July 2018. The term $dq_x/dt|MP$ is the tendency of the mixing ratio of category x because of the cloud microphysics process, $d\theta/dt|MP$ is the tendency of potential temperature using the cloud microphysics process, and $d\theta/dt|RS$ ($d\theta/dt|RL$) is the tendency of potential temperature because of the shortwave (longwave) radiative heating. Figure 3.11 shows the result of the MP2003 simulation minus the result of the MP1702 simulation. The cloud ice mixing ratio increases, the graupel decreases at altitudes above 5000 m, and the rain increases in the lower levels in the MP2003 simulation (Fig. 3.11a). As shown in Fig. 3.11c, the water vapor decreases at altitudes of around 6000–8000 and 3000–4000 m in the MP2003 simulation, which is partly because of the increase in snow diffusion growth and decrease in rain evaporation. $d\theta/dt|MP$ of the MP2003 simulation, calculated from the diabatic heating of latent heat release of the cloud physical processes, is larger than that of the

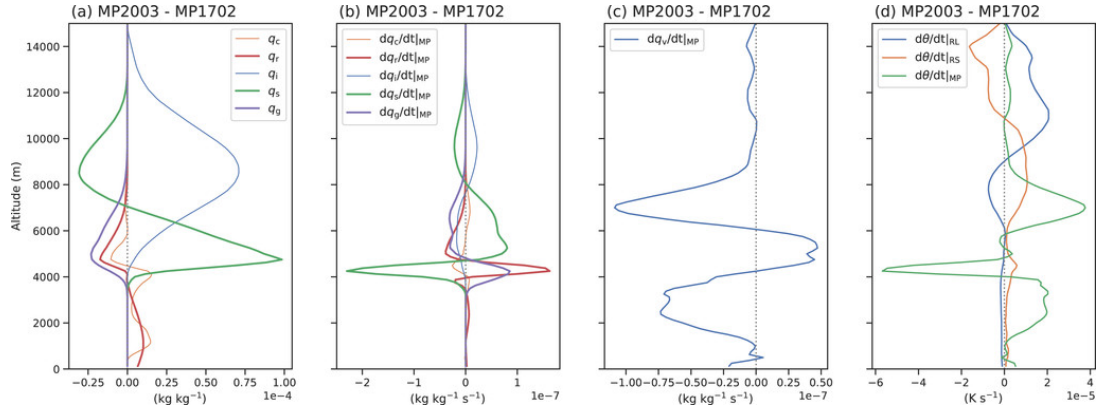


FIG. 3.11. Vertical distribution of average hydrometeors. (a) Mixing ratios of hydrometeors and (b)–(d) 1-h averaged tendencies of the MP2003 simulation minus the MP1702 simulation. Differences in tendencies for (b) hydrometeors and (c) water vapor from cloud microphysics and (d) potential temperature from shortwave radiation (RS), longwave radiation (RL), and cloud microphysics (MP).

MP1702 simulation at altitudes below 4000 m because of the decrease in rain evaporation and lower than that at the MP1702 simulation in the 4000–5000-m layer because of the increase in the amount of melting snow (Figs. 3.11b,d). The increase in ice clouds increases radiative heating in the upper troposphere in the 10 000–11 000-m layer, increasing the potential temperature tendency (Fig. 3.11d).

3.4. A kinematic model analysis

The MP1702 simulation in the previous section yielded the following four scientific findings:

- The scattering signal of microwave T_B at 89 GHz is weaker than the observation. This frequency band is sensitive to cloud ice. This suggests that cloud ice is in small amounts and that there is a lack of prediction of anvil clouds, which are mainly caused by deep convection.
- The reflectivity is weaker than observation aloft the melting layer. This indicates less backscatter from solid precipitation, which has larger particle sizes than cloud ice. It suggests that predicted snow and graupel are less.
- In the mixed or ice phases above the melting layer at 4000–5000 m, the DFR_m is larger than the observation. This indicates that the predominant particle type per unit volume is different from reality, suggesting more graupel than snow predicted.
- In the liquid phase at altitudes lower than 4000 m, the reflectivity is weaker than the observation. This is more pronounced during stratiform precipitation, indicating a rapid decrease in raindrops melted from solid precipitation.

TABLE 3.2. Experiment setting

| Experiment | Details |
|------------------|--|
| MP1702 | Operation setting in MSM until March 2020 (Japan Meteorological Agency 2019). |
| MP1702F | As MP1702, but for $f_{AGG} = 0$. |
| MP1702FVA | As MP1702F, but for terminal velocity of cloud ice, QCL_{is} , E_{is} and q_{c0} are modified (see section 3.2). |
| MP2003 | As MP1702FVA, but for PSD of rain used MP. Operation setting in MSM from March 2020. |

In this section, we clarify the causes of these findings and the impact of the change to MP2003 on the vertical profile of the atmosphere. We use a single-column kinematic model, Kinematic Driver Model (KiD; Shipway and Hill 2012), to investigate the effect of the changes in the cloud microphysics scheme. We adopt the deep convection and warm rain cases implemented in KiD. See Shipway and Hill (2012) for details of the design of these test cases. Table 3.2 summarizes the parameter settings of the cloud microphysics process for the experiments performed in this section.

3.4.1. Positive bias of brightness temperature

The low scattering of ice clouds in microwave radiation in the MP1702 simulation causes the bias in T_B at 89-GHzV band. The low scattering of ice clouds is because of the small amount of mass concentration of ice clouds. One reason for the small mass concentration of ice clouds is the fast conversion efficiency of ice clouds to snow because f_{AGG} is dominant in QCN_{is} , as shown in Fig. 3.4. Another reason is that the terminal velocity of cloud ice in the MP1702 simulation is set closer to graupel than ice crystals, as shown in previous studies (Ferrier et al. 1995; Mitchell 1996) (see Table 3.1 and Fig. 3.2).

Figure 3.12 shows the time evolutions of vertical profiles for each hydrometeor category for the case of the deep clouds simulated by KiD. In the MP1702 simulation (Fig. 3.12a), almost all ice clouds are converted to snow as soon as ice nucleation occurs and the remaining ice falls at a high rate; thus, there is almost no ice in the upper layer. In the MP1702F simulation (Fig. 3.12b), the conversion from ice to snow is suppressed by setting $f_{AGG} = 0$ (Table 3.2). The result shows that the ice clouds remain in the upper layer. In the MP1702FVA simulation (Fig. 3.12c), the terminal velocity of ice, collection of ice to snow, and autoconversion of cloud to rain were modified in addition to the changes in MP1702F simulation (Table 3.2), allowing ice clouds to stay in the upper layers. In the MP2003 simulation (Fig. 3.12d), the PSD of rain was modified in addition to the changes in MP1702FVA simulation. Consequently, there is

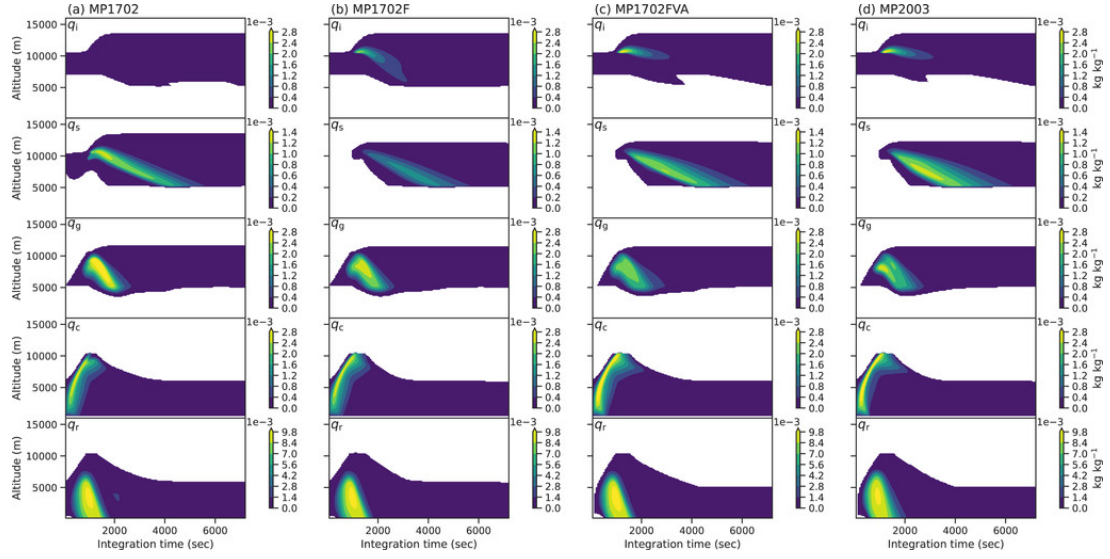


FIG. 3.12. Vertical profiles of hydrometeors predicted by KiD: (from top to bottom) cloud ice, snow, graupel, cloud water, and rain at an integration time. Time evolutions of mixing ratio obtained from the (a) MP1702, (b) MP1702F, (c) MP1702FVA, and (d) MP2003 simulations.

greater increase in cloud ice and snow in the upper layers. The results indicate that the improvement in T_B in the MP2003 simulation is because of the modification of f_{AGG} and terminal velocity.

3.4.2. Overestimated reflectivity above melting layer

The overestimation of DFR_m in MP1702 above the melting layer is because of the overprediction of graupel particles. Figure 3.13 shows the time-averaged vertical distribution of the mixing ratio of hydrometeors, production terms of snow, and graupel in the single-column kinematic model during the integration time of 0–7200 s. Note that the melting process is not shown. The production terms shown in Fig. 3.13 are defined as follows: $QCN_{x(y)z}$ is the autoconversion process from category x (and category y) to category z , QCL_{xy} is the collection process of x by y , QCL_{xyz} is the production rate of category z because of the collection process of x by y , QVD_{xv} is the evaporation from x , QDP_{xy} is the deposition from x to y , QSB_{xv} is the sublimation from x , and QFZ_{xy} is the freezing process from x to y . MP1702 and MP2003 simulation experiments are compared in Fig. 3.13.

First, in MP2003, cloud ice is maintained and grows in the upper layers because of the slower terminal velocity of cloud ice and the elimination of f_{AGG} , and its conversion to snow is suppressed in Eq. (3.5). Regarding the production term, collection unrelated to cloud ice and diffusional growth leading to snow growth are also suppressed. However, the time averages of QCL_{is} and QCN_{is} increased because of cloud ice in the upper layers. The vertical distribution of graupel in the layer between 8000 and 12 000 m shows that QCN_{csg} and $QCL_{srg} + QCL_{rsg}$ decreased with the decrease in snow as a source in MP2003. Graupel

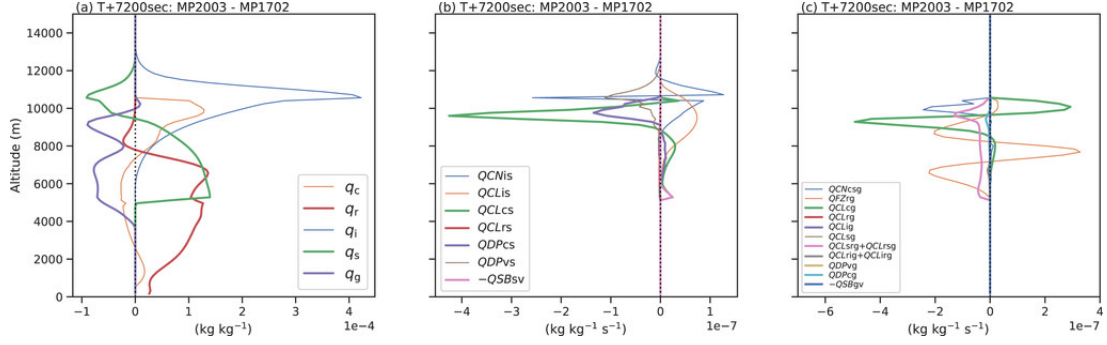


FIG. 3.13. Time-averaged vertical profiles of mixing ratio and tendency during $(T + 0)$ and $(T + 7200)$ s by KiD. This case is the test case of deep convection. The solid lines show (a) the mixing ratio profiles of the MP2003 simulation minus the MP1702 simulation and (b),(c) the tendencies of the MP2003 simulation minus the MP1702 simulation.

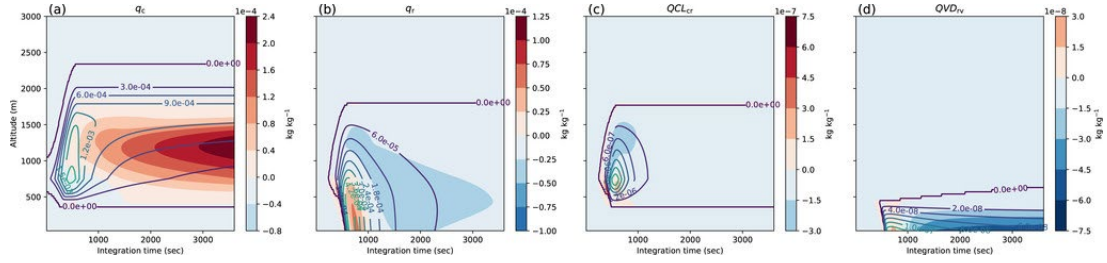


FIG. 3.14. Warm rain case of KiD. The contour shows (a) q_c , (b) q_r , (c) QCL_{cr} , and (d) QVD_{rv} at an integration time in the MP1702FVA simulation. The shading shows the MP2003 simulation minus the MP1702FVA simulation.

production is also delayed, decreasing QCL_{cg} . Incidentally, the increase in QCL_{cg} around 12 000 m compensates for the decrease in QCN_{csg} .

Next, for rain and graupel, QFZ_{rg} is reduced and graupel is suppressed. Since QFZ_{rg} depends on the slope parameter using the formulation of Bigg (1953), the difference in the freezing amount from rain to graupel is because of the difference in PSD of rain. Phenomenologically, using the MP PSD implies that the freezing of small rain particles is suppressed more than that when using the AB PSD. Consequently, below 10 000 m, graupel decreases, QCL_{csg} and $QCL_{rsg} + QCL_{srg}$ are further suppressed, and snow increases in MP2003. From the above, MP2003 has less predicted graupel amounts and more predicted snow amounts than MP1702. Therefore, the change in the predicted amount of graupel and snow improved the Z_m (Ka) – Z_m (Ku) relationship.

3.4.3. Underestimated reflectivity at lower layer

In MP1702, even outside the strong precipitation area, the reflectivity is smaller in the lower layers of the predicted weak precipitation area because of the small amount of predicted q_r . Specifically, when q_r is small, the reflectivity of MP1702 is smaller because the AB scheme has much more small particles than

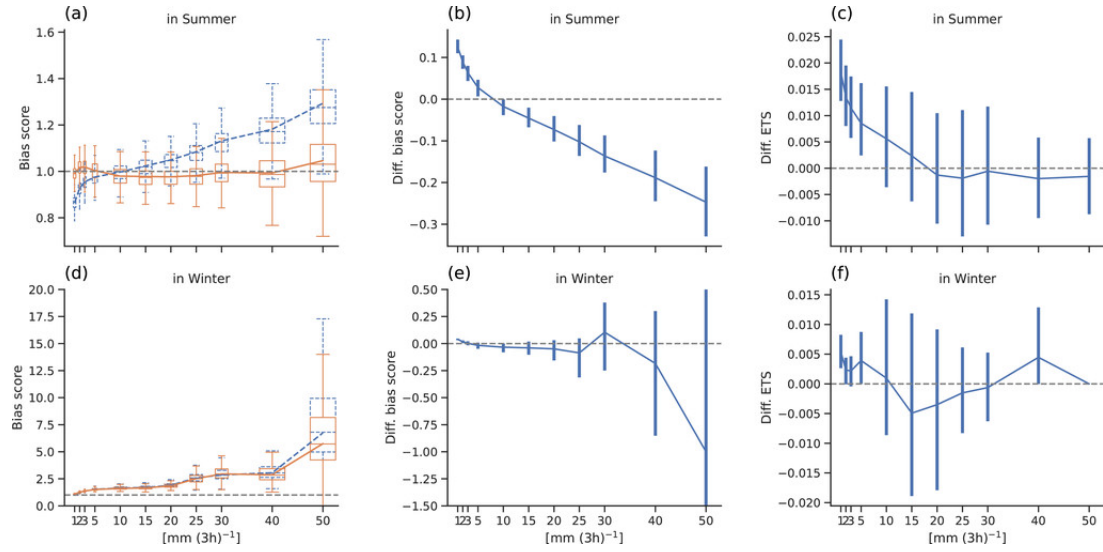


FIG. 3.15. Scores of precipitation forecast at each 3-h accumulated precipitation. (a),(d) Bias score of the MP1702 simulation (blue) and MP2003 simulation (orange). (b),(e) Bias score of the MP2003 simulation minus the MP1702 simulation. (c),(f) ETS of the MP2003 simulation minus the MP1702 simulation. (top) Scores in the summer experiment and (bottom) scores in the winter experiment. (a),(d) The box-and-whisker plots show the 0th, 25th, 50th, 75th, and 100th percentiles. (b),(c),(e),(f) The error bars show a 95% confidence interval calculated using the bootstrap method.

the classical negative exponential distribution (MP scheme). Figure 3.14 shows the results of the single-column kinematic model in the case of warm rain simulated by KiD. The experiments compared are MP1702FVA and MP2003, showing the difference between the AB and MP schemes. When q_r is small, the magnitude of the production term for collection and evaporation in MP2003 is smaller than that in MP1702FVA (Figs. 3.14b–d). Consequently, the precipitation peak at 800 s of integration time is increased, and the evaporation after 1000 s is suppressed (Fig. 3.14d). This change in the simulated rain particles improved the reflectivity in the lower layers.

3.5. Impacts on the numerical weather forecasts

An assimilation-forecast cycle experiment was performed to verify the impact on forecasts using the JMA mesoscale NWP system by changing the cloud microphysics scheme. The NWP model setup is the same as in the case study. The forecasting range covered by the statistical verification is 39 h. The initial time of forecast is created every 3 h. The NWP model runs eight times per day. The experimental period was selected for the summer experiment from 18 June to 23 July 2018, and the winter experiment from 23 December 2017 to 27 January 2018. In the experiment, the cloud microphysics scheme of the forecast model used in the data assimilation system was changed from MP1702 to MP2003. The data assimilation method in the mesoscale NWP system is the four-dimensional variational method with strong constraints on the forecast model. If the data assimilation system is not updated simultaneously, there is a high risk of

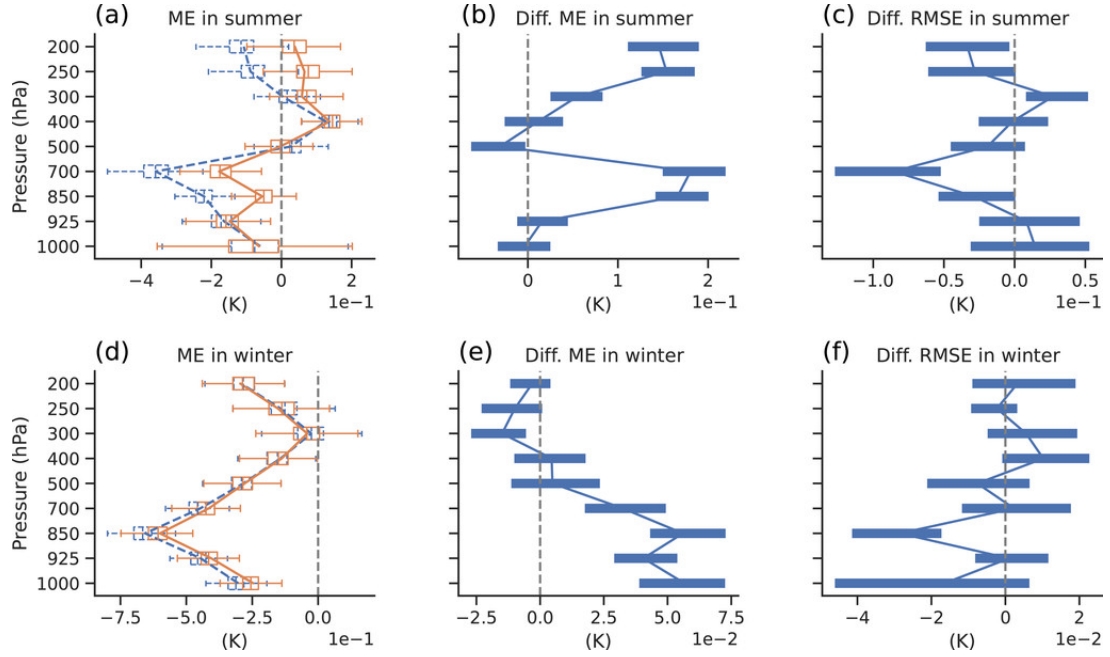


FIG. 3.16. Verification of temperature forecast in the upper air against sonde data. (a),(d) Mean error (ME) of the MP1702 simulation (blue) and MP2003 simulation (orange). (b),(e) ME of the MP2003 simulation minus the MP1702 simulation. (c),(f) Root-mean-square error (RMSE) of the MP2003 simulation minus the MP1702 simulation. (top) Scores in the summer experiment and (bottom) scores in the winter experiment. (a),(d) The box-and-whisker plots show the 0th, 25th, 50th, 75th, and 100th percentiles. (b),(c),(e),(f) The error bars show a 95% confidence interval calculated using the bootstrap method.

missing the error drift of the forecast model. Therefore, it is critical to maintain consistency between the internal models of the assimilation system and the forecast model.

First, the precipitation verification results are presented. The precipitation verification is based on the 3-h integrated precipitation averaged over 20 km of the verification grid to compare observations and forecast with same resolution. The reference value is the Radar/Rain-gauge-Analyzed Precipitation (R/A: Nagata 2011) of JMA. The R/A is the two-dimensional precipitation product observed by ground-based radar and corrected by rain gauge observations in Japan. The bias score and equitable threat score (ETS) were obtained for the forecast time from 3 to 39 h. The bias score greater than 1.0 indicates overprediction, and the bias score less than 1.0 indicates underprediction. The ETS for perfect forecast indicates 1.0. Figure 3.15a shows the bias score for the MP1702 simulation (blue) and MP2003 simulation (orange), and Fig. 3.15b shows the change in the bias score (the MP2003 simulation minus the MP1702 simulation) in summer. The precipitation forecasts with a threshold of less than 10 mm (3 h)^{-1} increased from the MP1702 simulation to the MP2003 simulation, whereas the precipitation forecasts with a threshold of more than 10 mm (3 h)^{-1} decreased. Summer bias scores improved significantly in the wide range of precipitation intensity of more than 10 mm (3 h)^{-1} . Figure 3.15c shows the difference in ETS between the MP1702 and MP2003 simulations, where positive values mean improvement for the MP2003 simulation.

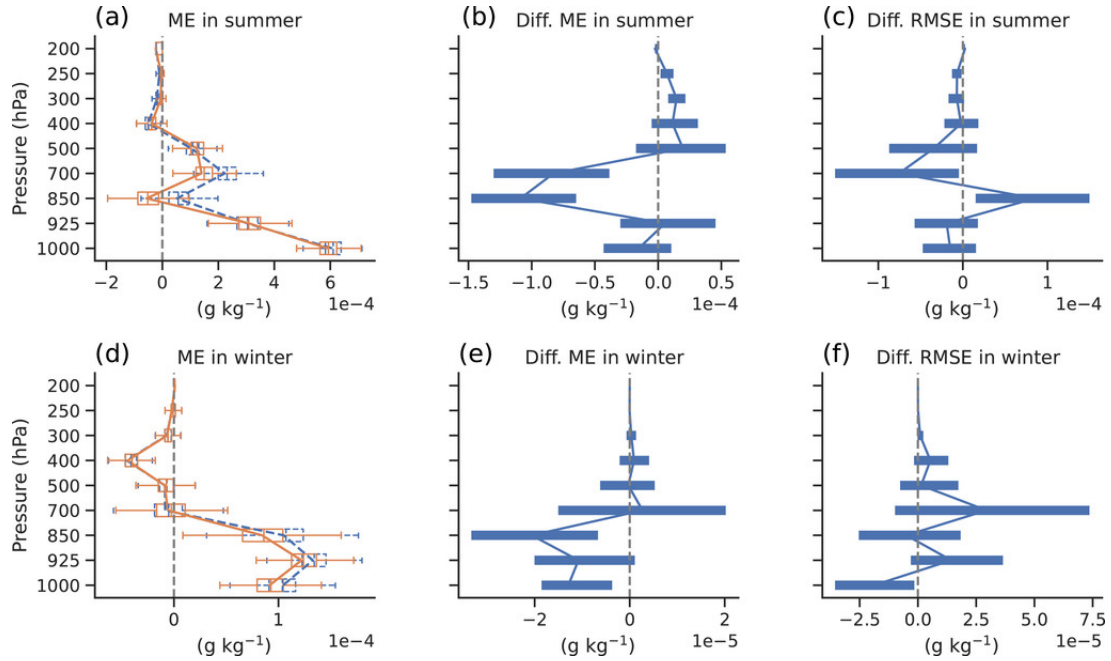


FIG. 3.17. As in Fig. 3.16, but for the specific humidity.

The ETS shows a significant improvement in precipitation predictions below 10 mm (3 h)^{-1} . The bottom panels of Fig. 3.15 show the winter scores. The winter bias scores are overforecasted (Fig. 3.15d), but the ETS of the threshold below 10 mm (3 h)^{-1} (Fig. 3.15f) shows a similar improvement as in the summer experiment.

Next, we compare the model with the sonde observations in Japan. Figure 3.16 shows the validation results of the 24-h forecast. Figure 3.16 shows the temperature validation results, where the negative biases at 200–250 hPa and 700–850 hPa are eliminated in summer, and the root-mean-square error (RMSE) for the MP2003 simulation is also significantly improved. In winter, the bias in the MP2003 simulation is significantly reduced below 700 hPa, and the RMSE in the MP2003 simulation at 700 hPa is significantly improved. Figure 3.17 shows the results of the specific humidity verification, where MP2003 was drier than MP1702 at 700–850 hPa, and the RMSE was significantly improved at 700 hPa, but significantly degraded at 850 hPa. The water vapor in the model was originally negatively biased, but the MP1702 simulation might have compensated for this by over evaporating rain. The cooling caused by excess evaporation also caused a low-temperature bias in the lower level. Eliminating negative biases, such as lower layer low-temperature bias and frequency of light rainfall, supports the correctness of the change to the MP2003 simulation. Both Figs. 3.16 and 3.17 indicate that the experiments with MP2003 are overall superior to those with MP1702 regarding temperature and water vapor fields. The improvement of the cloud microphysics scheme has a positive effect on the overall skill of the NWP.

3.6. Conclusions

In this study, we verified the cloud microphysics scheme of the JMA regional model using GPM core-satellite observations. Results showed that there was a very large error in cloud fields in the original scheme. The low T_B of GMI was not reproduced because of the lack of significant amount of cloud ice. The reflectivity of Ku and Ka radar was underestimated in both the lower and upper layers because of low rainfall and small particles in the lower layers and a smaller amount of snow in the upper layer for solid precipitation. From the comparison of the Z_m (Ka) – Z_m (Ku) relationship, the amount of graupel was found to be large.

Based on the evaluations from the GPM satellite observation, we used the single-column kinematic model to identify the cause of the error of the original cloud microphysics scheme (MP1702). Through sensitivity experiments using the single-column kinematic model, we made the following three changes and constructed a new cloud microphysics scheme (MP2003). First, the elimination of f_{AGG} changed the conversion rate from cloud ice to snow. The physical rationale for this change from the definition of ice and snow categories. Cloud particles with an average volume particle size greater than the diameter of 1.3 microns are immediately converted to snow by the conventional method. Since the minimum particle size for the snow category is a diameter of 200 microns, the conventional method results in an excessive amount of conversion. Second, the terminal velocity of cloud ice was modified. This change is to adjust the falling velocity of cloud ice to the observed value. The conventional fall velocity is close to that of large particles such as graupel, which is excessive for cloud ice particles smaller than the diameter of 100 microns. Third, the size distribution of rain particles was modified from the AB scheme to the MP scheme. The physical aim of this change in PSD is to reduce the amount of evaporation caused by small raindrops.

The NWP forecast experiments were conducted by comparing the NWP model with MP1702 and MP2003. The precipitation forecast validation showed significant improvement for weak precipitation. In the sonde validation, the biases of specific humidity improved in the lower layers, and the RMSE of specific humidity is improved at 700 hPa in the summer experiment and worsened at 850 hPa in the summer experiment. Atmospheric temperature prediction also successfully eliminated the low-temperature bias in the upper and lower layers.

We investigated the improvement of a single-moment bulk cloud microphysics scheme (MP1702, MP2003). This type of cloud microphysics scheme is simple; however, other complicated and sophisticated schemes are used in research models, such as multimoment schemes or spectral bin schemes. Although this study is within the scope of comparable results for the two simple schemes, the results indicate that prediction accuracy is improved by enhancing the total balance of processes in microphysics scheme. Finally, we conclude that combining each process is more important for the overall performance of the cloud microphysics scheme and that introducing a partially advanced scheme does not improve the

prediction. It is also speculated that schemes might also depend on the areas, such as the polar or tropical region or the midlatitude zone, indicating that a scheme developed at one region will not necessarily work well in other regions.

We also found that compensating errors affect the overall performance of the cloud microphysics scheme. The model has biases because of initial conditions, boundary conditions, and approximations in various physical processes. In the new scheme, MP2003, the water content distribution improved upon changing the bias at 850 hPa to a negative bias, but the difference from the observation became larger. However, the prediction accuracy for other altitudes and temperatures improved. The original scheme, MP1702, could compensate for the water vapor bias in the model at the expense of the prediction accuracy of hydrometeors distribution in the atmosphere. If the model has a compensating error, it will be challenging to upgrade even if the model is improved correctly because the unfairly compensated score will be partially degraded.

In this study, the model was upgraded based on GPM observations and verified in detail for precipitation. This upgrade was introduced into the JMA's operational mesoscale NWP system on 26 March 2020 (Ikuta et al. 2020). We improved the cloud microphysics scheme, assuming that a model with better reproducibility of hydrometeor fields provides better forecasting ability. However, many more observations of clouds will be available in the future as new satellites are launched. Moreover, the accuracy of individual precipitation events needs to be improved. These issues will be clarified in the future using the results of other satellite data, including the EarthCARE satellite mission (Illingworth et al. 2015) or ground-based radar network (e.g., ULTIMATE; Roh and Satoh 2021; Satoh 2021).

Finally, I will summarize the new findings obtained in this chapter. Conventional validation using single-frequency radar reflectivity has had difficulty in estimating the type of particles contained in a unit volume of the atmosphere. However, the validation using multiple-frequency radar reflectivity in this study was found to reveal the certainty of the prediction of the amount of snow and graupel in the unit volume of the atmosphere. The validation also revealed that overestimated evaporation below the melting layer depends on the definition of the particle size distribution in the cloud microphysical scheme. The scheme that solved the issues identified by the validation was found to improve the accuracy of the prediction of atmospheric temperature and water vapor. This means that the accuracy of the prediction of the vertical distribution of the hydrometeors has a significant impact on the accuracy of the atmospheric prediction. Let us consider the effect of the elementary processes that brought about this vertical distribution of hydrometeors. It is common to think that slowing down the conversion of cloud ice to snow will reduce snow. However, the slower the conversion from cloud ice to snow results in a delay in the growth of snow. When this happens, snow grows slower and falls more slowly, making it more likely to remain in

the upper air. From the above, counterintuitively, snow will increase. This is due to the complexity of cloud microphysical processes, which involve many elementary processes. This study shows that model-based analysis of elementary processes is useful for improving our understanding of cloud microphysical processes. Although the changes made in this study were simple, they resulted in improvements. In other words, this suggests that prediction accuracy can be improved by improving the total balance of microphysical scheme processing to match observations without using a complicated scheme.

4. Improvement of cloud microphysics scheme using polarimetric radar and disdrometer

第4章については、5年以内に雑誌等で刊行予定のため、非公開。

5. Evaluation of turbulence scheme using the ground-based radar observation

5.1. Introduction

In a NWP model, the surface scheme provides a link between the atmosphere and the lower boundary conditions, the latter of which are a source of heat and water vapor and absorb momentum. The planetary boundary layer (PBL) scheme controls vertical mixing within the BL and is responsible for the transport of heat, water vapor, and momentum. The amounts that are transported are related to the TC intensity and are thus key to the prediction of TC-related disasters. The optimal choice or continuous improvement of the PBL scheme is therefore necessary for research discoveries that could prevent or mitigate such disasters.

In this study, we examine the sensitivity to BL schemes in NWP model simulations at a horizontal grid spacing of 250 m which resolution is characteristic of the gray zone. This resolution is much higher than that used operationally, but it is commonly used for investigating the mesoscale systems related to severe storms. Furthermore, such a resolution needs to be tested for future use in operational models. Thus, a comparison between the simulation results and the observations is necessary to validate possible candidates for the PBL scheme in the gray zone.

To evaluate the PBL schemes, we chose the case of Typhoon Faxai, which made landfall near a metropolitan area in Japan (Chiba City, Chiba Prefecture) on 8 September 2019. At landfall, Faxai kept its quasi-symmetric structure, and the details of its TCBL structure were captured by ground-based Doppler radar. Miyamoto et al. (2022) simulated the realistic track and intensity of Faxai around landfall using a numerical model with a horizontal grid spacing of 1 km and suggested that the strong intensity was caused mainly by the presence of supergradient wind. We chose a model with a horizontal grid spacing of 250 m and compared the ability of the LES and PBL schemes to simulate the TCBL and the secondary circulation. To evaluate the numerical results, we used the model to simulate radar-observed parameters and compared the results with the observations. In particular, Doppler velocities are compared with the results of the simulations to quantitatively reveal the numerical model representation of the BL structure. Mashiko (2020) investigated streak structures caused by horizontal rolls in Faxai using a NWP model with a horizontal grid spacing of 250 m and argued that their presence causes the strong winds observed at the land surface.

The configuration of the NWP model, the observation simulator, and the observation data that we used as a reference are described in Section 5.2. Section 5.3 first outlines the characteristics of Faxai and then presents the results of the sensitivity test of the PBL scheme. Based on our experimental results, we simulated radar observations and then compared the results with observations. Section 5.3 also examines the

characteristics of the secondary circulation of the TC and discusses the effects of the rolls on the BL. Section 5.4 summarizes this study and provides an outlook on the development of NWP in the future.

5.2. Model and simulation

5.2.1. Non-hydrostatic model ASUCA

In this study, the non-hydrostatic model ASUCA from the JMA is used to conduct numerical simulations of Typhoon Faxai with a horizontal grid spacing of 250 m. ASUCA forms the basis of the MSM, which is the core of the JMA's regional NWP system. Figure 5.1 shows the domain of the MSM, which covers Japan and its surroundings using a horizontal grid spacing of 5 km. For the operational simulations, we used the Kain and Fritsch (Kain 2004) scheme for the convection scheme, the one-moment cloud microphysics scheme (Ikuta et al. 2021a), and the MYNN3 (Nakanishi and Niino 2009) scheme for the PBL scheme. The surface flux scheme was implemented according to Beljaars and Holtslag (1991). Land use information for the model's grid was taken from numerical map information with a resolution of 50 m provided by the Geospatial Information Authority of Japan. The initial conditions of the MSM were provided by the Meso-scale Analysis, which is the four-dimensional variational method version of the ASUCA-Var.

In the present study, we adopted a special set of parameters and conditions in ASUCA for conducting sensitivity tests of the gray-zone simulations. We compared the sensitivity to three PBL schemes for simulating the PBL structure: RANS, LES, and gray-zone schemes. We used the MYNN3 scheme for the RANS scheme; the Deardorff (DDF; Deardorff 1980) scheme as an LES scheme; and the Anisotropic Deardorff Model (ADM; Kitamura 2016) scheme as a gray-zone scheme. The ADM scheme is based on the DDF scheme and takes into account the anisotropy of eddy viscosity and thermal vortex diffusivity. The MYNN3 and DDF are selected for their contribution to the JMA since they have been used both in the operational system and in research. The ADM is selected because it is an extension of the DDF.

Table 5.1 shows the experimental configuration of the ASUCA. The experiments were run in three domains: D1, D2, and D3 (Fig. 5.1). In the D1 experiment, the horizontal grid spacing was 2 km, the number of horizontal grids was 733×605 , the number of vertical layers was 76, and the top of model was at an altitude of 22108 m. The height of the cell edge at the lowest level in the spatial discretization for the finite volume method employed by ASUCA was 20.0 m. The height at other typical levels are shown in Table 5.1. The physical scheme was the same as in the MSM, but convective parameterization was switched off in the sensitivity experiments. The initial and lateral boundary conditions were provided by Meso-scale Analysis and the MSM, respectively. The settings of the D2 experiment were the same as in the D1 experiment, with the following exceptions: the horizontal grid spacing was 250 m, the number of horizontal grids was 2001×2001 , and both the initial and lateral boundary conditions were provided by

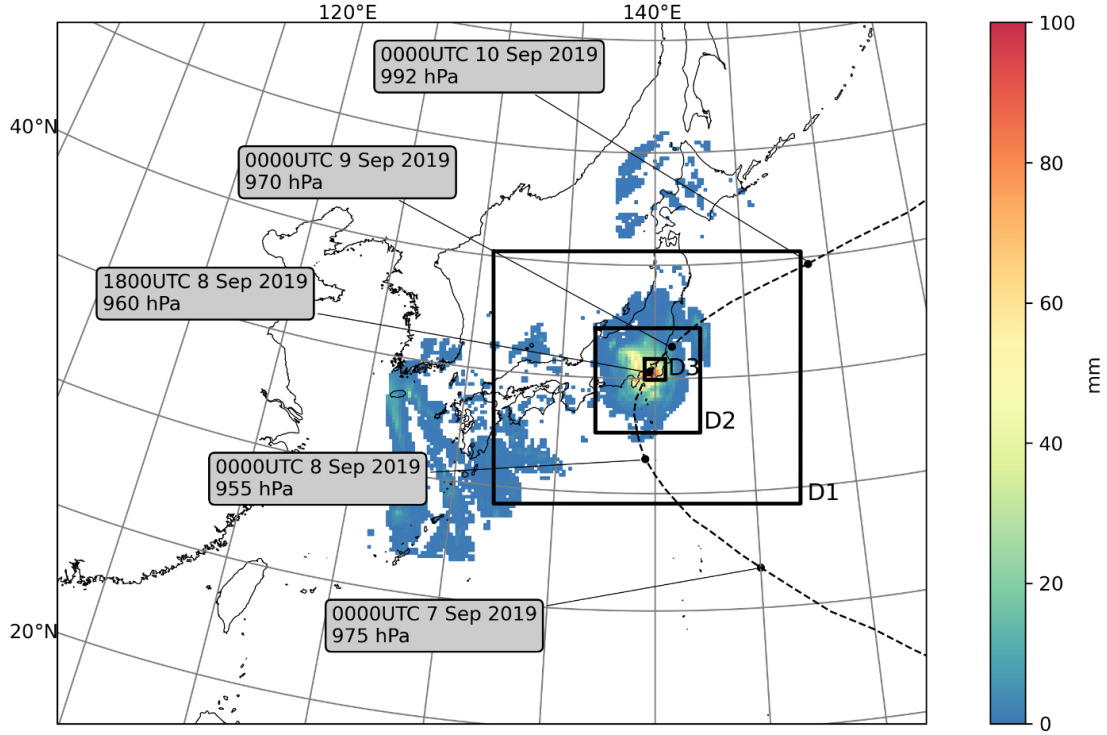


FIG. 5.1. The domain of the MSM. Dashed line shows the best track of Faxai. Solid rectangles denote the domains covered in the sensitivity experiments in this study. Shading indicates the 3-hourly accumulated precipitation by Radar/Raingauge-Analysed Precipitation.

the forecast result in D1 experiment. In the D2 experiment, we tested three types of PBL schemes: the MYNN3, ADM, and DDF schemes. The settings of the D3 experiment were the same as in the D2 experiment using the DDF scheme, but the horizontal grid spacing was 50 m, and both the initial and lateral boundary conditions were provided by the forecast result in the D2 experiment using the DDF scheme. The D1, D2, and D3 experiments were performed using the one-way nesting method with Rayleigh damping sponge layers. The sea surface temperature as the bottom boundary condition was given by the High-Resolution Merged Satellite and In-situ Data Sea Surface Temperature (HIMSST; https://ds.data.jma.go.jp/gmd/goos/data/pub/JMA-product/him_sst_pac_D/Readme_him_sst_pac_D) from JMA, and it was not a prognostic value in the NWP model.

D2 is the target region with which we investigated the sensitivity of TC forecast to the PBL schemes using a horizontal grid spacing of 250 m. D3 was used in the reference simulation with a horizontal grid spacing of 50 m. In the following discussion, for convenience, we refer to the experiments using the MYNN3 scheme in D2, the ADM scheme in D2, the DDF scheme in D2, and the DDF scheme in D3 as MYN250, ADM250, DDF250, and DDF050, respectively.

TABLE 5.1. Configuration of the sensitivity experiments.

| | Configuration | | |
|---|--|----------------------|------------------------------|
| | D1 | D2 | D3 |
| Initial time | 1500 UTC 8 September 2019 | | |
| Horizontal grid spacing | 2,000 m | 250 m | 50 m |
| Number of horizontal grids | 733 × 605 | 2,001 × 2,001 | 2,001 × 2,001 |
| Number of vertical layers | 76 | | |
| Top of model | 22,108 m | | |
| Altitudes of vertical layers | The heights of the cell edges at vertical layers of 1, 10, 20, 30, 50, 60, 70, and 76 are 20.0, 416.99, 1382.23, 3000.0, 8610.21, 12811.20, 18081.83, and 22108.0 m, respectively. | | |
| Initial/boundary condition | Meso-scale Analysis (Ikuta et al. 2021b) / MSM (Japan Meteorological Agency 2019) at 1500 UTC 8 September 2019. | D1 | D2 with DDF (Deardorff 1980) |
| Lateral sponge layer of Rayleigh damping | 36,000 m | 16,000 m | 3,200 m |
| Cloud microphysics | Six-class three-ice single-moment bulk scheme (Ikuta et al. 2021a) | | |
| Sea surface temperature | HIMSST (https://ds.data.jma.go.jp/gmd/goos/data/pub/JMA-product/him_sst_pac_D/Readme_him_sst_pac_D) at 1800 UTC 7 September 2019. | | |
| Surface flux scheme | Beljaars and Holtslag (1991) | | |
| Turbulence parameterization | MYNN3 (Nakanishi and Niino 2009) | | |
| | | ADM (Kitamura 2016) | |
| | | DDF (Deardorff 1980) | |

5.2.2. Integrated satellite simulators (I-Simulator)

The predictive performance of the numerical simulations can be validated by various remote sensing observations from both space and the ground using observation simulators. Satellite simulators have been used to evaluate the results of numerical simulations that refer to satellite observations (Masunaga et al. 2008; Eito and Aonashi 2009; Matsui et al. 2009,2020; Hashino et al. 2013; Roh and Satoh, 2014; Ikuta et al. 2021a). A similar approach is used for ground-based radar observations. As shown by Matsui et al. (2020), radar observations have high spatial and temporal resolution and are indispensable for the verification of high-resolution models.

To simulate ground-based radar observations, we used the Integrated Satellite Simulators (I-Simulator; Ikuta et al. 2021a). The I-Simulator aims to validate physical processes and to assimilate satellite and radar observations in the NWP model; it is currently used for validations and assimilations of JMA models. In this study, the I-Simulator was enhanced to simulate ground-based radar observations using the scattering database for polarimetric radar parameters. The scattering database is calculated by the POLARimetric Radar Retrieval and Instrument Simulator (POLARRIS; Matsui et al. 2019); thus, we regard the I-Simulator as an integrated observation simulator comprising space and ground-based radar observations. POLARRIS quickly provides a high-quality simulation of polarimetric parameters, as the appropriate algorithms and scattering databases can be efficiently prepared offline. The I-Simulator computes the reflectivity and Doppler velocity along the radar beam path using the Mueller matrix (Vivekanandan et al. 1991) database from POLARRIS. For the Mueller matrix computation, the radar frequency was set to 5,335 MHz to match the radar observations being compared to the simulation. The effective particles were cloud water, rain, cloud ice, snow, and graupel. The PSD (PSD) of cloud water was the mono-dispersion distribution. The PSDs of rain, cloud ice, and graupel were exponential distributions with negative exponents, and the intercept parameter of cloud ice was given by a function of temperature. The PSD of snow was given by a mixture of the negative exponential and the gamma distribution based on the Field scheme (Field 2007). In addition, the particle shapes and orientations were taken into account by using the definition of Matsui et al. (2019). Particles of cloud water and cloud ice were assumed to be spherical, while those of rain, snow, and graupel were assumed to be spheroid. The orientation of all particles was given by a quasi-Gaussian distribution.

5.3. Observations of Faxai

The best track of Typhoon Faxai in 2019 is shown in Fig. 5.1. As the precursor of Faxai, a tropical cyclone formed over the southern sea of Wake Island at 0000 UTC 2 September 2019, moved west-northwestward and then became Typhoon Faxai over the southeastern sea of Minamitori Island at 1800 UTC 4 September, before changing its course to the northwest. Faxai kept its northwestward track and developed rapidly, reaching its maximum intensity over the sea to the south of Hachijo Island ($\sim 140^{\circ}\text{E}$ and 30°N) at 1800 UTC 7 September, before turning north-northwest. Faxai then turned to the north-northeast and passed near the Miura Peninsula before 1800 UTC 8 September. At around 2000 UTC 8

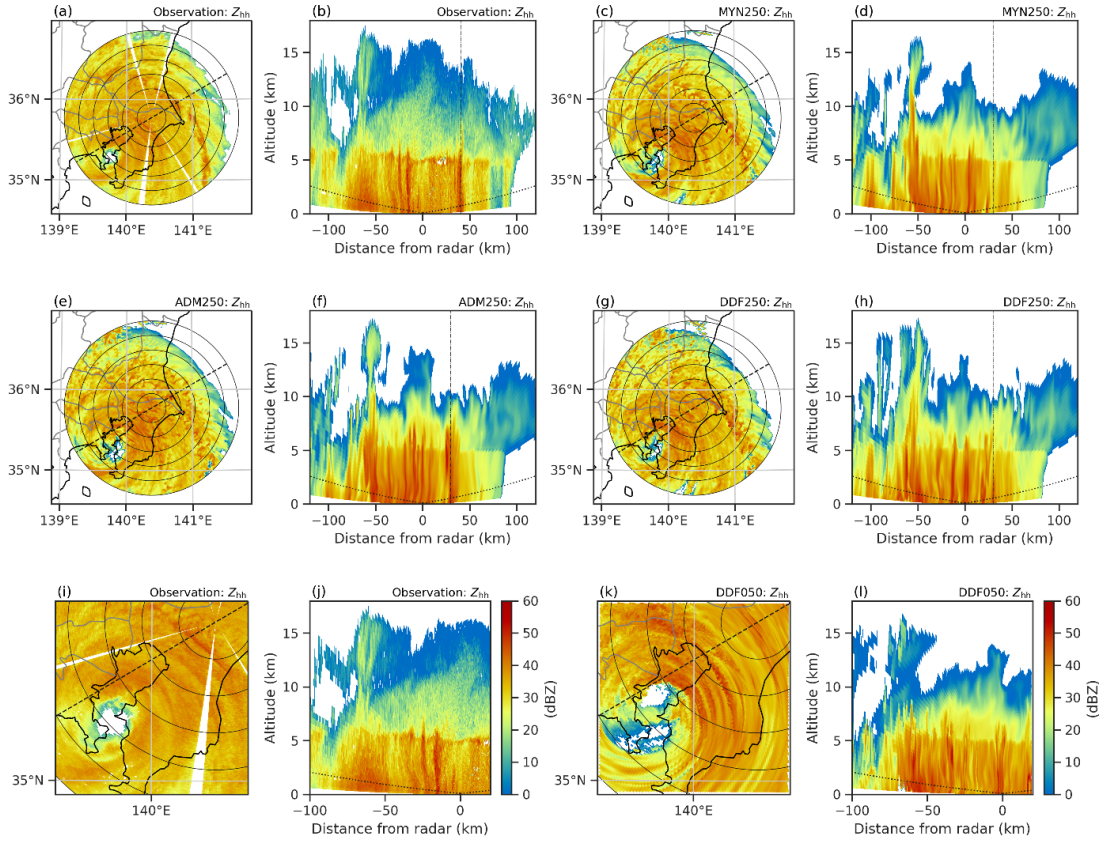


FIG. 5.2. Radar reflectivity at Narita Airport. (a), (c), (e), (g), (i), (k) PPI scan at an elevation angle of 0.7° at 1759 UTC and (b), (d), (f), (h), (j), (l) RHI scan at 1800 UTC 8 September 2019. (a), (b) Observation; (c), (d) MYN250; (e), (f) ADM250; (g), (h) DDF250; (i), (j) observation in D3; and (k), (l) DDF050. Circles indicate distance from the radar site in 20 km increments. The dashed lines in PPI scans indicate the position of the RHI scan. In the RHI scans, the dotted lines indicate the altitude at an elevation angle of 0.7° .

September, it made landfall near Chiba City, Chiba Prefecture (Fig. 5.6a). It moved to east-northeast of Japan, transformed into an extratropical cyclone at 0000 UTC 10 September, and then accelerated its east-northeastward movement before eventually disappearing south of the Aleutians at around 1800 UTC 11 September. Figure 5.1 also shows the 3-hour accumulated precipitation as determined by R/A, which is the estimated precipitation from ground-based radar and rain gauge observations at 1800 UTC 11 September. The precipitation area of Faxai is within D2, whose size is $500 \times 500 \text{ km}^2$. Because Faxai passed over a metropolitan area, nearby ground-based radar sites were able to capture its detailed structure. In addition, Faxai approached Japan while keeping its nearly axisymmetric structure, so it represents a good example for understanding a typical TC structure.

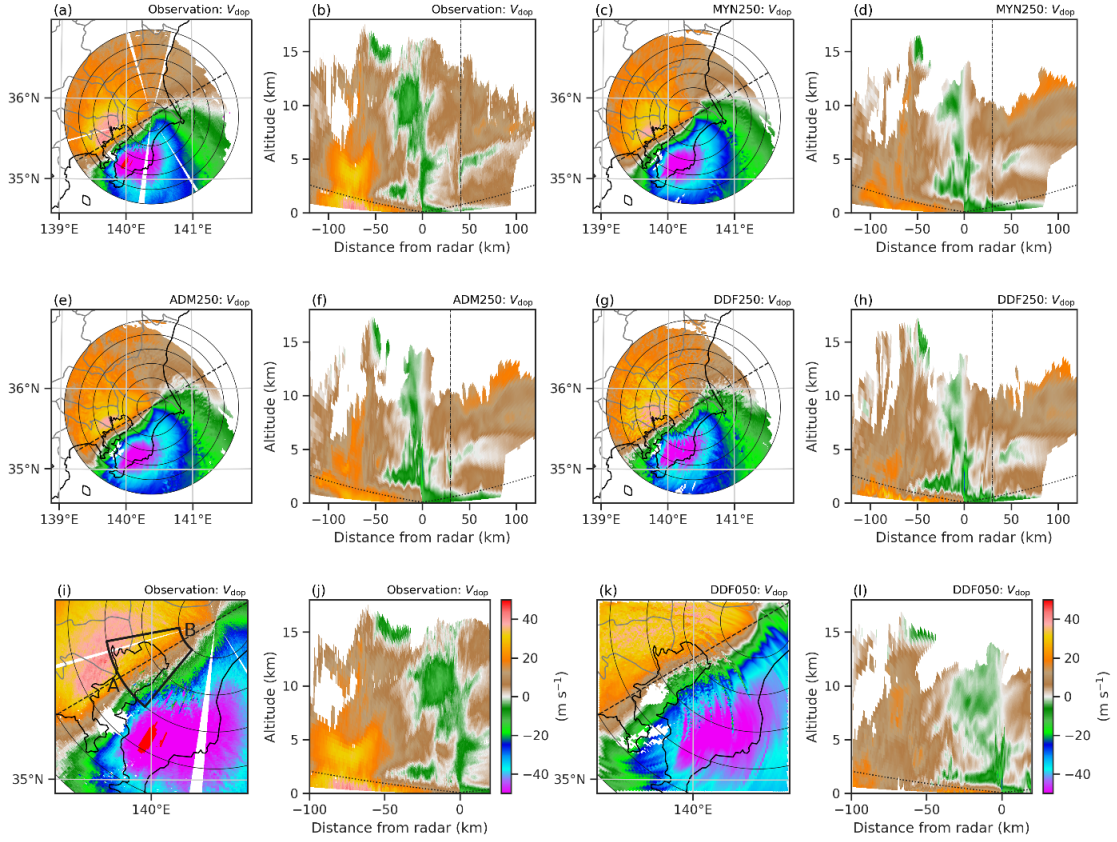


FIG. 5.3. As in Fig. 5.2, but for Doppler velocity. (i) The thick line shows the region covered in Fig. 5.12.

In this study, we use dual-polarimetric radar data recorded at Narita Airport. The transmission radio frequency of the radar is 5,335 MHz. Solid-state power amplifiers are used as a transmitter. The observation range at the site is 120 km. The resolution of radial direction is 150 m and that of the azimuth is 360/512 degrees in Plan Position Indicator (PPI) mode. In Range Height Indicator (RHI) mode, the resolution of the elevation angle varies between 0.0° and 1.0° . The volume scan is scheduled by PPI scans (0.7° , 90.0° , 17.0° , 12.5° , 0.7° , 9.2° , 6.9° , 5.1° , 0.7° , 3.8° , 2.8° , 2.1° , 0.7° , 1.5° , 1.1° , and 0.7°) and the RHI scan (0° – 180°) in 5-minute intervals. The RHI scan provides high-density data in the vertical direction. In particular, the observed high-density Doppler velocity in the vertical direction indicates the structure of the BL.

Figure 5.2a,b shows the PPI and RHI scans of the observed radar reflectivity by the C-band dual-polarimetric Doppler radar located at Narita Airport. The observation times of the PPI and RHI scans were 1759 and 1800 UTC 8 September 2019, respectively. The eye of Faxai was observed at

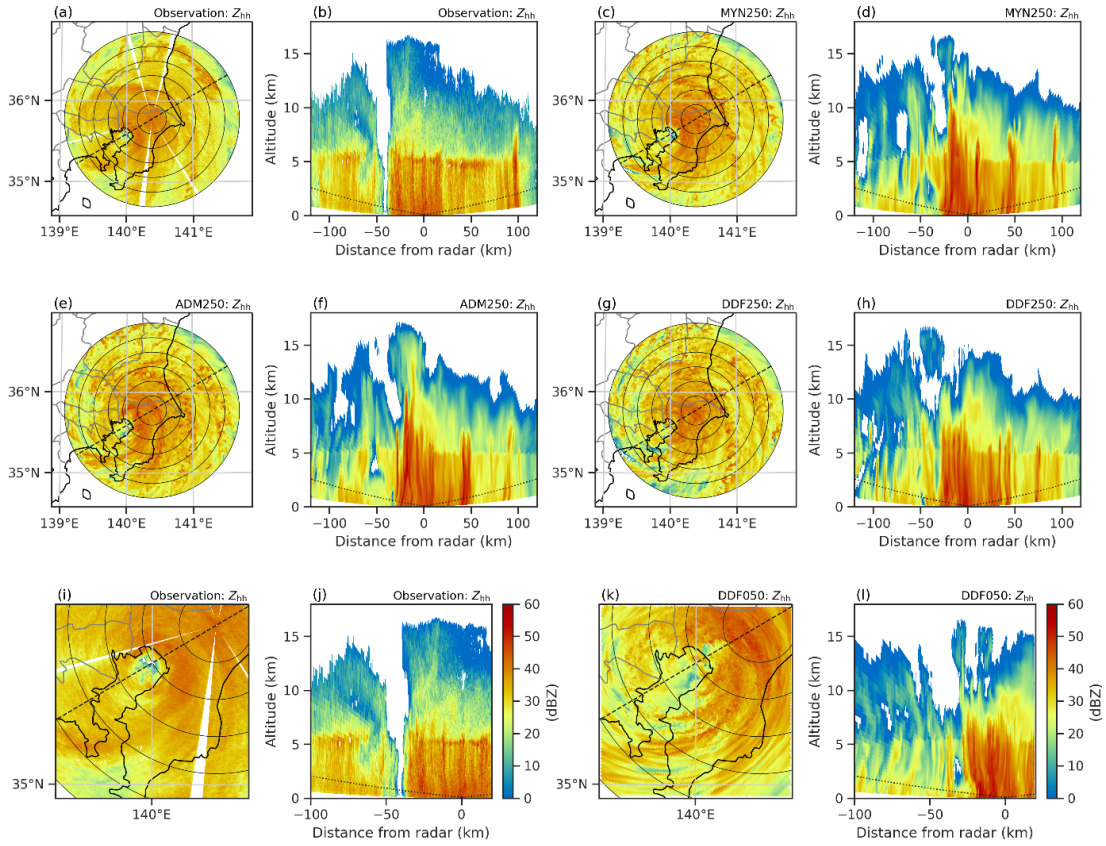


FIG. 5.4. As in Fig. 5.2, but at PPI scan at 1919 UTC and RHI scan at 1920 UTC 8 September 2019.

139.7°E and 35.3°N, and a strong reflectivity corresponding to precipitation from the northern rainband was observed at a radius of 100 km from the eye (Fig. 5.2a). The reflectivity of the PPI and RHI scans show that the eyewall was located around -70 km from the radar site (Figs. 5.2a,b). Strong reflectivity due to precipitation was observed at altitudes below the melting layer (5–6 km); strong precipitation due to another rainband located to the east of the TC center was observed around $+40$ km from the radar site. Figure 5.3a shows the Doppler velocity of the PPI scan observation. The eyewall is on the southwest side of the radar site, resulting in a positive Doppler velocity on the northwest side and a negative Doppler velocity on the southeast side of the TC center. Figure 5.3b shows the Doppler velocity of the RHI scan observation. The negative (positive) Doppler velocity is observed at altitudes below 1 km in a positive (negative) distance. At almost all locations of 0 m s^{-1} values, the wind direction is oriented perpendicular to the RHI cross-section. Above altitudes of 2–5 km at a distance of $+50$ km, positive Doppler velocity is dominant. As shown by the dashed-dotted line in Fig. 5.3b, there is a columnar of positive Doppler velocity at a distance of $+40$ km up to an altitude of 9 km. This is due to convection in the rainband around a distance of 120 km from the

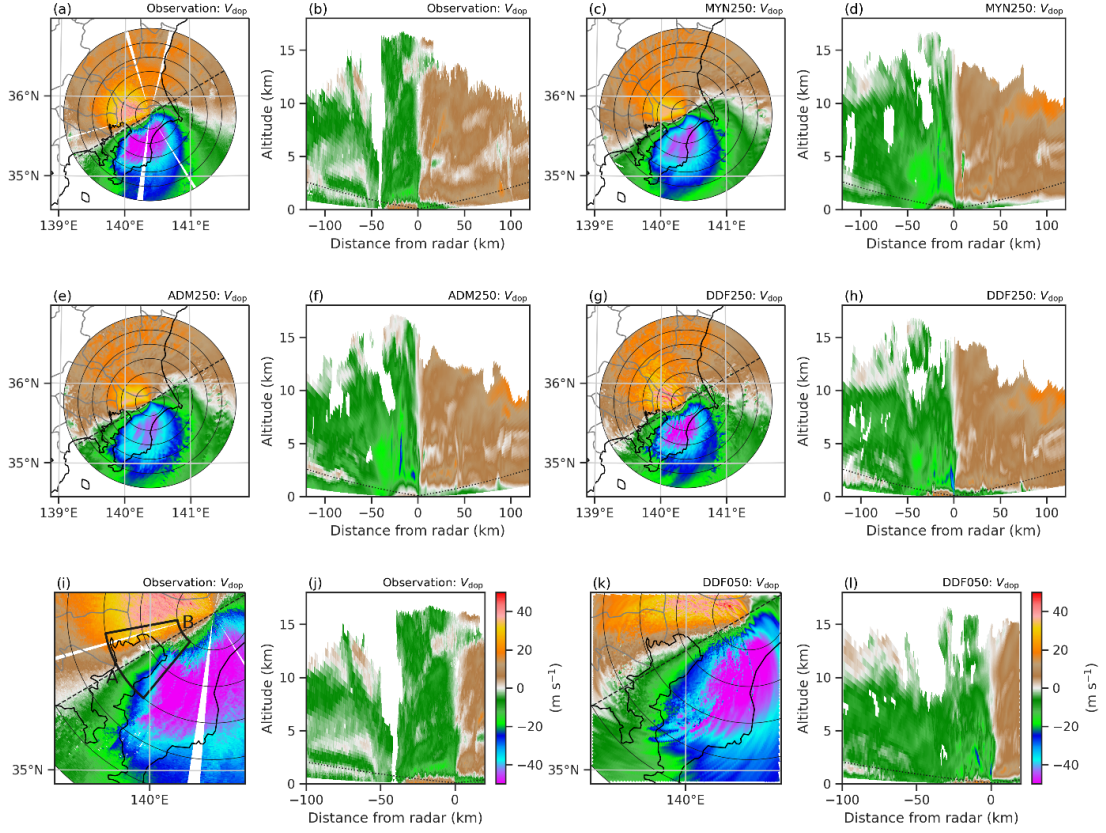


FIG. 5.5. As in Fig. 5.4, but for Doppler velocity.

center of the TC, as shown in the PPI and RHI image of the reflectivity (Figs. 5.2a,b). At 1920 UTC, the RHI scan crossed Faxai's eye (Figs. 5.4a-b, 5.5a-b), which was located around 40 km from the radar site (Figs. 5.4a,b). Therefore, in Fig. 5.5b, positive (negative) Doppler velocity in the distance of -40 – 0 km and negative (positive) Doppler velocity greater than the distance of 0 km means inflow (outflow). The inflow (outflow) is observed below (above) an altitude of about 1 km (Fig. 5.5b). Note that the Py-ART was used to visualize the radar observations and simulations.

5.4. Numerical results

5.4.1. Track and central pressure

First, we examine the simulated track and intensity of Faxai and compare them with observations. In MYN250, ADM250, DDF250, and DDF050, the trajectory of the center of Faxai follows a cycloid curve as the TC center moves northeastward, but the precise locations of the center are not the same as those of the best track (Fig. 5.6a). Here, we define the center position of Faxai as the location where the sea level pressure is at a minimum after smoothing with a 5×5 grid-averaging filter. The

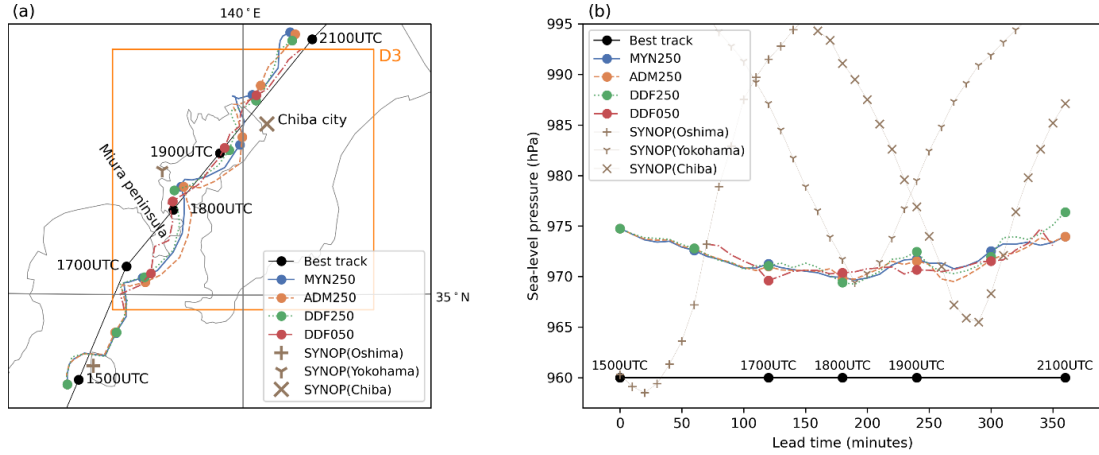


FIG. 5.6. (a) TC tracks in MYN250 (blue), ADM250 (orange), DDF250 (green), and DDF050 (red), and best track (black). Circles indicate the TC's central position each hour from 1500 UTC to 2100 UTC 8 September 2019. D3 is shown by the orange rectangle. (b) Central pressure of TCs at each lead time in experiments and from SYNOP observations recorded at Oshima (cross), Yokohama (Y), and Chiba (X). SYNOP locations are shown in the left panel.

amplitude and period of oscillation of the cycloid curve are smaller in DDF050 than in the other experiments. The simulated central pressures are almost similar in the experiments regardless of the PBL schemes and the resolution, but are about 10–15 hPa greater than the best track between 1500 and 2100 UTC (Fig. 5.6b). In SYNOP's (report of surface observation from a fixed land station; WMO 2019) observations, the lowest pressures were recorded at the Oshima site at 1519 UTC (958.4 hPa), at the Yokohama site at 1812 UTC (969.1 hPa), and at the Chiba site at 1949 UTC (965.1 hPa). The SYNOP records also indicate that the central pressure of the simulated Faxai was larger than the observation. Although it is clear that the central pressure of the simulated TC does not match the central pressure recorded in the best track, the simulation error with respect to SYNOP is smaller than that with respect to the best track around 1800 UTC.

5.4.2. Simulations of radar

Figures 5.2c–j, 5.3c–j show the simulated reflectivity in MYN250, ADM250, DDF250, and DDF050. The spatial resolution of radar simulation is the same as that of radar observation. All the experiments successfully simulated the overall structure of Faxai, including the eyewall and rainbands. The locations of the eyewall in these experiments are close to those of the observation, with a displacement error of 10–20 km. We considered the effects of attenuation due to precipitation in the simulation of reflectivity where there is strong precipitation along the beam path in the I-simulator; this allows direct comparison between the simulated radar reflectivities and the C-band radar observations. In the PPI and RHI cross-sections, the eyewalls were simulated at a distance of around –50 km from the radar site at 1800 UTC (Fig. 5.2) and –30 km at 1900 UTC (Fig. 5.4). The reflectivity at an altitude of 5–10 km is stronger in the simulations

than in observations, indicating an overprediction of ice phase hydrometeors in our model. The reflectivity above the melting level, especially for convective echo, seems to be stronger in MYN250 (Figs. 5.2d, 5.4d), ADM250 (Figs. 5.2f, 5.4f), and DDF250 (Figs. 5.2h, 5.4h) than in observations (Figs. 5.2b, 5.4b).

Figures 5.3c–h, k, l, 5.5c–h, k, l show the simulated Doppler velocity in MYN250, ADM250, DDF250, and DDF050. As indicated by the vertical dashed-dotted line in Figs. 5.3b, d, f, h, columnar discontinuity of positive Doppler velocity at radii between +20 km and +40 km by convection in the rainband is simulated well at 1800 UTC. However, below an altitude of 2 km, the difference between the experiments is more evident. The positive (negative) Doppler velocity in the negative (positive) distance shows the inflow. Figure 5.3 shows that inflow layer is thinner in both DDF250 and DDF050 than in both MYN250 and ADM250. Figure 5.5 shows that at 1920 UTC, the height of the inflow layer is not significantly different between the experiments. However, both Figs. 5.3 and 5.5 show that both DDF250 and DDF050 predict a complex structure by rolls (see section 5.4.5 for further discussion).

5.4.3. Azimuthally averaged values

We azimuthally averaged the results of simulations for the region around the center of Typhoon Faxai to focus on the secondary circulation. As shown in Figure 5.6a, the locations of the simulated TCs in all experiments are slightly different. Thus, we examined the sensitivity of secondary circulation to the schemes using 1-hour averaged values of forecast data at 10-minute intervals from 1700 UTC to 1800 UTC on 8 September 2019. Note that DDF050 is not shown here, because D3 is not large enough to calculate the azimuthally averaged values. The area to be azimuthally averaged was east of the TC center, because the axisymmetric structure was significantly deformed on land to the west of Faxai, as shown in Fig. 5.7.

Figures 5.8a–c shows the azimuthally averaged mass stream function (Schubert and Hack, 1983), showing the inflow toward the TC center near the surface and the outflow toward the outside of the TC in the upper levels. The outflow becomes stronger at altitudes above 10 km. Figure 5.8b shows that the inflow layer below an altitude of 2 km in ADM250 is very similar to that in MYN250, but the outflow above an altitude of 2.5 km is larger in ADM250 than in MYN250. The thickness and magnitude of the inflow layer near the earth’s surface are thinner and stronger in DDF250 than in MYN250, respectively (Fig. 5.8c). The outflows corresponding to eyewall clouds and rainbands are stronger in DDF250 than in MYN250.

Figures 5.8d–f shows the tangential velocity v_t . The altitude of the tangential wind core is slightly higher (lower) in ADM250 (DDF250) than in MYN250 (Figs. 5.8e, f). As the tangential wind core is produced at

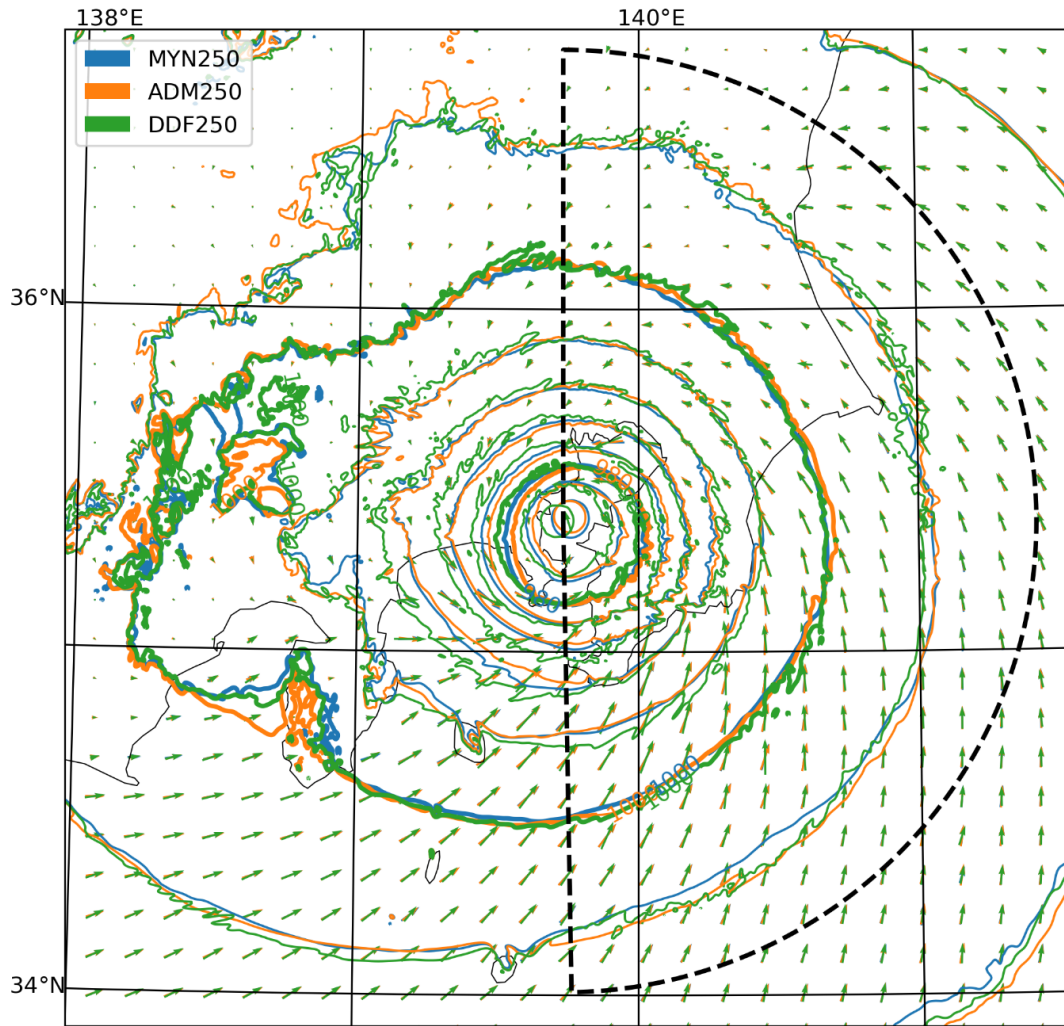


FIG. 5.7. Pressure (contoured lines) at sea level and wind (arrows) at an altitude of 10 m. MYN250 (blue), ADM250 (orange), and DDF250 (green) at 1800 UTC on 8 September 2019. The dashed line indicates the computation region of azimuthally averaged values.

the transition level between the inflow and outflow (e.g., Kepert 2010), the altitudes of the tangential wind core depend on the thickness of the inflow.

Figures 5.8g–i shows the azimuthally averaged vertical mass flux. The simulated vertical mass fluxes have strong peaks around the eyewall cloud at a radius of 30 km and weaker peaks around the rainband at a radius of 60 km and 100 km. The vertical mass flux at a radius of 40–80 km is stronger in ADM250 than in MYN250 (Fig. 5.8h). The vertical mass flux at a radius of 20–40 km is stronger and more concentrated toward the TC center in DDF250 than in MYN250.

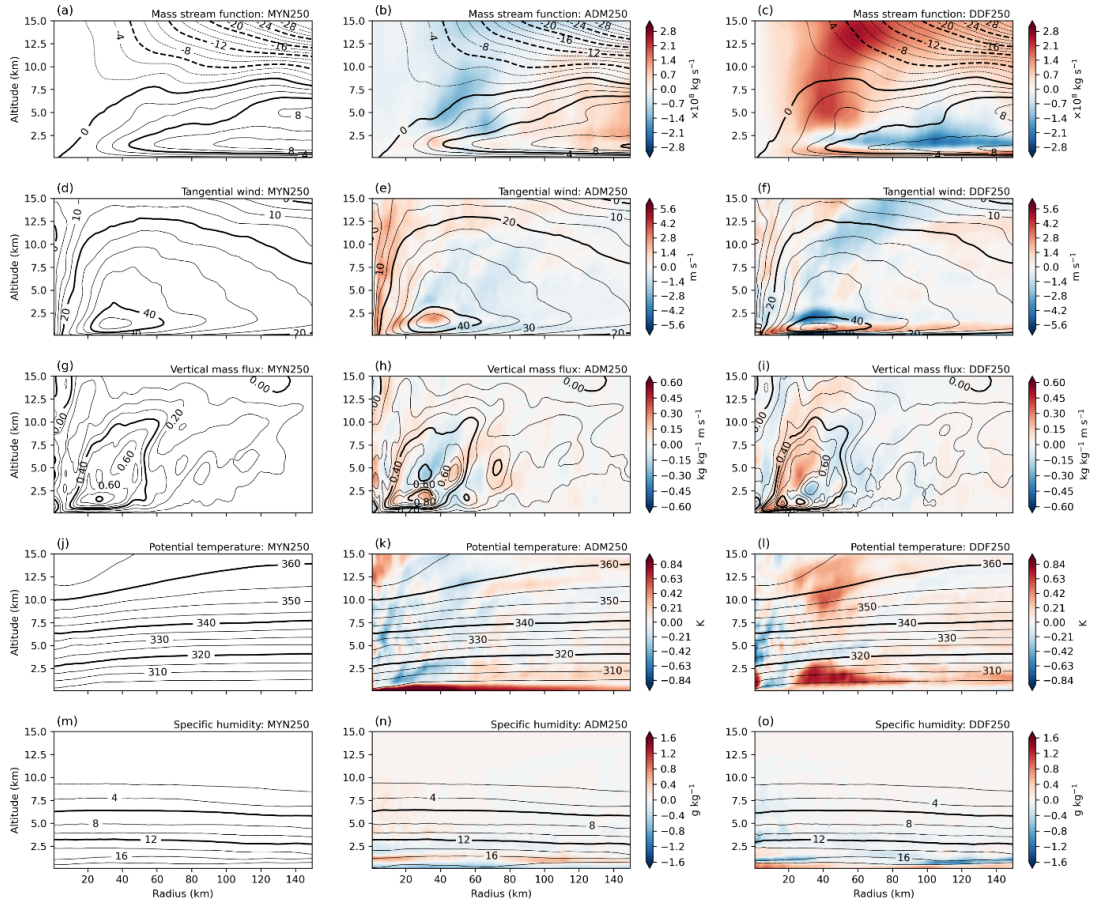


FIG. 5.8. Azimuthally averaged (a)–(c) mass stream function (10^8 kg s^{-1}), (d)–(f) tangential wind (m s^{-1}), (g)–(i) vertical mass flux (kg kg^{-1}), (j)–(l) potential temperature (K), and (m)–(o) specific humidity (g kg^{-1}). Contours show (left) MYN250, (middle) ADM250, and (right) DDF250. Shading indicates (middle) ADM250 minus MYN250 and (right) DDF250 minus MYN250.

The potential temperature is warmer in ADM250 than in MYN250 below an altitude of 1 km (Fig. 5.8k). This indicates that the near-surface air is mixed more strongly in ADM250 than in MYN250. The potential temperatures are similar near the surface in DDF250 and MYN250 (Fig. 5.8l). At altitudes of 1–3 km, the transport of lower-potential temperature air masses to the upper layers increases (decreases) in the region where the vertical flux of both ADM250 and DDF250 are stronger (weaker) than those of MYN250.

Figures 5.8m–o shows the azimuthally averaged specific humidity. The specific humidity near the surface is lower in ADM250 than in MYN250, and the specific humidity around an altitude of 1.2 km is higher in ADM250 than in MYN250. This indicates that the near-surface moist air is mixed more strongly in ADM250 than in MYN250. The specific humidity near the earth’s surface is higher in DDF250 than in

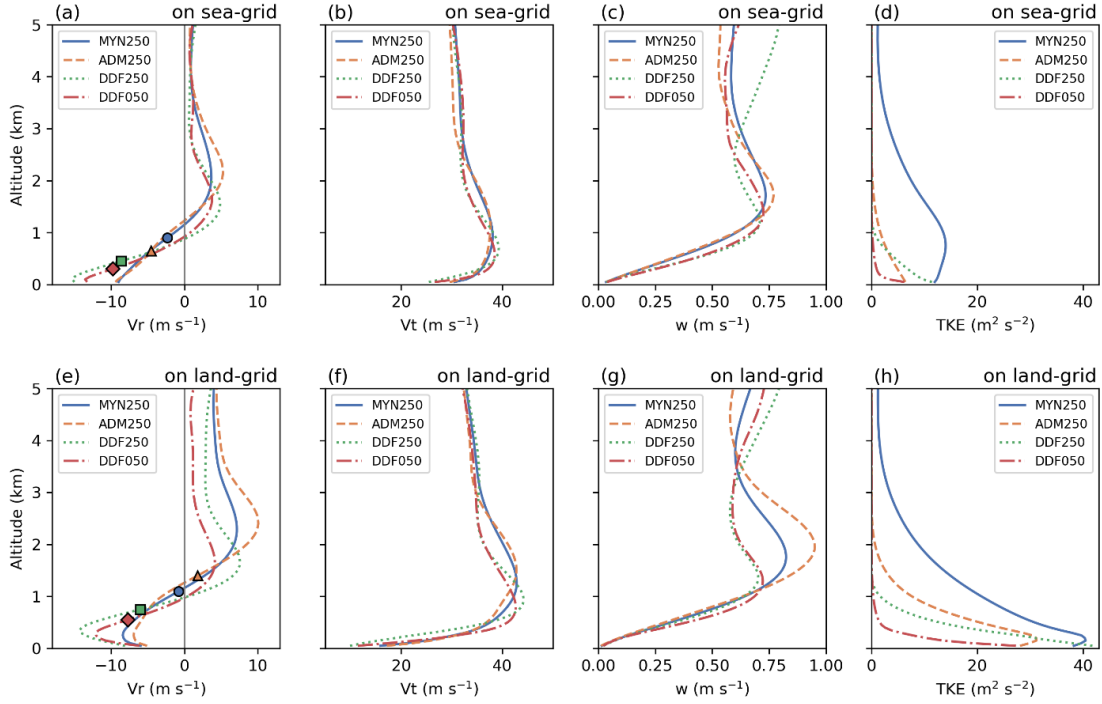


FIG. 5.9. Averaged vertical profiles of (a), (e) v_r ; (b), (f) v_t ; (c), (g) w ; and (d), (h) TKE in MYN250 (solid), ADM250 (dashed), DDF250 (dotted), and DDF050 (dash-dotted). (a)–(d) Sea grid and (e)–(h) land grid profiles. Filled circles, triangles, squares, and diamonds are inflection points in MYN250, ADM250, DDF250, and DDF050, respectively.

MYN250. This indicates that the more humid air is confined closer to the surface in DDF250 than in MYN250, because the thickness of the inflow layer is thinner in DDF250 than in MYN250.

5.4.4. Budget analysis

The averaged profiles of the radial velocity v_r , the tangential velocity v_t , the vertical velocity w , and the sub-grid scale turbulence kinetic energy (TKE) below an altitude of 5 km on grid points over sea and on land are shown in Fig. 5.9. However, the sea-land division for budget analysis is not rigorous, as advection is significant on both sides of the coastline and adjustment of turbulence takes place. These profiles were averaged over a 20–45 km radius from the center of the TC in D3 outside the sponge layer using forecast data at 10-minute intervals between 1700 UTC and 1800 UTC on 8 September 2019. The velocities v_r , v_t , and w were calculated in the cylindrical coordinate system centered on Typhoon Faxai. The height and magnitude of inflow in MYN250 are almost the same as those in ADM250, and those in DDF250 are almost the same as those in DDF050 (Figs. 5.9a,e). The height of inflection points on sea (land) grid points in MYN250, ADM250, DDF250, and DDF050 are 0.9 (1.1), 0.6 (1.3), 0.4 (0.7), 0.3 (0.5) km, respectively. The altitude of the v_t peak in DDF250 is similar to that in DDF050 and lower than that in MYN250 and ADM250. The vertical velocity w on grid points over the sea is larger in DDF050 than in MYN250, ADM250, and DDF250 above the altitude of 3 km (Fig. 5.9c). The vertical velocity w

for grid points over land is larger in MYN250 and ADM250 than in DDF250 and DDF050 between an altitude of 1 and 3 km and is similar in DDF250 and in DDF050 below the altitude of 3 km (Fig. 5.9g). In DDF050, the vertical flux in the lateral sponge layer is damped to $0 \text{ kg m}^{-2} \text{ s}^{-1}$ toward the lateral boundary. Therefore, w is underestimated in DDF050 in the southern sea grid, where inflow from the lateral boundary is predominant. Figure 5.9d shows that the TKE is the largest in MYN250 and remains up to an altitude of 3 km. The TKE in ADM250 is larger than that in DDF250 at altitudes above 600 m and smaller than that in DDF250 near the surface. The TKE of ADM250 disappears above an altitude of 2 km. The TKE is larger in DDF250 than in DDF050. The TKE of DDF250 and DDF050 disappears above an altitude of 1 km. The difference in sub-grid scale TKE between DDF050 and other experiments is due to the fact that it does not include TKE for grid-resolved motions whose horizontal scale is between 50m and 250m. The magnitudes of TKE on sea grid points are about 1/3 of those on land grid points (Figs. 5.9d,h).

The contribution of production terms to the tendency of TKE E is estimated by the following diagnostic equation:

$$\frac{\partial E}{\partial t} = A + S + B + T - \text{Dissipation terms}, \quad (5.1)$$

$$A = -\mathbf{v} \cdot \nabla E, \quad (5.2)$$

$$S = S_{rv} + S_{tv} + S_{hh} + S_{hv}, \quad (5.3)$$

$$S_{rv} = -\langle w' v_r' \rangle \frac{\partial v_r}{\partial z} - \langle v_r' w' \rangle \frac{\partial w}{\partial r}, \quad (5.4)$$

$$S_{tv} = -\langle w' v_t' \rangle \frac{\partial v_t}{\partial z} - \frac{\langle v_t' w' \rangle}{r} \frac{\partial w}{\partial \varphi}, \quad (5.5)$$

$$S_{hh} = -\langle v_r' v_r' \rangle \frac{\partial v_r}{\partial r} - \frac{\langle v_t' v_r' \rangle}{r} \frac{\partial v_r}{\partial \varphi} - \langle v_r' v_t' \rangle \frac{\partial v_t}{\partial r} - \frac{\langle v_t' v_t' \rangle}{r} \frac{\partial v_t}{\partial \varphi}, \quad (5.6)$$

$$S_{vv} = -\langle w' w' \rangle \frac{\partial w}{\partial z}, \quad (5.7)$$

$$B = \frac{g}{\theta} \langle w' \theta' \rangle, \quad (5.8)$$

and

$$T = -\nabla \langle \mathbf{v}'^{(E+p')} \rangle, \quad (5.9)$$

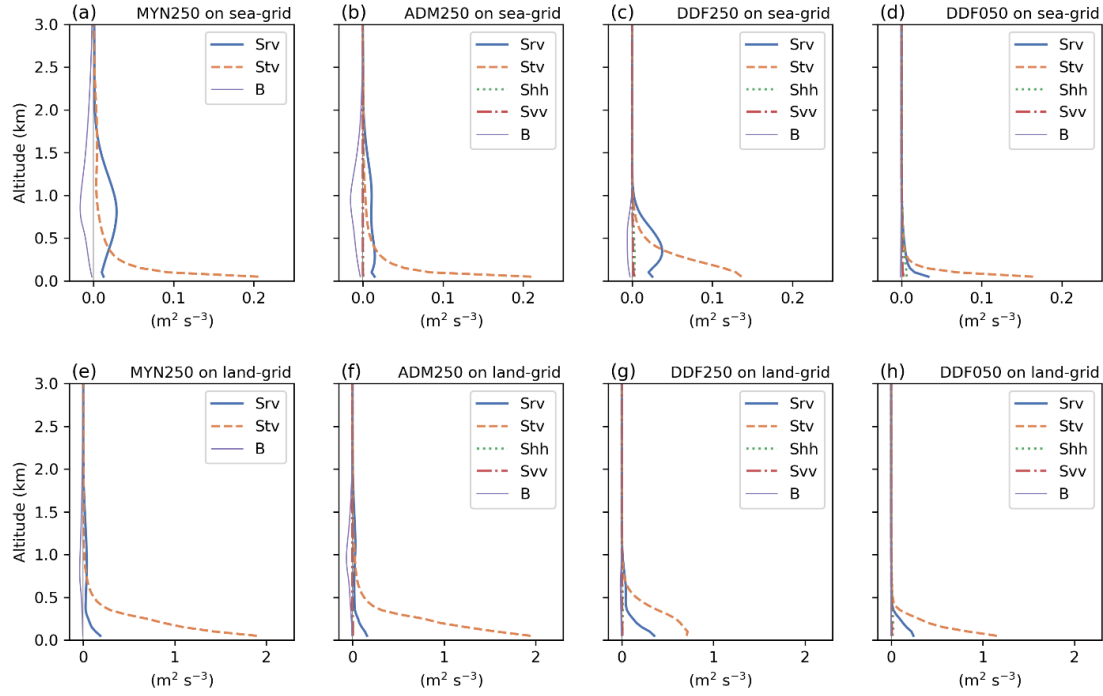


FIG. 5.10. Averaged vertical profiles of Srv (solid), Stv (dashed), Shh (dotted), Sv (dash-dotted), and B (thin solid) in (a), (e) MYN250; (b), (f) ADM250; (c), (g) DDF250, and (d), (h) DDF050. (a)–(d) Sea grid and (e)–(h) land grid profiles

where r , φ , and z are the radius, azimuth angle, and height of the cylindrical coordinate system centered at the TC center, respectively; the prime variables are turbulent variables; the brackets indicate the ensemble average of the sub-grid scale; A is the advection term; Srv, Stv, Shh, and Sv are the shear production terms; B is the buoyancy production term; T is the turbulent transport term; and p and g are kinematic pressure and gravitational acceleration, respectively. The sub-grid scale turbulent momentum fluxes are computed from the output of each PBL scheme. For example, in the case of ADM, it is given by Eqs. (1)–(3) in Kitamura (2016). Figure 5.10 shows the profile of shear production terms and buoyancy terms. The averaging domain and period are the same as Fig. 5.9. The magnitude of the shear production terms is smaller on sea grid points than on land grid points. The shear production terms Shh and Sv are ignored in the MYNN3 scheme but can be computed in the ADM and DDF schemes. In MYN250, the contribution of Stv is large and that of Srv is small (Figs. 5.10a,e). In ADM250, as in MYN250, the contribution of Stv is large and that of Srv is small, while Shh and Sv contribute almost nothing (Figs. 5.10b,f). In DDF250 and DDF050, the contribution of Stv is large and Srv is small. Srv in DDF250 contributes a larger percentage of the overall shear production than in ADM250. The contribution of Shh and Sv is relatively small in ADM250, DDF250, and DDF050. The vertical shear of the horizontal wind such as Srv and Stv contribute significantly to the production of TKE in the sub-grid scale shear production terms in all experiments. The shear production is almost zero above 0.5 km in

DDF050 and above 1 km in DDF250. The shear production in MYN250 and ADM250 remains above 1 km. These differences in shear production are related to the fact that the TKE in MYN250 and ADM250 remains up to 3 km.

Using the simplified anelastic equation, the tendency of vertical velocity w is diagnosed as follows:

$$\begin{aligned} \frac{\partial w}{\partial t} = & \text{ArW} + \text{AtW} + \text{AzW} \\ & + \text{DrW} + \text{DtW} + \text{DzW} - \frac{1}{\rho} \frac{\partial p}{\partial z} - g, \end{aligned} \quad (5.10)$$

$$\text{ArW} = -v_r \frac{\partial w}{\partial r}, \quad (5.11)$$

$$\text{AtW} = -\frac{v_t}{r} \frac{\partial w}{\partial \varphi}, \quad (5.12)$$

$$\text{AzW} = -w \frac{\partial w}{\partial z}, \quad (5.13)$$

$$\text{DrW} = -\frac{\partial \langle w' v_r' \rangle}{\partial r}, \quad (5.14)$$

$$\text{DtW} = -\frac{1}{r} \frac{\partial \langle w' v_t' \rangle}{\partial \varphi}, \quad (5.15)$$

and

$$\text{DzW} = -\frac{\partial \langle w' w' \rangle}{\partial z}, \quad (5.16)$$

where ρ is air density. Figure 5.11 shows the profiles of the advection terms and the divergence terms of the turbulence flux. The averaging domain and period are the same as Fig. 5.10. The contribution of turbulent flux terms is smaller than that of the advection term in all experiments. In all schemes, AtW profiles on sea grid points are negative, whereas AtW profiles on land grid points are positive except near the surface. This is because the tangential winds are slower (faster) over land (sea), and $\partial w / \partial \varphi$ becomes negative (positive). MYN250 has a small negative tendency related to near-surface inflow below an altitude of 2 km, which is contributed by ArW and AzW (Figs. 5.11a,e). ArW and AzW above 3 km are negative due to outflow into the upper troposphere along the eyewall. ADM250 has almost the same profile as MYN250 (Figs. 5.11b,f). However, due to the different thicknesses of the inflow layer in these two experiments, the altitudes of the ArW and AzW maxima in ADM250 are slightly higher than those in MYN250. In DDF250, ArW , AtW , and AzW are negative below an altitude of 1.2 km and are positive at an altitude of 1.2–3 km (Figs. 5.11c,g). These negative tendencies are related to the near-surface inflow,

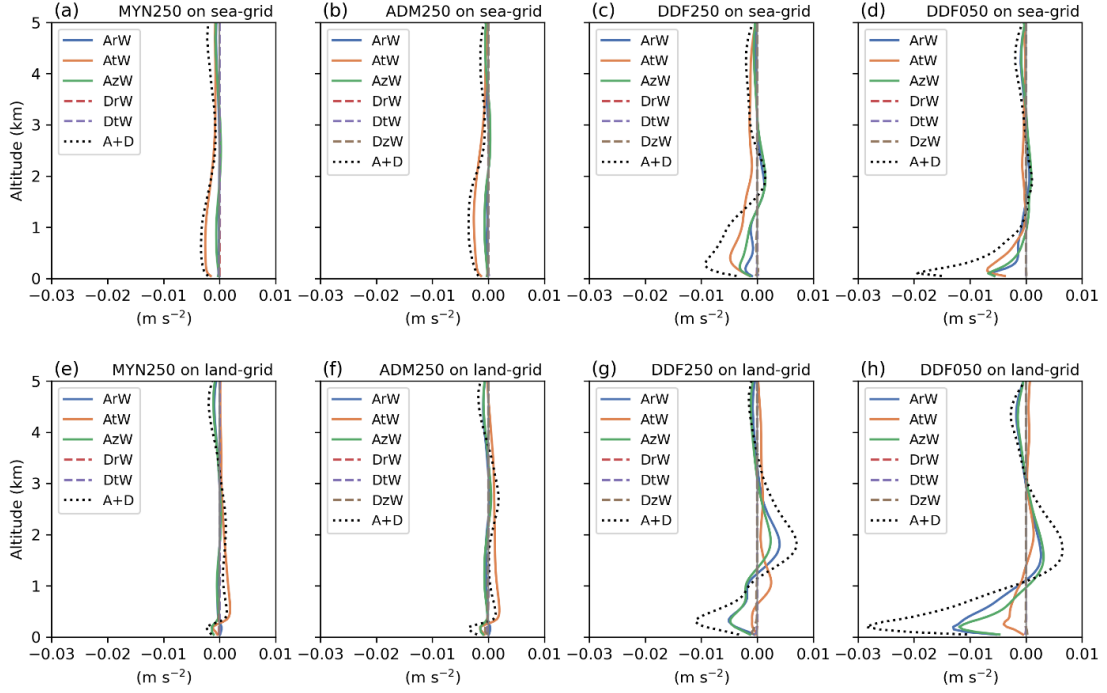


FIG. 5.11. Tendency of vertical velocity in (a), (e) MYN250; (b), (f) ADM250; (c), (g) DDF250; and (d), (h) DDF050. Advection terms are ArW (blue solid line), AtW (orange solid line), and AzW (green solid line). Divergence terms of turbulence flux are DrW (red dashed line), DtW (purple dashed line), and DzW (brown dashed line). Sum of ArW, AtW, AzW, DrW, DtW, and DzW (black dotted line). (a)–(d) Sea grid and (e)–(h) land grid profiles

whereas the positive tendencies are related the outflow layer over the top of the BL. In DDF050, ArW and AtW are negative below an altitude of 1 km, and their magnitudes are larger over land than over sea (Figs. 5.11d,h). In the DDF250 and DDF050, the horizontal inflow enhanced in the BL contributes to the advection of updrafts and enhances the updrafts above the BL. These results indicate that the budget profiles in DDF250 are closer to those in DDF050 than to those in MYN250 and ADM250, although their magnitudes are smaller, partly because this budget targets sub-grid scale turbulence.

5.4.5. Circulation structures in the planetary boundary layer

In this subsection, we further examine the detailed structure of the circulation inside the PBL by focusing on the comparison between the simulated and observed Doppler velocity. Figure 5.12 shows the observed Doppler velocity, simulated Doppler velocity, and w of the PPI scan at an elevation angle of 0.7° in the region indicated by the thick line in Figure 5.3i. The simulated TC centers have some positional errors from the observations, as shown in Fig. 5.6a. To avoid a mismatch due to the positional errors, the valid

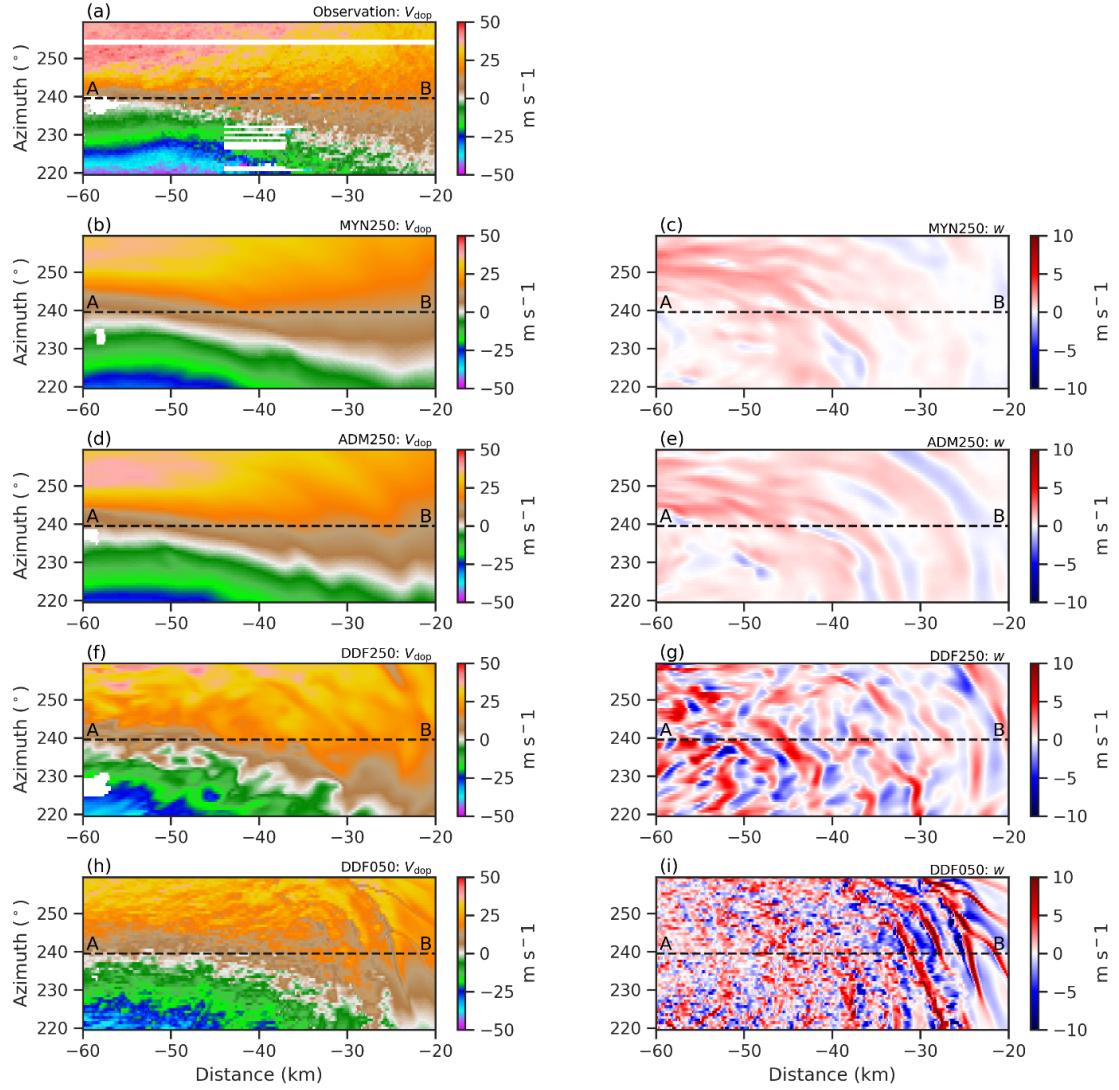


FIG. 5.12. (left) Doppler velocity and (right) w at an elevation angle of 0.7° in the region indicated by the thick line in Fig. 5.3i, for (a) observation, (b, c) MYN250, (d, e) ADM250, (f, g) DDF250, and (h, i) DDF050. Valid times are (a) 1840 UTC, (b–e) 1820 UTC, (f, g) 1810 UTC, and (h, i) 1800 UTC on 8 September 2019. Noise is seen in the observed Doppler velocity field at a distance of -45 to -35 km and an angle of around 220° to 240° in (a). The dashed line from A to B in each panel shows the location of the cross-section (Fig. 5.13).

times when the Doppler velocity patterns are close to the observation were selected: They are 1840, 1820, 1810, and 1800 UTC, for MYN250, ADM250, DDF250, and DDF050, respectively (Figs. 5.12, 5.13).

The Doppler velocities in MYN250 (Fig. 5.12b) and ADM250 (Fig. 5.12d) are less turbulent and smoother than those of the observation. The Doppler velocity in DDF250 (Fig. 5.12f) has an organized structure of about 5 km wavelength, which is not found in the observation. This organized structure is associated with a positive and negative pair of vertical velocities (Fig. 5.12g). Figure 5.12h shows that DDF050 produces turbulence having smaller scale than does DDF250, and its

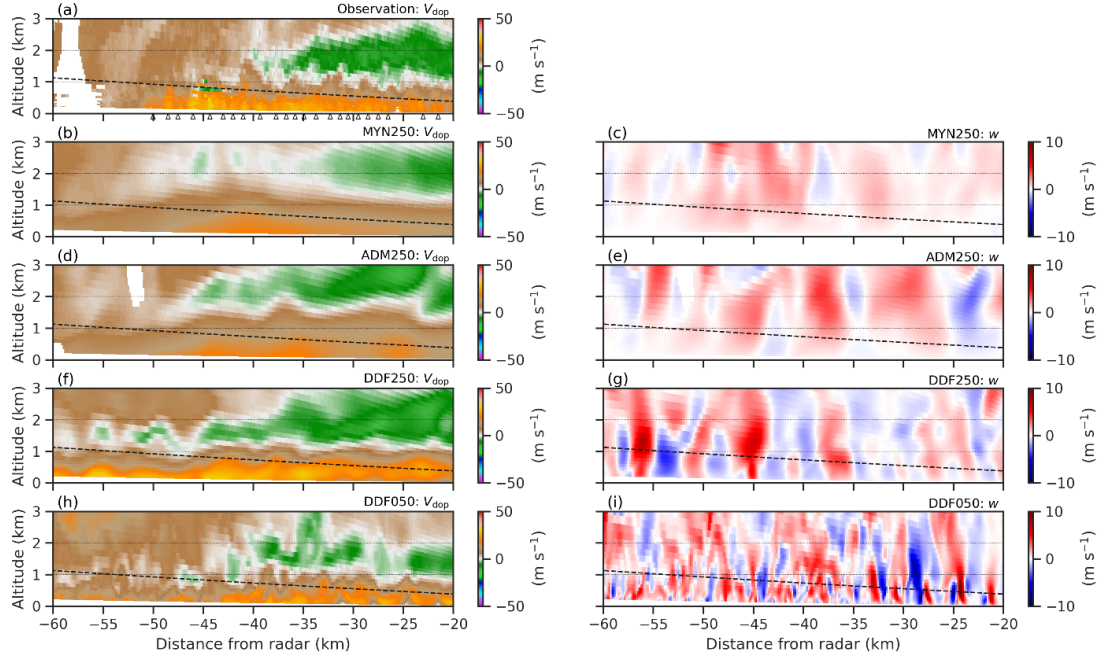


FIG. 5.13. As in Fig. 5.12, but the cross-section is of the beam path of the RHI scan. The dashed line shows the beam path at an elevation of 0.7° . Triangles indicate the approximate location of the peak of observed oscillation.

scale is closer to the observation. Comparison of the vertical velocities for DDF250 (Fig. 5.10g) and DDF050 (Fig. 5.10i) shows that turbulence has a smaller-scale structure in DDF050 than in DDF250. The horizontal scale of the upward and downward flow pairs in DDF050 seems to be $1/3$ – $1/2$ smaller than that in DDF250.

Figure 5.13 shows the Doppler velocity and vertical velocity on a cross-section of the RHI beam scan along the dashed line from A to B in Figure 5.12. In the RHI scan of observation, the positive Doppler velocity below an altitude of 1.5 km indicates the inflow in the BL, and the negative Doppler velocity at an altitude of 1.5–2 km indicates the outflow above the BL (Fig. 5.13a). The Doppler velocity in the observation presents an oscillatory pattern with a wavelength of about 1 km below an altitude of about 1 km. This pattern is formed by the rolls in the BL (e.g., Morrison et al. 2005). These rolls, which are typically seen in the TCBL, are caused by inflection-point instability (e.g., Nakanishi and Niino 2012; Gao and Ginis 2014). The simulated Doppler velocity and vertical velocity in MYN250 and ADM250 do not show a clear oscillatory structure (Figs. 5.13b–e); it is speculated that the effects of the rolls are involved in the parameterized turbulence. In DDF250, the wavelength of oscillation is longer than in the observation (Fig. 5.13f), and the positive and negative pairs of vertical velocities correspond to oscillations of the Doppler velocity (Fig. 5.13g). The oscillation

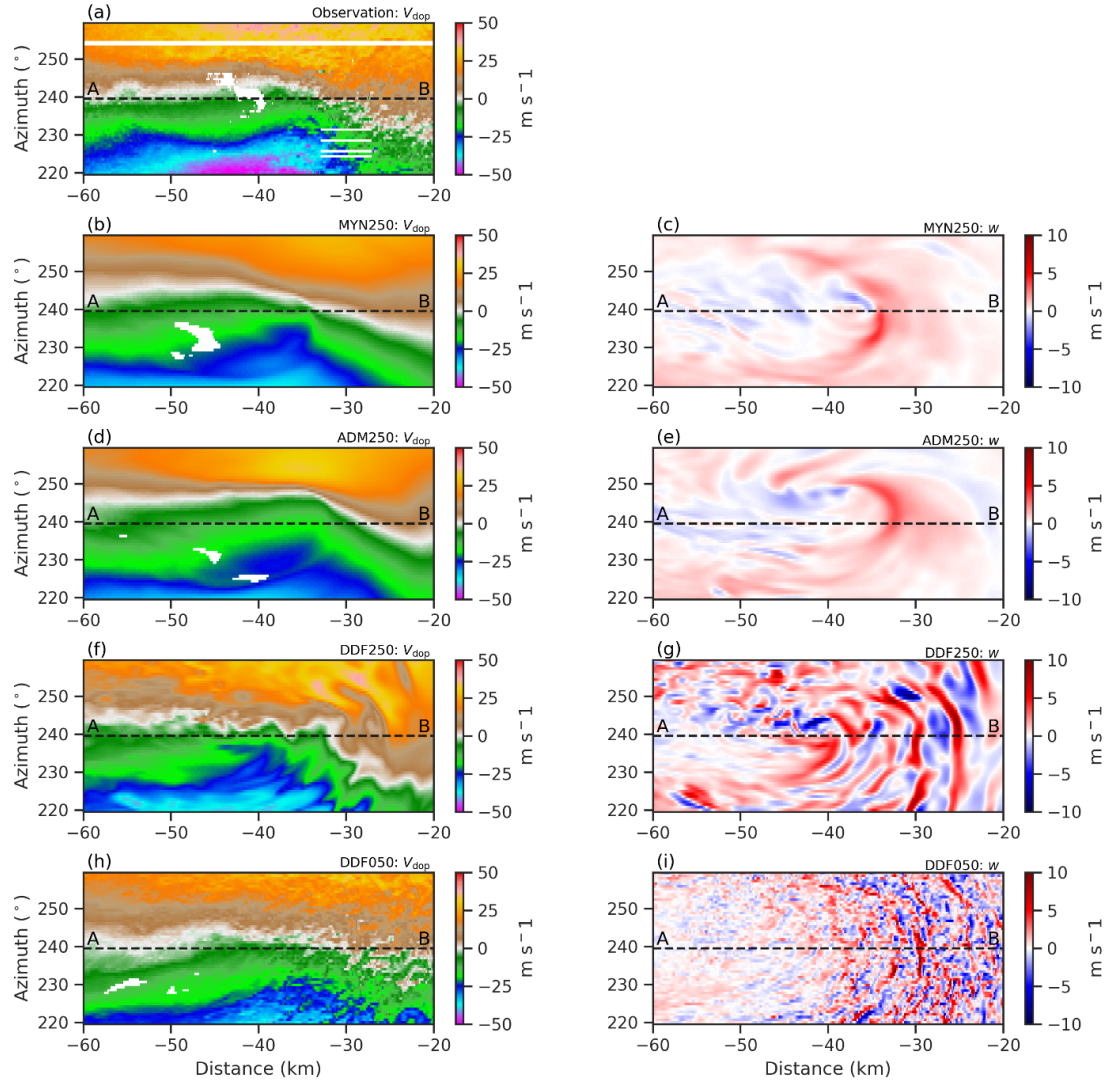


FIG. 5.14. As in Fig. 5.12, but valid times are (a) 1920 UTC, (b–g) 1910 UTC, and (h, i) 1900 UTC 8 September 2019. Noise is seen in the observed Doppler velocity field at a distance of -35 to -25 km and an angle of around 220° to 230° in (a). The dashed line from A to B in each panel shows the location of the cross-section (Fig. 5.15).

in DDF050 is the closest to the observation among the four experiments (Fig. 5.13h). Below an altitude of 0.5 km, the positive and negative pairs of vertical velocities have a structure of smaller scale in DDF050 than in DDF250 (Fig. 5.13i).

The RHI scan nearly crossed the eye of Faxai at 1920, 1910, 1910, 1910, and 1900 UTC, for the observation, MYN250, ADM250, DDF250, and DDF050, respectively (Figs. 5.14, 5.15). The eye of the TC was located at a distance of about -40 km from the radar, but the observed and simulated locations did not match well. Even near the TC center, the inflow altitudes were

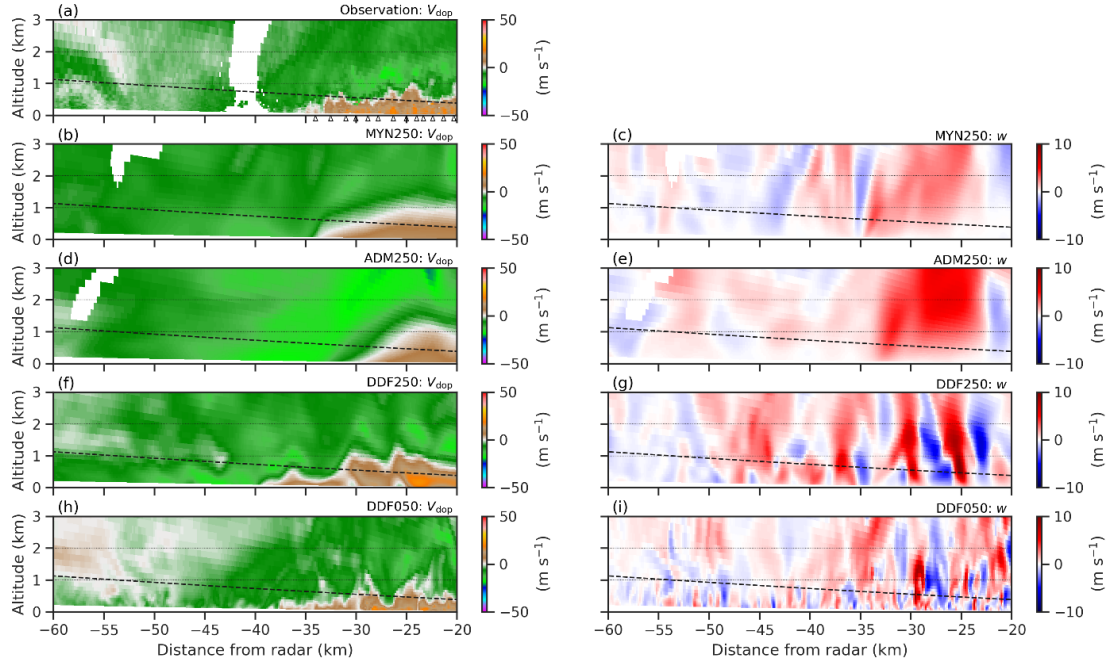


FIG. 5.15. As in Fig. 5.14, but the cross-section is of the beam path of the RHI scan. The dashed line shows the beam path at an elevation angle of 0.7° . Triangles indicate the approximate location of the peak of observed oscillation.

higher in MYN250 (Fig. 5.15b) and ADM250 (Fig. 5.15d) than in observations, but were close to observations in DDF250 (Fig. 5.15f). Figure 5.15a shows that the rolls exist in the observed inflow near the surface with positive Doppler velocity. Figures 5.15b–e show that the MYNN3 and ADM schemes do not produce rolls. DDF050 has up-down flow pairs that correspond to rolls below an altitude of 0.5 km (Fig. 5.15i). The horizontal scale of the up-down flow pairs predicted in DDF250 (Fig. 5.15g) is excessive compared to that in DDF050.

Next, the evaluation results for the observed Doppler velocities are presented. Figure 5.16 shows the CFADs of the absolute error, which is the difference between the simulated and observed Doppler velocities. The absolute error is calculated using the RHI scan data during the period from 1700 to 1900 UTC. At an altitude of 0.5 km, the mode values of CFAD over sea (land) grid points in MYN250, ADM250, DDF250, and DDF050 are about 10 (12), 12 (12), 0 (0), and 0 (0) m s^{-1} , respectively. The mode values are large at an altitude of 0.5–1 km in MYN 250 and ADM250 because the model inflow layer is thicker than the observation. In particular, the error is largely due to the existence of the outflow ($v_r > 0$) layer above the inflow ($v_r < 0$) layer. DDF250 and DDF050 do not have such non-zero peaks. However, DDF050 has a large random error, which is due to the small misalignment of rolls at an altitude of 0.5 km. The mode values at an altitude of 4 km on sea (land) grid points in MYN250, ADM250, DDF250, and DDF050 are about 6 (4), 6 (2), 2 (0), and 0 (2) m s^{-1} , respectively. The non-zero peaks are shown

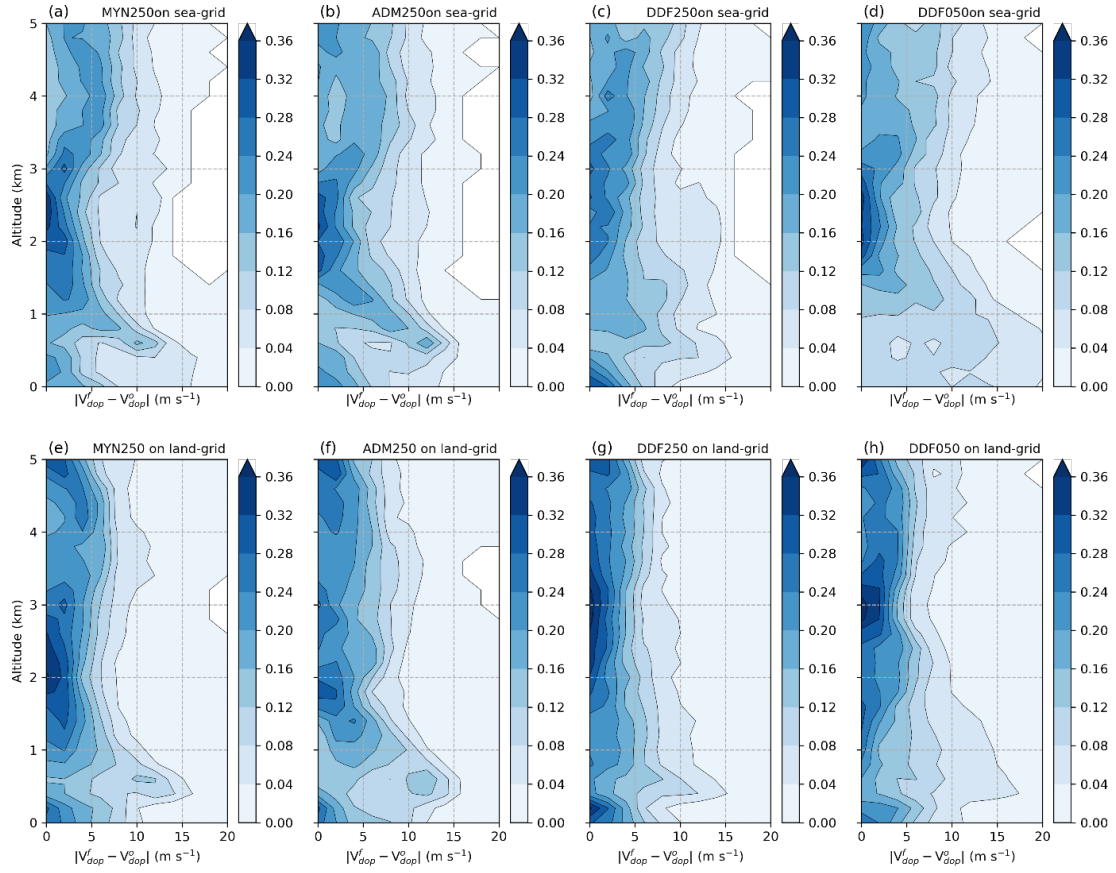


FIG. 5.16. Contoured frequency and altitude diagrams of the absolute error for Doppler velocity in (a), (e) MYN250; (b), (f) ADM250; (c), (g) DDF250; and (d), (h) DDF050. (a)–(d) Sea grid and (e)–(h) land grid profiles averaged within D3.

more clearly in MYN250, ADM250, and DDF250 than in DDF050 (Fig. 5.16). In this study, no quality control method has been established to reject observation noise as seen in Figs. 5.12a, 5.14a. Therefore, the CFADs in Fig. 5.16 may contain errors due to noise in the observations.

5.4.6. Spatial frequency

The amplitudes and wavelengths of the detailed structures of the BL are compared between the four simulations and the observations in terms of the Doppler velocity. For comparing the effective resolution of NWP models, spectral analysis methods are often used (e.g., Skamarock 2004). Figure 5.17 shows the time-averaged power spectrum of the spatial structure of the Doppler velocity. The horizontal axis of Fig. 5.17 is the wavenumber along the beam path from the radar site. Here, we specifically analyzed the PPI scan at an elevation angle of 0.7° (the altitudes of the elevations shown in RHI scans; e.g., Figs. 5.2–5.5). The PPI data used for the spectral analysis were observed and simulated at 10-minute intervals between 1700 UTC and 1900 UTC on 8 September 2019. The validated simulation data are from within D3 and the southwest quadrant of the radar site for all experiments. In a rotating wind field such as a TC, the

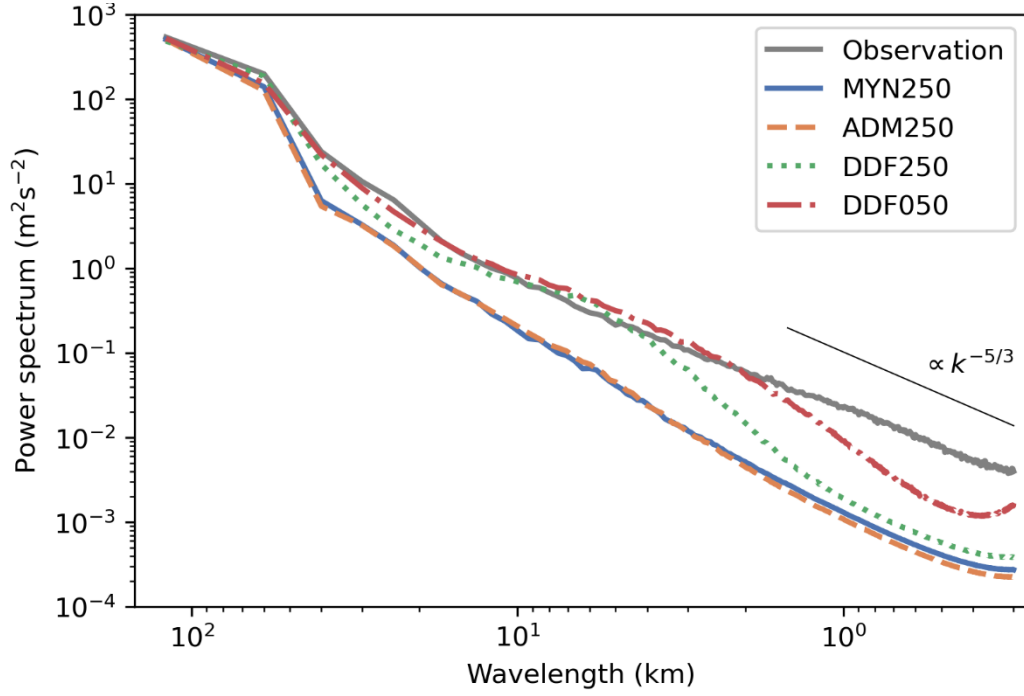


FIG. 5.17. Power spectrum of Doppler velocity at PPI scan of elevation angle 0.7° at each wavelength in observation (gray), MYN250 (blue), ADM250 (orange), DDF250 (green), and DDF050 (red). The black line is the reference line, which is proportional to the $-5/3$ power of the wavenumber k .

sign of the Doppler velocity changes in the radial direction from the radar site. The wavelength of the sign change of the Doppler velocity is considered to be much larger than that of the rolls and is reflected in a large wavelength range in the spectral analysis. In the gray-zone simulation, the Doppler velocities in DDF250 are closer to the observations than those in both MYN250 and ADM250. The power spectrum is smaller in MYN250 and ADM250 than in the observation for all wavelengths. The power spectrum in DDF250 is close to the observation for wavelengths larger than 3 km, slightly larger than the observation for wavelengths around 8 km, and smaller than the observation for wavelengths less than 3 km. The power spectrum in DDF050 is the closest to observation for all wavelengths, especially above 2 km. The slope of the power of the observation is approximately equal to the slope of the reference line, which is proportional to the $-5/3$ power of the wavenumber. At the short wavelength, the slope of the power spectrum in DDF250 is steeper than the observation and the reference line. This is consistent with the fact that the oscillation patterns of Doppler velocity due to the rolls simulated by DDF250 were larger than the observed oscillation pattern of Doppler velocity, as shown in Fig. 5.13. Comparison of the power spectrum of Doppler velocity in the gray-zone experiments again indicates that the smaller scale structures of the BL in DDF250 are closer to the observation than those in MYN250 and ADM250.

5.5. Conclusion

In this study, to explore the possibility of developing a higher-resolution numerical model for improved operational weather prediction, we simulated Typhoon Faxai using the JMA's NWP model ASUCA with a horizontal grid spacing of 250 m, a resolution in the gray zone, and with a horizontal grid spacing of 50 m, which was used as a reference in the LES regime. Four experiments using the MYNN3, ADM, and DDF schemes with a horizontal grid spacing of 250 m (referred to as MYN250, ADM250, and DDF250, respectively) and the DDF scheme with a horizontal grid spacing of 50 m (referred to as DDF050) were conducted to investigate the dependency of the detailed structure of the BL on the PBL scheme. We compared the results of our simulations with the radar observation, which captured the detailed structure of Faxai. In the gray-zone experiments with a horizontal grid spacing of 250 m, the simulated Doppler velocities near the BL were closer to the observations in DDF250 than in MYN250 and ADM250.

Analysis of the secondary circulation with azimuthal averages showed that inflow was thinner and had stronger wind speeds in DDF250 than in MYN250. The inflow was slightly weaker in ADM250 than in MYN250. The updraft was slightly stronger, particularly around the eyewall, in DDF250 than in MYN250. Vertical diffusion by the PBL scheme was suppressed more in DDF250 than in MYN250, resulting in the advection of near-surface inflow momentum toward the TC center without significant vertical diffusion. The budget analysis for the TKE showed the magnitude of shear production terms was smaller in DDF250 than in MYN250 and ADM250, and the difference between the TKE in these experiments depended on the characteristics of shear production. The budget analysis for the updraft showed that the advection term due to the inflow inside the BL contributed mainly to updraft in DDF250.

The inflows simulated in MYN250, ADM250, DDF250, and DDF050 were compared with the Doppler observations, focusing on the microstructure inside the BL. The heights of the BL in both DDF250 and DDF050 were closer to observation than were those in both MYN250 and ADM250. The Doppler observations captured the oscillatory structure, which is thought to be associated with the rolls that are often observed in the TCBL at altitudes below 1 km. MYN250 and ADM250 did not predict rolls, because rolls were included in the parameterized turbulence. DDF250 predicted excessive rolls, while DDF050 predicted the rolls most accurately. MYN250 and ADM250 had large TKE in the PBL scheme, meaning that vertical diffusion was large. This vertical diffusion included vertical mixing by unresolved rolls as a sub-grid-scale phenomenon. In MYN250 and ADM250, the PBL height was larger than observation, indicating that parameter tuning of the PBL scheme is needed. The vertical profiles of the absolute error of Doppler velocity clearly showed that both MYN250 and ADM250 had a large error of inflow height both at sea and on land (Fig. 5.16).

The wavelengths and amplitudes of the fine structure of the simulated Doppler velocity were compared with the observations. The amplitudes in MYN250 and ADM250 were smaller than the observations at almost all wavelengths, while the amplitudes in DDF250 were comparable or slightly larger than

observations for wavelengths of 6–8 km. The amplitudes in DDF250 were closer to the observation than were those in MYN250 and ADM250 but further than that of DDF050. Together, these results indicate that DDF250, although more realistic than both MYN250 and ADM250, did not adequately reproduce the fine structure of the PBL. In summary, the effects of the MYNN3, ADM, and DDF schemes on the secondary circulation are evident mainly in the lower-level inflow and the updraft distribution at the TC center. There is also a clear difference in the reproducibility of the rolls in the inflow. However, the intensity and the track of Faxai did not differ significantly between the experiments using these three schemes. This indicates that the MYNN3 and ADM schemes properly incorporate rolls as a subgrid-scale phenomenon into the parameterized turbulence, albeit with somewhat excessive BL height.

Many studies have investigated the sensitivity of the secondary circulation of TCs to the PBL scheme. However, few studies have examined this sensitivity by comparing it with fine-scale radar observations in the gray zone, particularly using observation simulators for direct comparison between simulations and observation, as in this study. A quantitative comparison of the model and observation in the observed space of Doppler velocities enabled us to validate the PBL scheme of the numerical model. The validation results presented in this study provide an indication of the best choice of MYNN3, ADM, or DDF schemes in the gray zone. For instance, if we focus on the predictability of inflow height near the surface, the application of the DDF scheme is more suitable than both the MYNN3 and ADM schemes. Furthermore, if we focus on the predictability of roll vortices, the DDF scheme with a horizontal grid spacing of 250 m is inadequate, while the DDF scheme with a horizontal grid spacing of 50 m performs better. The results of this study are also useful for determining what parameters need to be tuned in order to optimize the MYNN3 and ADM schemes, since the BL height in both MYN250 and ADM250 is higher than in the observation.

We chose the ADM scheme as one of several possible gray-zone schemes, as reviewed by Honnert et al. (2020). We showed in this study that the DDF scheme provides the best results, and the ADM scheme as a gray-zone scheme still has room for progress. However, we note that other gray-zone schemes might provide better results than those presented here, and it is left for future studies to compare the various gray-zone schemes.

Although the intensity and structure of wind gusts and rainfall of landfalling TCs, such as the one examined in this study, are important for predicting the damage after landfall, the interaction between the BL and rainfall has not yet been studied in detail. In the future, it will be important to investigate the effects of other physical processes, such as cloud microphysics, on the extent of damage after landfall, in addition to further increasing the model resolution and taking into account the interaction between the atmosphere and the land. The research project ULTIMATE, of which the present study forms a part, evaluates and improves cloud physics processes and other processes in numerical models using high-density and detailed observation data from remote sensing, such as phased array radar and lidar in the Tokyo area. We

expect to conduct a more comprehensive validation of numerical models and improve them with the goal of achieving better NWP for the extent of damage after the landfall of TCs.

6. General discussion

6.1. Effective observation for evaluation

We have shown the results of the validation and improvement of the cloud microphysics scheme using GPM satellite observations: we identified problems in the cloud microphysics scheme based on GPM satellite observations, validated the scheme using brightness temperature and reflectivity, and modified the scheme in Chapter 3. The cloud microphysics scheme is validated and improved using polarimetric radar as reference values in Chapter 4. A new normalized PSD was created using polarimetric parameters and disdrometer and added to the scheme. In addition, snow particles with different shapes were added to the snow category with reference to the polarimetric parameters.

Remote sensing used as a reference has several limitations in observational accuracy. Polar-orbiting satellite observations have a low temporal resolution because the time interval between revisits is about half a day. Geostationary meteorological satellites have high temporal resolution but provide mainly horizontal information and lack vertical information. Ground-based radars often have higher temporal and spatial resolution than satellite observations but are difficult to install at sea. Shipboard radars are limited in their observation range on navigation routes. From the above, to increase the reliability of verification results, it is necessary to use a variety of data, not just a single remote sensing observation.

For validation of the NWP model, preferred observations should be those of weather elements that have feedback to the model. Observations of the same meteorological elements as the forecast elements are most important. For example, sonde observations of temperature and water vapor are essential for model validation. However, some elements are difficult to observe, such as vertical velocity, hydrometeors, and turbulence. Such predictors that are difficult to observe are indirectly verified by comparing observed and diagnostic values. For example, the reflectivity can provide evidence of the predictive certainty of hydrometeors, K_{DP} can provide evidence of the modeling certainty of particle shape of hydrometeors, and the Doppler velocity can provide evidence of the modeling certainty of atmospheric motion.

One caveat to verification is which physical quantity to verify. For example, if only precipitation is verified, it is not possible to detect deviations from reality in the distribution of hydrometeors in the atmosphere. The problem becomes more complex when errors in atmospheric water quality are offset by errors in physical processes other than the cloud physics scheme. In model development, old schemes are replaced by new schemes as the understanding of physical principles improves and the performance of computers improves. However, introducing a new scheme does not necessarily improve performance if the old scheme cancels out the errors in the other scheme. This is called the compensating error problem and is considered problematic in the field of NWP model development (Jacob 2003; Naggers and Siebesma 2013; McTaggart-Cowan et al. 2019). To avoid compensating errors, it is important to examine the problem from multiple perspectives. In this study, to avoid such issues, a multifaceted validation of

the cloud microphysics scheme was conducted using satellite observations, ground-based radar, and a disdrometer. However, there are still issues to be addressed in the validation of the cloud microphysics scheme. For example, very short time-scale phenomena such as the life cycle of isolated cumulus clouds have not been verified. One possible solution to this issue is the use of phased-array radar, which can observe on the order of a few seconds. Another issue is the inability to directly verify particles inside precipitation systems. Direct observation of particles in the atmosphere, for example by using video sondes, is needed to reduce uncertainty.

6.2. Universality of improvement

Attention should also be paid to the meteorological phenomena to be verified. Precipitation, for example, varies greatly in characteristics depending on the season and latitudinal zone. Characteristic precipitation phenomena include rain bands associated with tropical cyclones, frontal precipitation associated with extratropical cyclones, precipitation caused by rainy season fronts, and snowfall in winter. Even if we focus only on precipitation, it can be broadly classified into stratiform and convective rainfall, which have characteristics that vary greatly depending on the season and latitudinal zone. However, we do not believe it is necessary to examine all of these meteorological phenomena. From a microphysical point of view, the shapes of snow particles are mainly determined by temperature and the saturated water vapor content (e.g. Magono and Lee 1966). It is also known that a diagram of the frequency distribution of reflectivity at each temperature, called Contoured Frequency by Temperature Diagram, is useful for organizing the correspondence between observed signals and cloud microphysical processes (Hashino et al. 2013). Thus, the temperature-dependent improvements in this study may be universally applicable to a variety of cases. The fact that the impact of the scheme improvements was similar in both TC and snowfall cases suggests that the improvements in this study may have universality. However, the distribution of hydrometeors depends not only on the temperature but also on the transport by the vertical flow and the horizontal advection from the adjacent precipitation system. To take the research a step further and make the scheme more universal, it is necessary to carefully classify the phenomena, identify the strengths and weaknesses of the scheme, and solve the problems that have been identified.

6.3. Effects of snow shape on the atmosphere

The shape of snow particles changes the magnitude of the tendencies of individual processes in the cloud microphysical scheme. Specifically, the dimensionless capacitance decreases by about 60% as the aspect ratio of the particles changes from 1.0 to 0.125. A decrease in capacitance reduces the evaporation efficiency. Therefore, cooling (heating) by evaporation (deposition) becomes weaker. Particles of different shapes also have different fall velocities. For example, dendritic particles have a higher falling velocity than spherical particles. As the number of particles with slow-falling velocity per unit volume increases, snow tends to remain in the air. The increase in snow increases cooling (heating) by evaporation (deposition). In this study, two types of snow particles other than spherical were added. As a result, the total heating increased by 2.1% in latent heat heating in the upper air due to the change in the capacitance and the

increase in the number of particles. This means that the shape of snow particles affects the atmospheric heat balance.

6.4. Dependency on resolution

In Chapter 5, we presented the results of the validation of the TCBL using Doppler velocities: in the gray zone, the prediction of the BL thickness is compared with Doppler observations, showing the difference in prediction accuracy between the BL schemes. The detailed structure within the TCBL was validated with Doppler observations, and the scheme and resolution dependence of the prediction of rolled convection was shown. For the 250 m horizontal grid spacing, RANS and the gray zone scheme failed to predict rolled convection, and LES overpredicted small organized structures in BL such as rolled convection because it explicitly computed grid-scale eddies. The difference in the scale of rolled convection had a small effect on the BL height. This means that the LES has the best reproduction performance when focusing on km-scale atmospheric circulation without focusing on the detailed structure within the BL. This suggests the usefulness of LES in models belonging to the gray zone. Currently, in the gray zone, it is necessary to select a BL scheme and adjust parameters according to the phenomena to be studied and the resolution of the model. In doing so, validation with observational data is essential, as shown in this study. Numerical forecast models used in the operational NWP center are expected to continue to increase in resolution. The current high-resolution regional models in operation at each of the NWP centers have a grid spacing of a few kilometers: DWD uses ICON-D2 (Zängl et al. 2015) with a ~ 2.2 km grid spacing, JMA operates LFM with a 2 km grid spacing around Japan area (JMA et al. 2019), the UK MetOffice uses the 1.5 km grid spacing UK Variable resolution model (UKV) with a 1.5 km grid length over the British Isles (Lean et al., 2008), and the French Meteorological Office uses AROME (Seity et al., 2011) with a 1.3 km grid length. Since those models belong to the gray zone, development studies are underway to reduce the forecast errors in the scheme; UK MetOffice is leading a study in the gray zone project using a model with an $O(100\text{ m})$ to $O(5\text{ km})$ grid spacing (Tomassini et al. 2018). Although the resolution of the NWP model is expected to be even higher in the future, there are currently no clear plans for a higher-resolution model that would break out of the gray zone. While not aimed at solving the gray zone problem, research is being conducted related to the Olympic Games using future high-resolution NWP models. NWP model with a grid spacing of 3-5 km was used for the Beijing 2008 Olympic Games; Environment-Canada simulated the urban climate of Vancouver using a 250 m grid spacing during the Vancouver 2010 Olympic and Paralympic Games (Leroy et al. 2011). The UK MetOffice operated "London model" (Boutle et al. 2016) with a grid spacing of 333 m for the London 2012 Olympic Games; kilometeric models were used for the Sochi 2014 Olympic Games (Kiktev et al. 2017). For the next Research Demonstration Project Paris 2024 Olympics, the use of 100 m out of the gray zone is being considered (Masson 2020). The resolution of the operational NWP models is improving to keep pace with the resolution of these studies of the research demonstration project for the Olympics. In the future, the operational

NWP model will also have a grid spacing of less than 1 km. The results of this study will provide significant insight into the future operation of NWP models that belong to the gray zone.

7. General conclusion

7.1. Improvement of cloud microphysics scheme

In Chapter 3, the cloud microphysics scheme of the JMA regional model used in the current work was validated using GPM core satellite observations. The results showed that the previously used M1702 scheme had very large errors in cloud and precipitation forecasts. Specifically, TBs with low GMI were not reproduced with low predicted cloud ice. The Ku and Ka precipitation radar reflectivity simulated from the predictions was underestimated in both the lower and upper layers; a comparison of the KuPR and KaPR relationships revealed a high amount of hail; and a high amount of cloud ice was found in the TBs with low GMI. Based on this evaluation from GPM satellite observations, a single-column kinematic model was used to determine the source of error in the original cloud microphysics scheme. Sensitivity experiments using the single-column kinematic model led to the development of the M2003 scheme as a new cloud microphysics scheme by modifying the following three points. First, the conversion rate from cloud ice to snow was changed. The physical rationale for these changes comes from the definition of ice and snow classification. The next step is to change the terminal velocity of the cloud ice. This is a change in the falling velocity of cloud ice from that of larger ice particles to that of smaller ice particles. third, the size distribution of raindrops was changed from the AB scheme to the MP scheme. This change is aimed at reducing excessive evaporation.

In the precipitation forecast validation, MP2003 showed significant improvement for weak precipitation. The sonde validation also showed that MP2003 improved the specific humidity bias in the lower layers. Atmospheric temperature predictions also showed that MP2003 improved over MP1702 with a reduced low temperature bias in the upper and lower layers. The changes in this study were simple, but improvements were obtained. In other words, the prediction accuracy was found to be improved by increasing the total balance of the microphysical scheme process without using a complex scheme.

Many such cloud microphysics verifications based on satellite observations had been conducted. In recent years, cloud microphysics schemes used by operational NWP centers in the world, including Japan, have also been validated based on satellite observations. We have demonstrated the usefulness of the GPM satellite for validating cloud microphysics schemes. As a result, the new cloud microphysics scheme resulting from this study was introduced into the JMA's operational mesoscale NWP system on March 26, 2020 (Ikuta et al. 2020).

In Chapter 4, precipitation forecasts were validated using dual-polarization radar and a disdrometer. The results of validation showed that the original scheme MPOLD had an overestimation of Z_{DR} below the melting layer and an underestimation of Z_{DR} above the melting layer. The bias of predicted K_{DP} was also similar to that of Z_{DR} . This was due to the large number of raindrops in the MPOLD and the spherical shape of the snow. To address these issues, a new scheme MPNEW was developed. In the MPNEW,

the PSD of rain was updated based on disdrometer observations, and the snow category was divided into three types of snow particles: dendrites, which are aggregates that fall slowly at low temperatures. By changing the PSD for rain and expanding the snow category to three categories, Z_{DR} and K_{DP} are close to being observed in MPNEW. The PSDs predicted by the model were also close to the MPNEW disdrometer observations. This improvement resulted in increased latent heating in the upper troposphere.

As reviewed by Morrison et al. (2020), many schemes have been proposed; Chem et al. (2020) and Jesen and Harrington (2015) have incorporated particle shape into cloud microphysical preference schemes, but in many popular schemes, particle shape has been treated as a simplification. Therefore, the effect of particle shape on predictions has not been investigated in detail. There are also a limited number of studies that validate hydrometeorology inside clouds by comparing polarimetric radar observations with models (e.g., Matsui et al. 2020; Shrestha et al. 2022). This study is a rare one that introduces particle shape into a cloud microphysics scheme using radar observations as a constraint. The introduction of particle shape into the scheme, while keeping it consistent with dual-polarization radar observations, changes the latent heat heating rate from hydrometeors in the atmosphere. This suggests the importance of particle shape in the atmospheric heat budget.

The cloud microphysics scheme developed in this study is consistent with observations, improves forecast accuracy, and greatly aids in understanding the mechanisms of weather phenomena. However, the results of this study have limitations because they are based on the validation and improvement of rain and snow particles. Also, the modeling in this study is not sufficient to reproduce the complexity of actual snow. In addition, uncertainties regarding assumptions of cloud ice and cloud water remain high, partly due to the lack of sufficient observational data. In the future, we hope to reduce the uncertainty by utilizing new observational data.

7.2. Evaluation of turbulence schemes

In Chapter 5, to explore the possibility of improving operational weather forecasting by developing a higher resolution numerical model, the JMA's NWP model ASUCA was used to simulate typhoon Faksai with a horizontal grid spacing of 250 m, which is the resolution of the gray zone, and a horizontal grid spacing of 50 m used as a reference in the LES region. The simulation results were compared to radar observations that captured the detailed structure of Faxai. In a gray zone experiment with a horizontal grid spacing of 250 m, simulated Doppler velocities near BL were closer to observations for DDF250 than for MYN250 or ADM250.

Analysis of secondary circulation by azimuthal averaging showed thinner inflow and stronger wind speeds for DDF250 than for MYN250; for ADM250, inflow was slightly weaker than for MYN250. Upwelling was slightly stronger in DDF250 than in MYN250, especially near the eyewall; vertical diffusion due to the PBL scheme was more suppressed in DDF250 than in MYN250, resulting in the advection of near-surface inflow momentum toward the TC center without much vertical diffusion. The TKE budget

analysis showed that the magnitude of the shear generation term was smaller for DDF250 than for MYN250 or ADM250, indicating that the difference in TKE in these experiments depends on the shear generation characteristics. The upwelling budget analysis showed that the advection term due to inflow inside the BL contributed mainly to the upwelling in DDF250.

Inflow simulations of MYN250, ADM250, DDF250, and DDF050 were compared to Doppler observations, focusing on the microstructure inside the BL; the BL heights of DDF250 and DDF050 were closer to observations than those of MYN250 and ADM250. The Doppler observations captured oscillatory structures thought to be related to the roll often observed in TCBLs below 1 km altitude; MYN250 and ADM250 did not predict roll due to the inclusion of roll in the parameterized turbulence; DDF250 predicted excessive roll and DDF 050 predicted roll most accurately; MYN250 and ADM250 had greater TKE in the PBL scheme, meaning greater vertical diffusion. This vertical diffusion included vertical mixing due to unresolved rolls as a subgrid-scale phenomenon; MYN250 and ADM250 had larger PBL heights than observed, indicating the need for parameter tuning of the PBL scheme.

The wavelengths and amplitudes of the simulated Doppler velocity microstructures were compared to the observations: the amplitudes of MYN250 and ADM250 were smaller than the observations at almost all wavelengths, while the amplitude of DDF250 was equal to or slightly larger than the observations at wavelengths of 6-8 km. The amplitudes of DDF250 were closer to the observed values than the amplitudes of MYN250 and ADM250, but farther away than the amplitude of DDF050. These results indicate that DDF250, although more realistic than MYN250 and ADM250, does not adequately reproduce the microstructure of the PBL.

MYN250 and ADM250 cannot predict rolls explicitly. The vertical transport due to rolls in MYN250 and ADM250 is predicted as a subgrid-scale phenomenon that is grid averaged. The intensity of this averaged vertical transport determines the height of the lowest inflow. In the simulations in this study, the lowest inflow heights in MYN250 and ADM250 were slightly larger than those in DDF050. Focusing on the vertical transport inside the lowest inflow, Fig. 5.11 shows that the grid-scale vertical transport in MYN250 and ADM250 is smaller than that in DDF050. In other words, sub-grid-scale vertical transport is dominant in MYN250 and ADM250, while grid-scale vertical transport is dominant in DDF050. Although the former and the latter use different methods to predict vertical transport, the difference in the height of the inflow is small, indicating that the total vertical transport due to rolls is similar. This indicates that the MYNN3 and ADM schemes, although with somewhat excessive BL heights, reasonably incorporate rolls as a subgrid-scale phenomenon into the parameterized turbulence. However, the detailed vertical structure inside the boundary layer of both MYN250 and ADM250 is different from that of the reference value DDF050. Many studies have investigated the relationship between the PBL scheme and

TCBL (e.g., Keppert 2001; Keppert and Wang 2001). Some observations of TCBL by radar have also been reported (e.g., Kosiba and Wurman 2014). However, few studies have examined the TCBL in the gray zone in comparison with radar observations. In particular, few studies directly compare simulations with observations using an observation simulator, as in this study. We were able to validate the PBL scheme of the numerical model by quantitatively comparing the model and observations in the Doppler velocity observation space. The validation results presented in this study indicate the optimal choice of MYNN3, ADM, and DDF schemes in the gray zone.

As reviewed by Honnert et al. (2020), there are several gray zone schemes; the ADM was selected from among them. This study shows that the DDF gives the best results and that there is still room for progress in the ADM as a gray-zone method. However, we note that other gray-zone methods may provide better results than the methods presented here, and it is left to future research to compare the different gray-zone methods.

The intensity and structure of wind gusts and rainfall at landfalling TCs, as discussed here, are important for predicting damage after landfall, but the interaction between BL and rainfall has not yet been studied in detail. In the future, it will be important to further improve the resolution of the model and to investigate the influence of other physical processes, such as cloud microphysics, on the extent of post-landfall damage, in addition to considering the interaction between the atmosphere and land.

7.3. Conclusion

Improvements in the cloud microphysics scheme yielded dramatic improvements in the reproducibility of brightness temperature, reflectivity, and polarimetric parameters. These improvements were made by upgrading the cloud microphysics scheme. The fundamental processes that resulted in improved predictions were found to be the rate of ice-to-snow conversion and the particle size distribution of raindrops. It was also found that the use of non-spherical particles improves the vertical distribution of water properties. These changes were found to affect the atmospheric temperature distribution through radiative and latent heat. In particular, the introduction of non-spherical snow flow resulted in latent heating at altitudes where solid precipitation was present. In addition to improving these physical quantities, improvements in observational simulations are also very useful in data assimilation to reduce the mismatch between observations and models. Validation of the TCBL using Doppler velocity revealed the BL scheme dependence and resolution dependence of the TCBL. In the TCBL, the prediction of rolls contributing to vertical transport was important for the accuracy of BL height in the gray zone. MYN250 and ADM250 include the effect of rolls in the vertical transport as a sub-grid scale phenomenon. The BL heights in MYN250 and ADM250, although reasonably well predicted, are higher than observed because the optimal parameters for the gray zone are not yet known. The DDF250 explicitly predicts the rolls responsible for vertical transport as a grid-scale phenomenon, and the BL height is found to be close to the observation. However,

DDF250 in the gray zone was found to have the issue that the horizontal scale of the rolls is larger than that of observations and DDF050. Focusing on the vertical structure inside the typhoon, the wind speed of the inflow inside the TCBL in DDF250 was the largest in this study. According to the budget analysis, this strengthening of inflow in the TCBL contributed to the increase of the updraft around the eye wall. This study was unprecedented in that it demonstrated the reproducibility of boundary layer heights by Doppler velocity simulations. We believe that focusing on the reproducibility of the spatial distribution of water quality, particle shape, and the internal structure of the BL will greatly advance the improvement of the physics scheme and the understanding of cloud precipitation processes, and contribute to the reduction of uncertainties in the internal structure of precipitation and cloud precipitation processes. In addition, the improved scheme in this study is supported by observations and improves the reliability of forecasting the vertical profiles of momentum and mass of hydrometeors in the interior of precipitation systems. Numerical forecast models with improved reliability lead to improved accuracy in numerical weather forecasting, which in turn improves the safety and quality of life in society. Furthermore, the results of this research, which will lead to improved reproducibility of polarimetric parameters, will be essential for polarimetric radar assimilation technology. In addition, simulations using the scheme developed in this study will provide a more accurate vertical structure of physical quantities. The results will facilitate the development of meteorological science by elucidating the mechanisms of weather phenomena. In addition, using the results to improve numerical forecast models will constitute a cycle of application and research that will provide positive feedback to each other. We will continue to use this research as a foundation to pioneer developmental research and further advance both applications and research.

Appendix

List of acronyms

| | |
|-----------|---|
| ADM | Anisotropic Deardorff Model |
| AROME | Application of Research to Operations at Mesoscale |
| ASUCA | ASUCA is a System based on a Unified Concept for Atmosphere |
| ASUCA-Var | Variational Data Assimilation System Based on ASUCA |
| BL | Boundary Layer |
| CFAD | Contoured Frequency by Altitude Diagram |
| CPR | Cloud Profiling Radar |
| CRess | Cloud Resolving Storm Simulator |
| CRM | Cloud-Resolving Model |
| DDF | Deardorff |
| DFR | Dual-Frequency Rate |
| DPR | Dual-frequency Precipitation Radar |
| DWD | Deutscher Wetterdienst |
| ETS | Equitable Threat Score |
| EUMETSAT | European Organisation for the Exploitation of Meteorological Satellites |
| FV3 | Finite-Volume Cubed-Sphere Dynamical Core |
| GFS | Global Forecast System |
| GMI | GPM Microwave Imager |
| GPM | Global Precipitation Measurement |

| | |
|----------|---|
| JAXA | Japan Aerospace Exploration Agency |
| JMA | Japan Meteorological Agency |
| KaPR | Ka-band Precipitation Radar |
| KiD | Kinematic Driver Model |
| KuPR | Ku-band Precipitation Radar |
| LES | Large Eddy Simulation |
| LFM | Local Forecast Model |
| ME | Mean Error |
| MSM | Meso-Scale Model |
| MY | Mellor-Yamada |
| MYNN | Mellor-Yamada-Nakanishi-Niino |
| MYNN3 | Mellor-Yamada-Nakanishi-Niino level 3 |
| NEXRAD | Next Generation Weather Radar |
| NHM | Non-Hydrostatic Model |
| NICAM | Non-hydrostatic Icosahedral Atmospheric Model |
| NICT | National Institute of Information and Communications Technology |
| NWP | Numerical Weather Prediction |
| P3 | Predicted Particle Properties |
| PBL | Planetary Boundary Layer |
| POLARRIS | POLArimetric Radar Retrieval and Instrument Simulator |

| | |
|-------------|---|
| PPI | Plan Position Indicator |
| PR | Precipitation Radar |
| PSD | Particle Size Distribution |
| Py-ART | Python ARM Radar Toolkit |
| R/A | Radar/Rain-gauge-Analyzed Precipitation |
| RANS | Reynolds Averaged Navier-Stokes |
| RHI | Range Height Indicator |
| RMSE | Root Mean Square Error |
| RTTOV-SCATT | Rapid Radiative Transfer for TOVS for Scattering |
| SDSU | Satellite Data Simulator Unit |
| T3EF | TRMM Triple-Sensor Three-Step Evaluation Framework |
| TC | Tropical Cyclone |
| TCBL | Tropical Cyclone Boundary Layer |
| TMI | TRMM Microwave Imager |
| TRMM | Tropical Rainfall Measuring Mission |
| ULTIMATE | ULTra-sIte for Measuring Atmosphere of Tokyo metropolitan Environment |
| UKV | UK Variable Resolution Model |
| UM | Unified Model |
| ICON | Icosahedral Nonhydrostatic |
| WRF | Weather Research and Forecasting |

Acknowledgment

I would like to thank my dissertation committee chair, Prof. Kaoru Sato, for her generosity and patience. I am also grateful to Prof. Masaki Satoh, Prof. Yukari Takayabu, Prof. Kentaro Suzuki, and Prof. Hiroyasu Hasumi for serving as examiners. This dissertation is based on research conducted at the Atmosphere and Ocean Research Institute (AORI), The University of Tokyo, and the Meteorological Research Institute (MRI) of the JMA. I am grateful to Prof. Masaki Sato for his guidance throughout this study. I thank Dr. Woosub Roh, Dr. Shuhei Matsugishi, and Dr. Naomi Kuba at AORI, and Dr. Tatsuya Seiki at Japan Agency for Marine-Earth Science and Technology for discussions on cloud microphysical processes. Mr. Akihito Umehara and Dr. Hisaki Eito at MRI provided support for the use of polarimetric radar observation data. Dr. Masahiro Sawada and Mr. Hiroshi Kusabiraki at JMA provided useful comments on the physical process of JMA's NWP model and typhoon analysis. Dr. Takuji Kubota at JAXA provided advice on the utilization of satellite observation data. I am convinced that this has helped to enrich the content of this paper. I would like to express my gratitude to all of them for their cooperation.

This study was supported by the Program for Promoting Technological Development of Transportation (Ministry of Land, Infrastructure, Transport and Tourism of Japan) and by the Japan Society for the Promotion of Science (JSPS) KAKENHI Grant-in-Aid for Scientific Research B (20H01967) for Ultra Site for Measuring Atmosphere of Tokyo Metropolitan Environment and Collaboration Studies with High-Resolution Atmospheric Models (ULTIMATE). This research was supported by the Cooperative Program (147, 2021-2023) of Atmosphere and Ocean Research Institute, The University of Tokyo. Additionally, the authors gratefully acknowledge support from JSPS KAKENHI Grant 21K03669 and MEXT (JPMXP1020200305) "Program for Promoting Researches on the Supercomputer Fugaku" (Large Ensemble Atmospheric and Environmental Prediction for Disaster Prevention and Mitigation) (ID: hp200128, hp210166).

References

- Abel, S. J., and B. J. Shipway, 2007: A comparison of cloud-resolving model simulations of trade wind cumulus with aircraft observations taken during RICO. *Quart. J. Roy. Meteor. Soc.*, **133**, 781–794, <https://doi.org/10.1002/qj.55>.
- Abel, S. J., and I. A. Boutle, 2012: An improved representation of the raindrop size distribution for single-moment microphysics schemes. *Quart. J. Roy. Meteor. Soc.*, **138**, 2151–2162, <https://doi.org/10.1002/qj.1949>.
- Barreyat, M., P. Chambon, J.-F. Mahfouf, G. Faure, and Y. Ikuta, 2021: A 1D Bayesian inversion applied to GPM microwave imager observations: Sensitivity studies. *J. Meteor. Soc. Japan*, **99**, 1045–1070, <https://doi.org/10.2151/jmsj.2021-050>.
- Bauer, P., E. Moreau, F. Chevallier, and U. O’Keeffe, 2006: Multiple-scattering microwave radiative transfer for data assimilation applications. *Quart. J. Roy. Meteor. Soc.*, **132**, 1259–1281, <https://doi.org/10.1256/qj.05.153>.
- Beljaars, A. C. M., and A. A. M. Holtslag, 1991: Flux Parameterization over Land Surfaces for Atmospheric Models. *J. Appl. Meteor. Climatol.*, **30**, 327–341, [https://doi.org/10.1175/1520-0450\(1991\)030<0327:FPOLSF>2.0.CO;2](https://doi.org/10.1175/1520-0450(1991)030<0327:FPOLSF>2.0.CO;2).
- Bigg, E. K., 1953: The formation of atmospheric ice crystals by the freezing of droplets. *Quart. J. Roy. Meteor. Soc.*, **79**, 510–519, <https://doi.org/10.1002/qj.49707934207>.
- Boutle, I.A., A. Finnenkoetter, A.P. Lock, and H. Wells, 2016: The London Model: forecasting fog at 333 m resolution. *Quart. J. Roy. Meteor. Soc.*, **142**: 360–371, <https://doi.org/10.1002/qj.2656>.
- Brown, R. A., 1980: Longitudinal instabilities and secondary flows in the planetary boundary layer: A review. *Rev. Geophys.*, **18**, 683–697, <https://doi.org/10.1029/RG018i003p00683>.
- Brown, P. R. A., and P. N. Francis, 1995: Improved measurements of the ice water content in cirrus using a total-water probe. *J. Atmos. Oceanic Technol.*, **12**, 410–414, [https://doi.org/10.1175/1520-0426\(1995\)012<0410:IMOTIW>2.0.CO;2](https://doi.org/10.1175/1520-0426(1995)012<0410:IMOTIW>2.0.CO;2).
- Brown, A., S., Milton, M., Cullen, B., Golding, J., Mitchell, and A., Shelly, 2012: Unified modeling and prediction of weather and climate: a 25 year journey. *Bull. Amer. Meteor. Soc.*, **93**, 1865–1877, <https://doi.org/10.1175/BAMS-D-12-00018.1>, 2012.
- Carpenter, K.M. 1979: An experimental forecast using a non-hydrostatic mesoscale model. *Quart. J. Roy. Meteor. Soc.*, **105**, 629–655, <https://doi.org/10.1002/qj.49710544510>.

- Chambon, P., S. Q. Zhang, A. Y. Hou, M. Zupanski, and S. Cheung, 2014: Assessing the impact of pre-GPM microwave precipitation observations in the Goddard WRF ensemble data assimilation system. *Quart. J. Roy. Meteor. Soc.*, **140**, 1219–1235, <https://doi.org/10.1002/qj.2215>.
- Chen, J.-P., and D. Lamb, 1994: The theoretical basis for the parameterization of ice crystal habits: Growth by vapor deposition. *J. Atmos. Sci.*, **51**, 1206–1221, [https://doi.org/10.1175/1520-0469\(1994\)051<1206:TTBFTP>2.0.CO;2](https://doi.org/10.1175/1520-0469(1994)051<1206:TTBFTP>2.0.CO;2).
- Chern, J.-D., W.-K. Tao, S. E. Lang, X. Li, and T. Matsui, 2020: Evaluating precipitation features and rainfall characteristics in a multi-scale modeling framework. *J. Adv. Model. Earth Syst.*, **12**, e2019MS002007, <https://doi.org/10.1029/2019MS002007>.
- Cione, J. J., and Coauthors, 2020: Eye of the storm: Observing hurricanes with a small unmanned aircraft system. *Bull. Amer. Meteor. Soc.*, **101**, E186–E205, <https://doi.org/10.1175/BAMS-D-19-0169.1>.
- Co-hard, J.-M., and J.-P. Pinty, 2000: A comprehensive two-moment warm microphysical bulk scheme. 1. Description and tests. *Quart. J. Roy. Meteor. Soc.*, **126**, 1815–1842, <https://doi.org/10.1002/qj.49712656613>.
- Cotton, W. R., M. A. Stephens, T. Nehrkorn, and G. J. Tripoli, 1982: The Colorado State University three-dimensional cloud/mesoscale model—1982. Part II: An ice phase parameterization. *Journal de Recherches Atmospheriques*, **16**, 295–320.
- Cotton, R. J., and Coauthors, 2013: The effective density of small ice particles obtained from in situ aircraft observations of mid-latitude cirrus. *Quart. J. Roy. Meteor. Soc.*, **139**, 1923–1934, <https://doi.org/10.1002/qj.2058>.
- Deardorff, J. W., 1980: Stratocumulus-capped mixed layers derived from a three-dimensional model. *Bound.-Layer Meteor.*, **18**, 495–527, <https://doi.org/10.1007/BF00119502>.
- Durran, D. R., and J. B. Klemp, 1983: A Compressible Model for the Simulation of Moist Mountain Waves. *Mon. Wea. Rev.*, **111**, 2341–2361, [https://doi.org/10.1175/1520-0493\(1983\)111<2341:AC-MFTS>2.0.CO;2](https://doi.org/10.1175/1520-0493(1983)111<2341:AC-MFTS>2.0.CO;2).
- Duruisseau, F., P. Chambon, G. Faure, and A. Geer, 2018: Development of an active sensor module for the RTTOV-SCATT radiative transfer simulator. Ninth IPWG Workshop, Seoul, South Korea, IPWG, JP1.7, https://www.isac.cnr.it/~ipwg/meetings/seoul-2018/Posters/P1-21_Duruisseau.pdf.
- Eito, H., and K. Aonashi, 2009: Verification of Hydrometeor Properties Simulated by a Cloud-Resolving Model Using a Passive Microwave Satellite and Ground-Based Radar Observations for a Rainfall System Associated with the Baiu Front. *J. Meteor. Soc. Japan*, **87**, 425–446, <https://doi.org/10.2151/jmsj.87A.425>.

- Eitzen, Z. A., and K.-M. Xu, 2005: A statistical comparison of deep convective cloud objects observed by an Earth Observing System satellite and simulated by a cloud-resolving model. *J. Geophys. Res.*, **110**, D15S14. <https://doi.org/10.1029/2004JD005086>.
- Ellis, R., and S. Businger, 2010: Helical circulations in the typhoon boundary layer. *J. Geophys. Res.: Atmos.*, **115**, D06205, <https://doi.org/10.1029/2009JD011819>.
- Etling, D., and R. A. Brown, 1993: Roll vortices in the planetary boundary layer: A review. *Bound.-Layer Meteor.*, **65**, 215–248, <https://doi.org/10.1007/BF00705527>.
- Fabry, F., and W. Szyrmer, 1999: Modeling of the melting layer. Part II: Electromagnetic. *J. Atmos. Sci.*, **56**, 3593–3600, [https://doi.org/10.1175/1520-0469\(1999\)056<3593:MOTMLP>2.0.CO;2](https://doi.org/10.1175/1520-0469(1999)056<3593:MOTMLP>2.0.CO;2).
- Ferrier, B. S. 1994: A double-moment multiple-phase four-class bulk ice scheme. Part I: Description. *J. Atmos. Sci.*, **51**, 249–280. [https://doi.org/10.1175/1520-0469\(1994\)051<0249:admmpf>2.0.co;2](https://doi.org/10.1175/1520-0469(1994)051<0249:admmpf>2.0.co;2).
- Ferrier, B. S., W.-K. Tao, and J. Simpson, 1995: A double-moment multiple-phase four-class bulk ice scheme. Part II: Simulations of convective storms in different large-scale environments and comparisons with other bulk parameterizations. *J. Atmos. Sci.*, **52**, 1001–1033, [https://doi.org/10.1175/1520-0469\(1995\)052<1001:ADMMPF>2.0.CO;2](https://doi.org/10.1175/1520-0469(1995)052<1001:ADMMPF>2.0.CO;2).
- Field, P. R., A. J. Heymsfield, and A. Bansemer, 2007: Snow Size Distribution Parameterization for Mid-latitude and Tropical Ice Clouds. *J. Atmos. Sci.*, **64**, 4346–4365, <https://doi.org/10.1175/2007JAS2344.1>.
- Field, P.R., R. Brožková, M. Chen, J. Dudhia, C. Lac, T. Hara, R. Honnert, J. Olson, P. Siebesma, S. de Roode, L. Tomassini, A. Hill, and R. McTaggart-Cowan, 2017: Exploring the convective grey zone with regional simulations of a cold air outbreak. *Quart. J. Roy. Meteor. Soc.*, **143**, 2537–2555, <https://doi.org/10.1002/qj.3105>.
- Fielding, M. D., and M. Janisková, 2020: Direct 4D-Var assimilation of space-borne cloud radar reflectivity and lidar backscatter. Part I: Observation operator and implementation. *Quart. J. Roy. Meteor. Soc.*, **146**, 3877–3899, <https://doi.org/10.1002/qj.3878>.
- Foster, R. C., 2005: Why Rolls are Prevalent in the Hurricane Boundary Layer. *J. Atmos. Sci.*, **62**, 2647–2661, <https://doi.org/10.1175/JAS3475.1>.
- Gall, R., J. Tuttle, and P. Hildebrand, 1998: Small-Scale Spiral Bands Observed in Hurricanes Andrew, Hugo, and Erin. *Mon. Wea. Rev.*, **126**, 1749–1766, [https://doi.org/10.1175/1520-0493\(1998\)126<1749:SSSBOI>2.0.CO;2](https://doi.org/10.1175/1520-0493(1998)126<1749:SSSBOI>2.0.CO;2).

- Gao, K., and I. Ginis, 2014: On the Generation of Roll Vortices due to the Inflection Point Instability of the Hurricane Boundary Layer Flow. *J. Atmos. Sci.*, **71**, 4292–4307, <https://doi.org/10.1175/JAS-D-13-0362.1>.
- Gao, K., and I. Ginis, 2016: On the Equilibrium-State Roll Vortices and Their Effects in the Hurricane Boundary Layer. *J. Atmos. Sci.*, **73**, 1205–1222, <https://doi.org/10.1175/JAS-D-15-0089.1>.
- Geer, A. J., and P. Bauer, 2011: Observation errors in all-sky data assimilation. *Quart. J. Roy. Meteor. Soc.*, **137**, 2024–2037, <https://doi.org/10.1002/qj.830>.
- Geer, A. J., and Coauthors, 2018: All-sky satellite data assimilation at operational weather forecasting centres. *Quart. J. Roy. Meteor. Soc.*, **144**, 1191–1217, <https://doi.org/10.1002/qj.3202>.
- Hara, T., 2007: Implementation of improved Mellor-Yamada Level 3 scheme and partial condensation scheme to JMANHM and their performance. *CAS/JSC WGN Res. Activ. Atmos. Oceanic Modell.*, **37**, 0407–0408.
- Harrington, J. Y., K. Sulia, and H. Morrison, 2013: A method for adaptive habit prediction in bulk micro-physical models. Part I: Theoretical development. *J. Atmos. Sci.*, **70**, 349–364, <https://doi.org/10.1175/JAS-D-12-040.1>.
- Hashino, T., M. Satoh, Y. Hagihara, T. Kubota, T. Matsui, T. Nasuno, and H. Okamoto, 2013: Evaluating cloud microphysics from NICAM against CloudSat and CALIPSO. *J. Geophys. Res. Atmos.*, **118**, 7273–7292, <https://doi.org/10.1002/jgrd.50564>.
- Hashino, T., M. Satoh, Y. Hagihara, S. Kato, T. Kubota, T. Matsui, T. Nasuno, H. Okamoto, and M. Sekiguchi, 2016: Evaluating Arctic cloud radiative effects simulated by NICAM with A-train. *J. Geophys. Res.*, **121**, 7041–7063, <https://doi.org/10.1002/2016JD024775>.
- Hashino, T., and G. J. Tripoli, 2007: The spectral ice habit prediction system (SHIPS). Part I: Model description and simulation of the vapor deposition process. *J. Atmos. Sci.*, **64**, 2210–2237, <https://doi.org/10.1175/jas3963.1>.
- Hashino, T., and G. J. Tripoli, 2011: The Spectral Ice Habit Prediction System (SHIPS). Part III: Description of the Ice Particle Model and the Habit-Dependent Aggregation Model. *J. Atmos. Sci.*, **68**, 1125–1141, <https://doi.org/10.1175/2011JAS3666.1>.
- Helmus, J.J., and S.M. Collis, 2016: The Python ARM Radar Toolkit (Py-ART), a Library for Working with Weather Radar Data in the Python Programming Language. *Journal of Open Research Software*, **4**, <http://doi.org/10.5334/jors.119>.

- Honnert, R., G. A. Efstathiou, R. J. Beare, J. Ito, A. Lock, R. Neggers, R. S. Plant, H. Hailey Shin, L. Tomassini, and B. Zhou, 2020: The atmospheric boundary layer and the “gray zone” of turbulence: A critical review. *J. Geophys. Res.: Atmos.*, **125**, e2019JD030317, <https://doi.org/10.1029/2019JD030317>.
- Hou, A. Y., and Coauthors, 2014: The Global Precipitation Measurement Mission. *Bull. Amer. Meteor. Soc.*, **95**, 701–722, <https://doi.org/10.1175/BAMS-D-13-00164.1>.
- Iguchi, T., 2020: Dual-Frequency Precipitation Radar (DPR) on the Global Precipitation Measurement (GPM) Mission’s Core Observatory. *Satellite Precipitation Measurement*, Springer International Publishing, V. Levizzani et al., Eds., 183–192, https://doi.org/10.1007/978-3-030-24568-9_11.
- Iguchi, T., and Coauthors, 2018: GPM/DPR Level-2 Algorithm Theoretical Basis Document (V06). 127 pp., https://www.eorc.jaxa.jp/GPM/doc/algorithm/ATBD_DPR_201811_with_Appendix3b.pdf.
- Ikawa, M. and K. Saito, 1991: Description of a nonhydrostatic model developed at the Forecast Research Department of the MRI. *Technical Report of the MRI*, **28**, 238pp.
- Ikuta, Y., and Coauthors, 2020: A new data assimilation system and upgrading of physical processes in JMA’s meso-scale NWP system. *WGNE Res. Act. Earth System Model.*, **50**, 1.07–1.08, http://blue-book.meteoinfo.ru/uploads/2020/docs/01_Ikuta_Yasutaka_MAMSM2003.pdf.
- Ikuta, Y., K. Okamoto, and T. Kubota, 2021: One-dimensional maximum-likelihood estimation for spaceborne precipitation radar data assimilation. *Quart. J. Roy. Meteor. Soc.*, **147**, 858–875, <https://doi.org/10.1002/qj.3950>.
- Ikuta, Y., M. Satoh, M. Sawada, H. Kusabiraki, and T. Kubota, 2021a: Improvement of the Cloud Microphysics Scheme of the Mesoscale Model at the Japan Meteorological Agency Using Spaceborne Radar and Microwave Imager of the Global Precipitation Measurement as Reference. *Mon. Wea. Rev.*, **149**, 3803–3819, <https://doi.org/10.1175/MWR-D-21-0066.1>.
- Ikuta, Y., T. Fujita, Y. Ota, and Y. Honda, 2021b: Variational Data Assimilation System for Operational Regional Models at Japan Meteorological Agency. *J. Meteor. Soc. Japan*, **99**, 1563–1592, <https://doi.org/10.2151/jmsj.2021-076>.
- Illingworth, A. J., and Coauthors, 2015: The EarthCARE satellite: The next step forward in global measurements of clouds, aerosols, precipitation, and radiation. *Bull. Amer. Meteor. Soc.*, **96**, 1311–1332, <https://doi.org/10.1175/BAMS-D-12-00227.1>.

- Ishida, J., K. Aranami, K. Kawano, K. Matsubayashi, Y. Kitamura, C. Muroi, 2022: ASUCA: the JMA operational non-hydrostatic model. *J. Meteor. Soc. Japan*, **100**, 825–846, <https://doi.org/10.2151/jmsj.2022-043>.
- Ito, J., T. Oizumi, and H. Niino, 2017: Near-surface coherent structures explored by large eddy simulation of entire tropical cyclones. *Sci. Rep.*, **7**, 3798, <https://doi.org/10.1038/s41598-017-03848-w>.
- Jakob, C., 2003: An Improved Strategy for the Evaluation of Cloud Parameterizations in GCMS. *Bull. Amer. Meteor. Soc.*, **84**, 1387–1402, <https://doi.org/10.1175/BAMS-84-10-1387>.
- Japan Meteorological Agency, 2019: Outline of the operational numerical weather prediction at the Japan Meteorological Agency. Appendix to WMO Technical Progress Report on the Global Data-Processing and Forecasting System and Numerical Weather Prediction, 229 pp., <https://www.jma.go.jp/jma/jma-eng/jma-center/nwp/outline2019-nwp/index.htm>.
- Japan Meteorological Agency, 2020: Suuchi Yohou Kenshu Text 2020 (in Japanese). Japan Meteorological Agency Forecast Department, 153 pp., <https://www.jma.go.jp/jma/kishou/books/nwptext/nwptext.html>.
- Jensen, A. A., and J. Y. Harrington, 2015: Modeling Ice Crystal Aspect Ratio Evolution during Riming: A Single-Particle Growth Model. *J. Atmos. Sci.*, **72**, 2569–2590, <https://doi.org/10.1175/JAS-D-14-0297.1>.
- Jensen, A. A., J. Y. Harrington, H. Morrison, and J. A. Milbrandt, 2017: Predicting Ice Shape Evolution in a Bulk Microphysics Model. *J. Atmos. Sci.*, **74**, 2081–2104, <https://doi.org/10.1175/JAS-D-16-0350.1>.
- Jung, Y., G. Zhang, and M. Xue, 2008: Assimilation of Simulated Polarimetric Radar Data for a Convective Storm Using the Ensemble Kalman Filter. Part I: Observation Operators for Reflectivity and Polarimetric Variables. *Mon. Wea. Rev.*, **136**, 2228–2245, <https://doi.org/10.1175/2007MWR2083.1>.
- Jung, Y., M. Xue, and G. Zhang, 2010: Simulations of Polarimetric Radar Signatures of a Supercell Storm Using a Two-Moment Bulk Microphysics Scheme. *J. Appl. Meteor. Climatol.*, **49**, 146–163, <https://doi.org/10.1175/2009JAMC2178.1>.
- Kain, J. S., 2004: The Kain–Fritsch Convective Parameterization: An Update. *J. Appl. Meteor. Climatol.*, **43**, 170–181, [https://doi.org/10.1175/1520-0450\(2004\)043<0170:TKCPAU>2.0.CO;2](https://doi.org/10.1175/1520-0450(2004)043<0170:TKCPAU>2.0.CO;2).
- Keptert, J., 2001: The Dynamics of Boundary Layer Jets within the Tropical Cyclone Core. Part I: Linear Theory. *J. Atmos. Sci.*, **58**, 2469–2484, [https://doi.org/10.1175/1520-0469\(2001\)058<2469:TDO-BLJ>2.0.CO;2](https://doi.org/10.1175/1520-0469(2001)058<2469:TDO-BLJ>2.0.CO;2).

- Kepert, J., and Y. Wang, 2001: The Dynamics of Boundary Layer Jets within the Tropical Cyclone Core. Part II: Nonlinear Enhancement. *J. Atmos. Sci.*, **58**, 2485–2501, [https://doi.org/10.1175/1520-0469\(2001\)058<2485:TDOBLJ>2.0.CO;2](https://doi.org/10.1175/1520-0469(2001)058<2485:TDOBLJ>2.0.CO;2).
- Kepert, J. D., 2010a: Slab- and height-resolving models of the tropical cyclone boundary layer. Part I: Comparing the simulations. *Quart. J. Roy. Meteor. Soc.*, **136**, 1686–1699. <https://doi.org/10.1002/qj.667>.
- Kepert, J. D., 2010b: Slab- and height-resolving models of the tropical cyclone boundary layer. Part II: Why the simulations differ. *Quart. J. Roy. Meteor. Soc.*, **136**, 1700–1711. <https://doi.org/10.1002/qj.685>.
- Kessler, E., III, 1969: *On the Distribution and Continuity of Water Substance in Atmospheric Circulations*. *Meteor. Monogr.*, No. 32, Amer. Meteor. Soc., 84 pp.
- Kitamura, Y., 2016: Improving a Turbulence Scheme for the Terra Incognita in a Dry Convective Boundary Layer. *J. Meteor. Soc. Japan*, **94**, 491–506, <https://doi.org/10.2151/jmsj.2016-028>.
- Kiktev D., P. Joe, G.A. Isaac, A. Montani, I.-L. Frogner, P. Nurmi, B. Bica, J. Milbrandt, M. Tsyrlunikov, E. Astakhova, A. Bundel, S. Bélair, M. Pyle, A. Muravyev, G. Rivin, I. Rozinkina, T. Paccagnella, Y. Wang, J. Reid, T. Nipen, and K.-D. Ahn, 2017: FROST-2014: The Sochi Winter Olympics International Project. *Bull. Amer. Meteor. Soc.*, **98**, 1908–1929, <https://doi.org/10.1175/BAMS-D-15-00307.1>.
- Kojima, M., and Coauthors, 2012: Dual-frequency precipitation radar (DPR) development on the global precipitation measurement (GPM) core observatory. *Proc. SPIE*, 8528, 85281A, <https://doi.org/10.1117/12.976823>.
- Kosiba, K., J. Wurman, F. J. Masters, and P. Robinson, 2013: Mapping of Near-Surface Winds in Hurricane Rita Using Finescale Radar, Anemometer, and Land-Use Data. *Mon. Wea. Rev.*, **141**, 4337–4349, <https://doi.org/10.1175/MWR-D-12-00350.1>.
- Kosiba, K., and J. Wurman, 2014: Finescale Dual-Doppler Analysis of Hurricane Boundary Layer Structures in Hurricane Frances (2004) at Landfall. *Mon. Wea. Rev.*, **142**, 1874–1891, <https://doi.org/10.1175/MWR-D-13-00178.1>.
- Kotsuki, S., K. Terasaki, and T. Miyoshi, 2014: GPM/DPR precipitation compared with a 3.5-km-resolution NICAM simulation. *SOLA*, **10**, 204–209, <https://doi.org/10.2151/sola.2014-043>.

- Kozu, T., and Coauthors, 2001: Development of precipitation radar onboard the Tropical Rainfall Measuring Mission (TRMM) satellite. *IEEE Trans. Geosci. Remote Sens.*, **39**, 102–116, <https://doi.org/10.1109/36.898669>.
- Kuba, N., T. Seiki, K. Suzuki, W. Roh, and M. Satoh, 2020: Evaluation of rain microphysics using a radar simulator and numerical models: Comparison of two-moment bulk and spectral bin cloud microphysics schemes. *J. Adv. Model. Earth Syst.*, **12**, e2019MS001891, <https://doi.org/10.1029/2019MS001891>.
- Kubota, T., T. Iguchi, M. Kojima, L. Liao, T. Masaki, H. Hanado, R. Meneghini, and R. Oki, 2016: A statistical method for reducing sidelobe clutter for the Ku-band precipitation radar on board the GPM core observatory. *J. Atmos. Oceanic Technol.*, **33**, 1413–1428, <https://doi.org/10.1175/JTECH-D-15-0202.1>.
- Kummerow, C., W. Barnes, T. Kozu, J. Shiue, and J. Simpson, 1998: The Tropical Rainfall Measuring Mission (TRMM) sensor package. *J. Atmos. Oceanic Technol.*, **15**, 809–817, [https://doi.org/10.1175/1520-0426\(1998\)015<0809:TTRMMT>2.0.CO;2](https://doi.org/10.1175/1520-0426(1998)015<0809:TTRMMT>2.0.CO;2).
- Leroyer, S., S. Bélair, J. Mailhot, and I.B. Strachan, 2011: Microscale numerical prediction over Montreal with the Canadian external urban modeling system. *J. Appl. Meteor. Climatol.*, **50**, 2410–2428, <https://doi.org/10.1175/JAMC-D-11-013.1>.
- Le, M., and V. Chandrasekar, 2013: Hydrometeor profile characterization method for dual-frequency precipitation radar onboard the GPM. *IEEE Trans. Geosci. Remote Sens.*, **51**, 3648–3658, <https://doi.org/10.1109/TGRS.2012.2224352>.
- Lean, H. W., P. A. Clark, M. Dixon, N. M. Roberts, A. Fitch, R. Forbes, and C. Halliwell, 2008: Characteristics of high-resolution versions of the Met Office Unified Model for forecasting convection over the United Kingdom. *Mon. Wea. Rev.*, **136**, 3408–3424.
- Li, X., W.-K. Tao, T. Matsui, C. Liu, and H. Masunaga, 2010: Improving a spectral bin microphysical scheme using TRMM satellite observations. *Quart. J. Roy. Meteor. Soc.*, **136**, 382–399, <https://doi.org/10.1002/qj.569>.
- Li, X., Z. Pu, and Z. Gao, 2021: Effects of Roll Vortices on the Evolution of Hurricane Harvey during Landfall. *J. Atmos. Sci.*, **78**, 1847–1867, <https://doi.org/10.1175/JAS-D-20-0270.1>.
- Lin, Y.-L., R. D. Farley, and H. D. Orville, 1983: Bulk parameterization of the snow field in a cloud model. *J. Climate Appl. Meteor.*, **22**, 1065–1092, [https://doi.org/10.1175/1520-0450\(1983\)022<1065:BPOTSF>2.0.CO;2](https://doi.org/10.1175/1520-0450(1983)022<1065:BPOTSF>2.0.CO;2).

- Liu, G., 2008: A database of microwave single-scattering properties for nonspherical ice particles. *Bull. Amer. Meteor. Soc.*, **89**, 1563–1570, <https://doi.org/10.1175/2008BAMS2486.1>.
- Lorsolo, S., J. L. Schroeder, P. Dodge, and F. Marks, 2008: An observational study of hurricane boundary layer small-scale coherent structures. *Mon. Wea. Rev.*, **136**, 2871–2893, <https://doi.org/10.1175/2008MWR2273.1>.
- Magono, C., and C. W. Lee, 1966. Meteorological classification of natural snow crystals. *J. Fac. Sci., Hokkaido Univ.*, Ser. VII 4, 321–335 (with Plates 27).
- Mashiko, W., 2020: Characteristics of typhoons that brought storms, tornadoes and other gusty winds to Japan in 2019. Proceedings of Japan meteorological society meeting, (in Japanese).
- Masunaga, H., M. Satoh, and H. Miura, 2008: A joint satellite and global cloud-resolving model analysis of a Madden-Julian Oscillation event: Model diagnosis. *J. Geophys. Res.*, **113**, D17210, <https://doi.org/10.1029/2008JD009986>.
- Masson V., 2020: WMO Research Demonstration Project “Paris Olympic Games 2024“, AMS Annual meeting 2020. <https://ams.confex.com/ams/2020Annual/webprogram/Paper366490.html>
- Matsui, T., X. Zeng, W.-K. Tao, H. Masunaga, W. S. Olson, and S. Lang, 2009: Evaluation of Long-Term Cloud-Resolving Model Simulations Using Satellite Radiance Observations and Multifrequency Satellite Simulators. *J. Atmos. Oceanic Technol.*, **26**, 1261–1274, <https://doi.org/10.1175/2008JTECHA1168.1>.
- Matsui, T., J.-D. Chern, W.-K. Tao, S. Lang, M. Satoh, T. Hashino, and T. Kubota, 2016: On the land–ocean contrast of tropical convection and microphysics statistics derived from TRMM satellite signals and global storm-resolving models. *J. Hydrometeor.*, **17**, 1425–1445, <https://doi.org/10.1175/JHM-D-15-0111.1>.
- Matsui, T., B. Dolan, S. A. Rutledge, W.-K. Tao, T. Iguchi, J. Barnum, and S. E. Lang, 2019: POLAR-RIS: A POLArimetric Radar Retrieval and Instrument Simulator. *J. Geophys. Res.: Atmos.*, **124**, 4634–4657, <https://doi.org/10.1029/2018JD028317>.
- Matsui, T., B. Dolan, T. Iguchi, S. A. Rutledge, W.-K. Tao, and S. Lang, 2020: Polarimetric Radar Characteristics of Simulated and Observed Intense Convective Cores for a Midlatitude Continental and Tropical Maritime Environment. *J. Hydrometeor.*, **21**, 501–517, <https://doi.org/10.1175/JHM-D-19-0185.1>.
- McTaggart-Cowan, R., P. A. Vaillancourt, A. Zadra, S. Chamberland, M. Charron, S. Corvec, J. A. Milbrandt, D. Paquin-Ricard, A. Patoine, M. Roch, L. Separovic, and J. Yang, 2019: Modernization of

- atmospheric physics parameterization in Canadian NWP. *Journal of Advances in Modeling Earth Systems*, **11**, 3593–3635. <https://doi.org/10.1029/2019MS001781>.
- Mellor, G. L., and T. Yamada, 1974: A Hierarchy of Turbulence Closure Models for Planetary Boundary Layers. *J. Atmos. Sci.*, **31**, 1791–1806, [https://doi.org/10.1175/1520-0469\(1974\)031<1791:AHOTCM>2.0.CO;2](https://doi.org/10.1175/1520-0469(1974)031<1791:AHOTCM>2.0.CO;2).
- Mellor, G. L., and T. Yamada, 1982: Development of a turbulence closure model for geophysical fluid problems. *Rev. Geophys.*, **20**, 851–875, <https://doi.org/10.1029/RG020i004p00851>.
- Milbrandt, J. A., and M. K. Yau, 2005a: A multimoment bulk microphysics parameterization. Part I: Analysis of the role of the spectral shape parameter. *J. Atmos. Sci.*, **62**, 3051–3064, <https://doi.org/10.1175/jas3534.1>.
- Milbrandt, J. A., and M. K. Yau, 2005b: A multimoment bulk microphysics parameterization. Part II: A proposed three-moment closure and scheme description. *J. Atmos. Sci.*, **62**, 3065–3081, <https://doi.org/10.1175/jas3535.1>.
- Mishchenko, M. I., L. D. Travis, and D. W. Mackowski, 1996: T-matrix computations of light scattering by nonspherical particles: A review. *Journal of Quantitative Spectroscopy and Radiative Transfer*, **5**, 535–575, ISSN 0022-4073, [https://doi.org/10.1016/0022-4073\(96\)00002-7](https://doi.org/10.1016/0022-4073(96)00002-7).
- Mitchell, D. L., 1996: Use of mass- and area-dimensional power laws for determining precipitation particle terminal velocities. *J. Atmos. Sci.*, **53**, 1710–1723, [https://doi.org/10.1175/1520-0469\(1996\)053<1710:UOMAAD>2.0.CO;2](https://doi.org/10.1175/1520-0469(1996)053<1710:UOMAAD>2.0.CO;2).
- Mitchell, D. L., R. P. d’Entremont, and R. P. Lawson, 2010: Inferring Cirrus Size Distributions through Satellite Remote Sensing and Microphysical Databases, *J. Atmos. Sci.*, **67**, 1106–1125, <https://doi.org/10.1175/2009JAS3150.1>
- Miyamoto, Y., H. Fudeyasu and A. Wada, 2022: Intensity and Structural Changes of Numerically Simulated Typhoon Faxai (1915) before Landfall. *J. Meteor. Soc. Japan*, **100**, <https://doi.org/10.2151/jmsj.2022-009>.
- Morrison, I., S. Businger, F. Marks, P. Dodge, and J. A. Businger, 2005: An Observational Case for the Prevalence of Roll Vortices in the Hurricane Boundary Layer. *J. Atmos. Sci.*, **62**, 2662–2673, <https://doi.org/10.1175/JAS3508.1>.
- Morrison, H., and J. A. Milbrandt, 2015: Parameterization of cloud microphysics based on the prediction of bulk ice particle properties. Part I: Scheme description and idealized tests. *J. Atmos. Sci.*, **72**, 287–311, <https://doi.org/10.1175/jas-d-14-0065.1>.

- Murakami, M., 1990: Numerical modeling of dynamical and microphysical evolution of an isolated convective cloud. *J. Meteor. Soc. Japan*, **68**, 107–128, https://doi.org/10.2151/jmsj1965.68.2_107.
- Nagata, K., 2011: Quantitative precipitation estimation and quantitative precipitation forecasting by the Japan Meteorological Agency. *Technical Review of RSMC Tokyo*, **13**, 37–50. [Available at <http://www.jma.go.jp/jma/jma-eng/jma-center/rsmc-hp-pub-eg/techrev/text13-2.pdf>.]
- Neggers, R. A. J., and A. P. Siebesma, 2013: Constraining a System of Interacting Parameterizations through Multiple-Parameter Evaluation: Tracing a Compensating Error between Cloud Vertical Structure and Cloud Overlap. *J. Climate*, **26**, 6698–6715, <https://doi.org/10.1175/JCLI-D-12-00779.1>.
- Nakanishi, M., and H. Niino, 2004: An Improved Mellor–Yamada Level-3 Model with Condensation Physics: Its Design and Verification. *Bound.-Layer Meteor.*, **112**, 1–31, <https://doi.org/10.1023/B:BOUN.0000020164.04146.98>.
- Nakanishi, M. and H. Niino, 2006: An Improved Mellor–Yamada Level 3 Model: Its Numerical Stability and Application to a Regional Prediction of Advection Fog. *Bound.-Layer Meteor.*, **119**, 397–407, <http://dx.doi.org/10.1007/s10546-005-9030-8>.
- Nakanishi, M., and H. Niino, 2009: Development of an Improved Turbulence Closure Model for the Atmospheric Boundary Layer. *J. Meteor. Soc. Japan*, **87**, 895–912, <https://doi.org/10.2151/jmsj.87.895>.
- Nakanishi, M., and H. Niino, 2012: Large-Eddy Simulation of Roll Vortices in a Hurricane Boundary Layer. *J. Atmos. Sci.*, **69**, 3558–3575, <https://doi.org/10.1175/JAS-D-11-0237.1>.
- Nishizawa, S., H. Yashiro, Y. Sato, Y. Miyamoto, and H. Tomita, 2015, Influence of grid aspect ratio on planetary boundary layer turbulence in large-eddy simulations. *Geosci. Model Dev.*, **8**, 3393–3419, <https://doi.org/10.5194/gmd-8-3393-2015>.
- Nolan, D. S., 2005: Instabilities in hurricane-like boundary layers. *Dyn. Atmos. Oceans*, **40**, 209–236, <https://doi.org/10.1016/j.dynatmoce.2005.03.002>.
- Nolan, D. S., J. A. Zhang, and D. P. Stern, 2009a: Evaluation of Planetary Boundary Layer Parameterizations in Tropical Cyclones by Comparison of In Situ Observations and High-Resolution Simulations of Hurricane Isabel (2003). Part I: Initialization, Maximum Winds, and the Outer-Core Boundary Layer. *Mon. Wea. Rev.*, **137**, 3651–3674, <https://doi.org/10.1175/2009MWR2785.1>.
- Nolan, D. S., D. P. Stern, and J. A. Zhang, 2009b: Evaluation of Planetary Boundary Layer Parameterizations in Tropical Cyclones by Comparison of In Situ Observations and High-Resolution Simulations

- of Hurricane Isabel (2003). Part II: Inner-Core Boundary Layer and Eyewall Structure. *Mon. Wea. Rev.*, **137**, 3675–3698, <https://doi.org/10.1175/2009MWR2786.1>.
- Ogura, Y., and N. A. Phillips, 1962: Scale Analysis of Deep and Shallow Convection in the Atmosphere. *J. Atmos. Sci.*, **19**, 173–179, [https://doi.org/10.1175/1520-0469\(1962\)019<0173:SAODAS>2.0.CO;2](https://doi.org/10.1175/1520-0469(1962)019<0173:SAODAS>2.0.CO;2).
- Ogura, Y., and M. Yoshizaki, 1988: Numerical Study of Orographic-Convective Precipitation over the Eastern Arabian Sea and the Ghat Mountains during the Summer Monsoon. *J. Atmos. Sci.*, **45**, 2097–2122, [https://doi.org/10.1175/1520-0469\(1988\)045<2097:NSOOC>2.0.CO;2](https://doi.org/10.1175/1520-0469(1988)045<2097:NSOOC>2.0.CO;2).
- Okamoto, K., K. Aonashi, T. Kubota, and T. Tashima, 2016: Experimental assimilation of the GPM core observatory DPR reflectivity profiles for Typhoon Halong (2014). *Mon. Wea. Rev.*, **144**, 2307–2326, <https://doi.org/10.1175/MWR-D-15-0399.1>.
- Pielke, R.A., W.R. Cotton, R.L. Walko, C.J. Tremback, W.A. Lyons, L.D. Grasso, M.E. Nicholls, M.D. Moran, D.A. Wesley, T.J. Lee, and J.H. Copeland, 1992: A comprehensive meteorological modeling system—RAMS. *Meteorol. Atmos. Phys.*, **49**, 69–91, <https://doi.org/10.1007/BF01025401>.
- Putnam, B. J., M. Xue, Y. Jung, G. Zhang, and F. Kong, 2017: Simulation of Polarimetric Radar Variables from 2013 CAPS Spring Experiment Storm-Scale Ensemble Forecasts and Evaluation of Microphysics Schemes. *Mon. Wea. Rev.*, **145**, 49–73, <https://doi.org/10.1175/MWR-D-15-0415.1>.
- Richardson, L. F., 1922: *Weather Prediction by Numerical Process*. Cambridge University Press, Cambridge.
- Ryzhkov, A., M. Pinsky, A. Pokrovsky, and A. Khain, 2011: Polarimetric Radar Observation Operator for a Cloud Model with Spectral Microphysics. *J. Appl. Meteor. Climatol.*, **50**, 873–894, <https://doi.org/10.1175/2010JAMC2363.1>.
- Roh, W., and M. Satoh, 2014: Evaluation of Precipitating Hydrometeor Parameterizations in a Single-Moment Bulk Microphysics Scheme for Deep Convective Systems over the Tropical Central Pacific. *J. Atmos. Sci.*, **71**, 2654–2673, <https://doi.org/10.1175/JAS-D-13-0252.1>.
- Roh, W., and M. Satoh, 2021: An introduction to the ULTIMATE project in Japan. 23rd EGU General Assembly, EGU, EGU21-11901, <https://doi.org/10.5194/egusphere-egu21-11901>.
- Roh, W., M. Satoh, and T. Nasuno, 2017: Improvement of a cloud microphysics scheme for a global non-hydrostatic model using TRMM and a satellite simulator. *J. Atmos. Sci.*, **74**, 167–184, <https://doi.org/10.1175/JAS-D-16-0027.1>.

- Roh, W., M. Satoh, T. Hashino, H. Okamoto, and T. Seiki, 2020: Evaluations of the thermodynamic phases of clouds in a cloud-system-resolving model using CALIPSO and a satellite simulator over the Southern Ocean. *J. Atmos. Sci.*, **77**, 3781–3801, <https://doi.org/10.1175/JAS-D-19-0273.1>.
- Rutledge, S. A., and P. V. Hobbs, 1984: The mesoscale and microscale structure and organization of clouds and precipitation in midlatitude cyclones. XII: A diagnostic modeling study of precipitation development in narrow cold-frontal rainbands. *J. Atmos. Sci.*, **41**, 2949–2972, [https://doi.org/10.1175/1520-0469\(1984\)041<2949:TMAMSA>2.0.CO;2](https://doi.org/10.1175/1520-0469(1984)041<2949:TMAMSA>2.0.CO;2).
- Saito, K., T. Fujita, Y. Yamada, J. Ishida, Y. Kumagai, K. Aranami, S. Ohmori, R. Nagasawa, S. Kumagai, C. Muroi, T. Kato, H. Eito, and Y. Yamazaki, 2006: The operational JMA Nonhydrostatic Mesoscale Model. *Mon. Wea. Rev.*, **134**, 1266–1298, <https://doi.org/10.1175/MWR3120.1>.
- Satoh, M. 2008 : Numerical simulations of heavy rainfalls by a global cloud-resolving model. *J. Disaster Research*, **3**, 33–38, <https://doi.org/10.20965/jdr.2008.p0033>.
- Satoh, M., 2013: *Atmospheric Circulation Dynamics and General Circulation Models, 2nd edition*. Springer-PRAXIS, 757 pp, <http://dx.doi.org/10.1007/978-3-642-13574-3>.
- Satoh, M., 2021: ULTIMATE: Ultra-site for measuring atmosphere of Tokyo metropolitan environment (in Japanese). *J. Remote Sens. Soc. Japan*, **41**, 133–139, <https://doi.org/10.11440/rssj.41.133>.
- Satoh, M., S. Matsugishi, W. Roh, Y. Ikuta, N. Kuba, T. Seiki, T. Hashino, and H. Okamoto, 2022: Evaluation of cloud and precipitation processes in regional and global models with ULTIMATE (ULtra-sItE for Measuring Atmosphere of Tokyo metropolitan Environment): A case study using the dual-polarization Doppler weather radars. *Prog. Earth Planet. Sci.*, **9**, 51, <https://doi.org/10.1186/s40645-022-00511-5>.
- Saunders, R., and Coauthors, 2018: An update on the RTTOV fast radiative transfer model (currently at version 12). *Geosci. Model Dev.*, **11**, 2717–2737, <https://doi.org/10.5194/gmd-11-2717-2018>.
- Schubert, W. H., and J. J. Hack, 1983: Transformed Eliassen balanced vortex model. *J. Atmos. Sci.*, **40**, 1571–1583, [https://doi.org/10.1175/1520-0469\(1983\)040%3C1571:TEBVM%3E2.0.CO;2](https://doi.org/10.1175/1520-0469(1983)040%3C1571:TEBVM%3E2.0.CO;2).
- Seity, Y., P. Brousseau, S. Malardel, G. Hello, P. Bénard, F. Bouttier, C. Lac, and V. Masson, 2011: The AROME-France convective scale operational model. *Mon. Wea. Rev.*, **139**, 976–991, <https://doi.org/10.1175/2010MWR3425.1>.
- Seto, S., T. Iguchi, R. Meneghini, J. Awaka, T. Kubota, T. Masaki, and N. Takahashi, 2021: The precipitation rate retrieval algorithms for the GPM dual-frequency precipitation radar. *J. Meteor. Soc. Japan*, **99**, 205–237, <https://doi.org/10.2151/jmsj.2021-011>. Shimpo, A., and Coauthors, 2019: Primary

- factors behind the heavy rain event of July 2018 and the subsequent heat wave in Japan. *SOLA*, **15**, 13–18, <https://doi.org/10.2151/sola.15A-003>.
- Shrestha, P., S. Trömel, R. Evaristo, and C. Simmer, 2022: Evaluation of modelled summertime convective storms using polarimetric radar observations. *Atmos. Chem. Phys.*, **22**, 7593–7324, <https://doi.org/10.5194/acp-22-7593-2022>.
- Shipway, B. J., and A. A. Hill, 2012: Diagnosis of systematic differences between multiple parametrizations of warm rain microphysics using a kinematic framework. *Quart. J. Roy. Meteor. Soc.*, **138**, 2196–2211, <https://doi.org/10.1002/qj.1913>.
- Skamarock, W. C. 2004: Evaluating Mesoscale NWP Models Using Kinetic Energy Spectra. *Mon. Wea. Rev.*, **132**, 3019–3032, <https://doi.org/10.1175/MWR2830.1>.
- Skamarock, W. C., and Coauthors, 2008: A description of the Advanced Research WRF version 3. NCAR Tech. Note NCAR/TN-4751STR, 113 pp. [Available online at http://www.mmm.ucar.edu/wrf/users/docs/arw_v3_bw.pdf.]
- Skofronick-Jackson, G., and Coauthors, 2017: The Global Precipitation Measurement (GPM) mission for science and society. *Bull. Amer. Meteor. Soc.*, **98**, 1679–1695, <https://doi.org/10.1175/BAMS-D-15-00306.1>.
- Smagorinsky, J., 1963: GENERAL CIRCULATION EXPERIMENTS WITH THE PRIMITIVE EQUATIONS. *Mon. Wea. Rev.*, **91**, 99–164, [https://doi.org/10.1175/1520-0493\(1963\)091<0099:GCEWTP>2.3.CO;2](https://doi.org/10.1175/1520-0493(1963)091<0099:GCEWTP>2.3.CO;2).
- Smith, R. N. B., 1990: A scheme for predicting layer clouds and their water content in a general circulation model. *Quart. J. Roy. Meteor. Soc.*, **116**, 435–460, <https://doi.org/10.1002/qj.49711649210>.
- Straka, J. M., and E. R. Mansell, 2005: A Bulk Microphysics Parameterization with Multiple Ice Precipitation Categories. *J. Appl. Meteor. Climatol.*, **44**, 445–466, <https://doi.org/10.1175/JAM2211.1>.
- Stull, R.B. 1988: An Introduction to Boundary Layer Meteorology. Kluwer Academic Publishers, Dordrecht, Boston and London, 666 p.
- Swales, D. J., R. Pincus, and A. Bodas-Salcedo, 2018: The cloud feedback model intercomparison project observational simulator package: Version 2. *Geosci. Model Dev.*, **11**, 77–81, <https://doi.org/10.5194/gmd-11-77-2018>.
- Tang, Y., H.W., Lean, and J., Bornemann, 2013: The benefits of the Met Office variable resolution NWP model for forecasting convection. *Met. Apps*, **20**: 417–426, <https://doi.org/10.1002/met.1300>.

- Tang, J., J.A. Zhang, P. Chan, K. Hon, X. Lei, and Y. Wang, 2021 : A direct aircraft observation of helical rolls in the tropical cyclone boundary layer. *Sci. Rep.*, **11**, 18771, <https://doi.org/10.1038/s41598-021-97766-7>.
- Thompson, G., P. R. Field, R. M. Rasmussen, and W. D. Hall, 2008: Explicit Forecasts of Winter Precipitation Using an Improved Bulk Microphysics Scheme. Part II: Implementation of a New Snow Parameterization. *Mon. Wea. Rev.*, **136**, 5095–5115, <https://doi.org/10.1175/2008MWR2387.1>.
- Tomassini L., R. Honnert, G. Efstathiou, A. Lock, and P. Siebesma, 2018: Second phase of the “Grey Zone” project based on the EUREC4A and phase III of GATE field campaigns. *WGNE/GASS White Paper on scale-awareness, stochasticity, and convective organization*, https://www.gewex.org/gewex-content/uploads/2018/09/GASSWhitePaper_GreyZoneII_1Sep2018.pdf.
- Tomita, H. and M. Satoh, 2004: A new dynamical framework of nonhydrostatic global model using the icosahedral grid. *Fluid Dyn. Res.*, **34**, 357–400, <https://doi.org/10.1016/j.fluiddyn.2004.03.003>.
- Tsuboki, K. and A. Sakakibara, 2001: CReSS User’s Guide 2nd Edition. http://www.rain.hyarc.nagoya-u.ac.jp/~tsuboki/kyoto_dpri_17g-c1/cress_html/guide_eng/frontpage.pdf
- Tsuboki, K. and A. Sakakibara, 2002: Large-scale parallel computing of Cloud Resolving Storm Simulator. High Performance Computing, Springer, H. P. Zima et al. Eds, 243–259.
- Vivekanandan, J., W. M. Adams, and V. N. Bringi, 1991: Rigorous Approach to Polarimetric Radar Modeling of Hydrometeor Orientation Distributions. *J. Appl. Meteor. Climatol.*, **30**, 1053–1063, [https://doi.org/10.1175/1520-0450\(1991\)030<1053:RATPRM>2.0.CO;2](https://doi.org/10.1175/1520-0450(1991)030<1053:RATPRM>2.0.CO;2).
- Watanabe, M., and Coauthors, 2010: Improved Climate Simulation by MIROC5: Mean States, Variability, and Climate Sensitivity. *J. Climate*, **23**, 6312–6335, <https://doi.org/10.1175/2010JCLI3679.1>.
- Wilson, D. R., and S. P. Ballard, 1999: A microphysically based precipitation scheme for the UK Meteorological Office Unified Model. *Quart. J. Roy. Meteor. Soc.*, **125**, 1607–1636, <https://doi.org/10.1002/qj.49712555707>.
- WMO, 2019: Manual on Codes. WMO-No.306, World Meteorological Organization.
- Wurman, J., and K. Kosiba, 2018: The Role of Small-Scale Vortices in Enhancing Surface Winds and Damage in Hurricane Harvey (2017). *Mon. Wea. Rev.*, **146**, 713–722, <https://doi.org/10.1175/MWR-D-17-0327.1>.

- Wurman, J., and J. Winslow, 1998: Intense Sub-Kilometer-Scale Boundary Layer Rolls Observed in Hurricane Fran. *Science*, **280**, 555–557, <https://doi.org/10.1126/science.280.5363.555>.
- Wyngaard, J. C., 2004: Toward Numerical Modeling in the “Terra Incognita”. *J. Atmos. Sci.*, **61**, 1816–1826, [https://doi.org/10.1175/1520-0469\(2004\)061<1816:TNMITT>2.0.CO;2](https://doi.org/10.1175/1520-0469(2004)061<1816:TNMITT>2.0.CO;2).
- Yuter, S. E., and R. A. Jr. Houze, 1995: Three-Dimensional Kinematic and Microphysical Evolution of Florida Cumulonimbus. Part II: Frequency Distributions of Vertical Velocity, Reflectivity, and Differential Reflectivity. *Mon. Wea. Rev.*, **123**, 1941–1963, [https://doi.org/10.1175/1520-0493\(1995\)123%3C1941:TDKAME%3E2.0.CO;2](https://doi.org/10.1175/1520-0493(1995)123%3C1941:TDKAME%3E2.0.CO;2).
- Zängl, G., D. Reinert, P. Rípodas, and M. Baldauf, 2015: The ICON (icosahedral non-hydrostatic) modeling framework of DWD and MPI-M: Description of the non-hydrostatic dynamical core. *Quart. J. Roy. Meteor. Soc.*, **141**, 563–579, <https://doi.org/10.1002/qj.2378>.
- Zhang, J. A., K. B. Katsaros, P. G. Black, S. Lehner, J. R. French, and W. M. Drennan, 2008: Effects of roll vortices on turbulent fluxes in the hurricane boundary layer. *Bound.-Layer Meteor.*, **128**, 173–189, <https://doi.org/10.1007/s10546-008-9281-2>.
- Zhang, J. A., R. F. Rogers, D. S. Nolan, and F. D. Marks Jr., 2011: On the Characteristic Height Scales of the Hurricane Boundary Layer. *Mon. Wea. Rev.*, **139**, 2523–2535, <https://doi.org/10.1175/MWR-D-10-05017.1>.
- Zhang, J. A., and W. M. Drennan, 2012: An observational study of vertical eddy diffusivity in the hurricane boundary layer. *J. Atmos. Sci.*, **69**, 3223–3236, <https://doi.org/10.1175/JAS-D-11-0348.1>.
- Zhou, Y. P., and Coauthors, 2007: Use of High-Resolution Satellite Observations to Evaluate Cloud and Precipitation Statistics from Cloud-Resolving Model Simulations. Part I: South China Sea Monsoon Experiment. *J. Atmos. Sci.*, **64**, 4309–4329, <https://doi.org/10.1175/2007JAS2281.1>.
- Ziegler, C. L. 1985: Retrieval of thermal and microphysical variables in observed convective storms. Part 1: Model development and preliminary testing. *J. Atmos. Sci.*, **42**, 1487–1509, [https://doi.org/10.1175/1520-0469\(1985\)042<1487:rotamv>2.0.co;2](https://doi.org/10.1175/1520-0469(1985)042<1487:rotamv>2.0.co;2).